A high-performance bosonic optical lattice clock

Inaugural dissertation

for the attainment of the title of doctor
in the Faculty of Mathematics and Natural Sciences
at the Heinrich-Heine-Universität Düsseldorf

presented by

Stefano Origlia
from Mondovì

Düsseldorf, February 2018

from the Institut für Experimentalphysik
at the Heinrich-Heine-Universität Düsseldorf

Published by permission of
the Faculty of Mathematics and Natural Sciences at
Heinrich-Heine-Universität Düsseldorf

Supervisor: Prof. Stephan Schiller
Co-supervisor: Prof. Michael Schmitt

Date of the oral examination: 15/10/2018

Abstract

Optical clocks are being developed worldwide and are at the forefront of frequency metrology. Today they outperform microwave clocks' instability and inaccuracy by two orders of magnitude, raising discussion about the redefinition of the SI second. Their outstanding performances are paving the way to applications in different fields apart from metrology. Optical clocks can be used for geodetic measurements, such as chronometric leveling, and fundamental physics experiments. These applications require transportable, and even space-born optical clocks that are in development. Space optical clocks will serve as a highly accurate references for intercontinental clock comparisons, and will also provide a unique test bench for fundamental physics theories, such as Einstein's prediction of time dilation and equivalence principle.

This work presents the development and characterization of a transportable strontium optical lattice clock, realized in the framework of the ESA I-SOC (Space Optical Clock on the ISS) mission. The aim of the project is to investigate new technologies and techniques, in order to develop a robust apparatus as demonstrator for space applications. Special effort has been made to reduce the size and weight of the clock, so as to meet the stringent requirements of a space mission. The system reported here is one of the most compact optical clocks to date, with a total volume of only $1\,\mathrm{m}^3$, excluding electronics.

The clock is operated with the strontium bosonic isotope ^{88}Sr: this is preferable to the fermionic counterpart ^{87}Sr, commonly used in optical lattice clocks, if simplicity and reliability are required. However, in terms of accuracy, bosonic clocks present some disadvantages compared with the fermionic ones, which have significantly slowed down their development for metrological applications.

We characterized the relevant operating parameters and their effect on the clock accuracy and instability. Exploiting a clock laser offering an outstanding stability, we were able to demonstrate a clock fractional instability of 3×10^{-18}, and an inaccuracy of 2×10^{-17}: both values represent a factor of 30 improvement compared with previous works on bosonic optical clocks. These results suggest that, in the near future, bosonic clocks may become competitive to their fermionic counterparts. This is of interest for applications such as time scale realization, transportable clocks, or for test of fundamental physics. As an example, we measured the ^{88}Sr$-^{87}$Sr isotope shift, with an uncertainty of 12 mHz.

Zusammenfassung

Optisch Uhren werden seit Jahrzehnten weltweit entwickelt und bilden die Spitze in der Frequenzmetrologie. Heutzutage übertreffen sie in Stabilität und Genauigkeit die etablierten Mikrowellenstandards um mehr als zwei Größenordnungen was eine Diskussion über die Neudefinition der Sekunde anregt. Die außerordentliche Leistungsfähigkeit optischer Uhren, ebnet den Weg zu unterschiedlichsten Anwendungsgebieten der Metrologie. Potentielle Anwendungsgebiete wären beispielsweise geodätische Messungen wie die chronometrische Nivellierung oder Tests fundamentaler Physik. Derartige Anwendungen erfordern transportable und sogar weltraumtaugliche optische Uhren, die sich derzeit in der Entwicklung befinden. Weltraumbasierte optische Uhren dienen bei interkontinentalen Vergleichen anderer optischer Uhren als ultrapräzise Referenz. Zugleich ermöglichen sie Tests fundamentaler Physik wie dem Einstein'schen Äquivalenzprinzip oder der Zeitdilatation.

In dieser Arbeit wird der aktuelle Status der Entwicklung und Charakterisierung einer transportablen optischen Gitteruhr basierend auf Strontium, welche im Ramen des ESA I-SOC Projektes (Space Optical Clock on the ISS) durchgeführt wird, präsentiert. Ziel des Projektes ist die Entwicklung und Erprobung neuer Technologien und Techniken um eine optische Uhr herzustellen, die als robuster Prototyp für Weltraumanwendungen dient. Hoher Wert wurde auf ein geringes Gewicht und möglichst geringe Baugröße gelegt, um die strikten Anforderungen eines Raumfluges zu erfüllen. Das in dieser Arbeit präsentierte System mit einem Volumen (ohne Elektronik) von nur 1 m^3, ist bis heute eine der kompaktesten optischen Gitteruhren weltweit.

Die Uhr wird mit dem bosonischen Strontium Isotop ^{88}Sr betrieben: dies ist im Gegensatz zu dem gewöhnlich in optischen Uhren benutzten fermionischen ^{87}Sr zu bevorzugen, falls Einfachheit und Zuverlässigkeit benötigt werden. In Bezug auf Genauigkeit haben bosonische Uhren jedoch im Vergleich zu den fermionischen einige Nachteile, welche ihre Entwicklung für metrologische Zwecke signifikant verlangsamt haben.

Die relevanten Betriebsparameter und deren Einfluss auf die Genauigkeit sowie der Instabilität der Uhr wurden charakterisiert. Die Verwendung eines extrem frequenzstabilen Uhrenlasers ermöglichte eine Instabilität von 3×10^{-18} und eine Ungenauigkeit von 2×10^{-17}: Beide Werte stellen eine Verbesserung um den Faktor 30 dar, verglichen mit den Ergebnissen anderer bosonischer optischer Uhren. Diese Werte legen nahe, dass die bosonischen Uhren in naher Zukunft mit ihren fermionischen Gegenstücken konkurrieren könnten. Im Hinblick auf die Realisierung einer Zeitskala, die weitere Entwicklung transportabler Uhren oder die Untersuchung fundamentaler Physik, ist dies sehr von Interesse. Beispielsweise waren wir im Ramen dieser Arbeit in der Lage, die Isotopieverschiebung von ^{88}Sr zu ^{87}Sr mit einer Unsicherheit von 12 mHz zu messen.

Contents

Contents

Chapter 1

Atomic clocks

In 1967 the International System of Units (SI) [1] has abandoned the definition of the second referenced to the Earth's revolution period around the Sun, and introduced a new definition based on a particular atomic transition: the second is defined as the duration of 9192631770 periods of the radiation corresponding to the transition between the two hyperfine states F = 3 and F = 4 (F is the total angular momentum of the state) of the ground state of cesium-133 (at a temperature of 0 °C). The first cesium clock was developed in 1955 [2], following the works by Rabi and Ramsey, and its accuracy was at 10^{-10} relative level. Nowadays the best cesium clocks (i.e. cesium fountains) show accuracies at the level of $\Gamma/\nu_0 = 1 \times 10^{-16}$ [3], where Γ and ν_0 are the transition linewidth and frequency, respectively.

Accuracy represents, together with instability, the most important parameter to define the performance of a frequency standard. In atomic clocks, the environment surrounding the atoms (electric and magnetic fields, light fields, BBR, etc.) perturbs the clock transition energy levels, resulting in a shift of the clock transition frequency: this shift needs to be characterized and an uncertainty budget table, including all the contributions to the transition shift, is produced. The final clock accuracy tells how well is known the clock frequency compared with the unperturbed atomic transition frequency (Figure 1.1). On the other hand, the clock instability is a statistical measurement of how the clock frequency varies in time. Also the instability may be affected by external perturbations, changing in time, which can be corrected and compensated with proper monitoring and stabilization techniques.

1.1 Atomic frequency standards

As mentioned above, in atomic clocks, a defined atomic transition is used as frequency reference. Practically, we measure the absorption, by one or more atoms, of the radiation coming

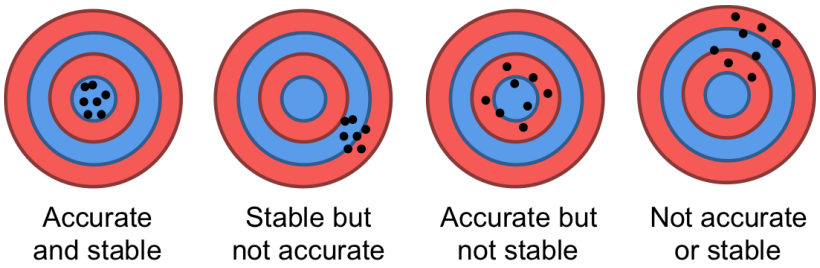

Figure 1.1: Schematic of measurement accuracy and instability.

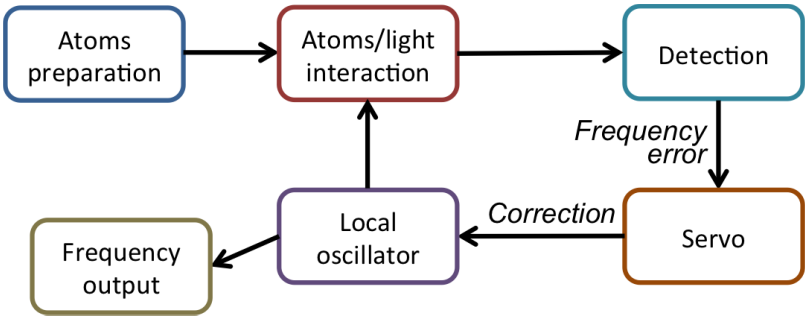

Figure 1.2: Basic scheme of an atomic clock. At first the atoms are prepared in the initial state (ground state). After the interaction with the light coming from the local oscillator (i.e. maser or laser) the excitation probability fraction is detected, deriving the frequency offset between the local oscillator and the atomic transition frequency. A servo generates the error signal used for the correction of the local oscillator frequency.

from a highly stable local oscillator (which can be a laser or a maser, in microwave clocks). Using the signal obtained from the atoms interrogation, with a feedback loop, one can stabilize the frequency of the laser to the one of the atomic clock transition, correcting in this way the long term drift of the laser (Figure 1.2).

The atoms preparation is really important: for high accuracy spectroscopy the atoms needs to be cooled down to near absolute zero temperatures, in order to reduce the Doppler effect due to atoms motion. Laser cooling techniques were introduced in the eighties, allowing the realization of the first atomic fountain [4]: atoms, cooled at a temperature of few μK, are launched upwards and, following a ballistic trajectory, fall down due to gravity, passing twice through the interrogation region (microwave cavity), with a dark time T_D in between the two interrogations. This is named as Ramsey spectroscopy [5] and allows to increase the interaction time and to reduce the transition linewidth, given by $\Delta\nu \simeq 1/T_D$. In order to reach relative accuracy at the level of low 10^{-16}, atomic fountains need long averaging time and an accurate control of all the systematic shifts of the clock transition: these effects are nowadays

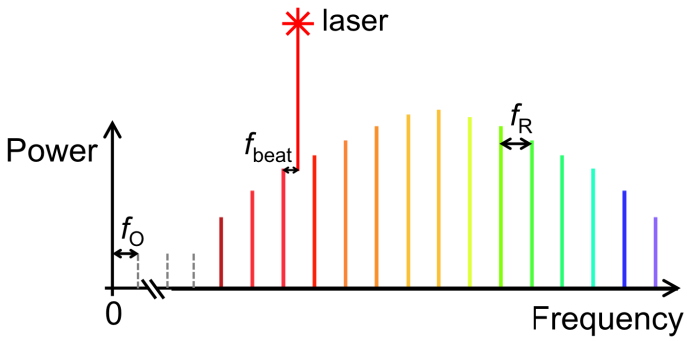

Figure 1.3: Schematic of a frequency comb.

limiting the ultimate accuracy which can be achieved with cesium clocks.

1.1.1 Optical frequency standards

The accuracy of microwave clocks has been exceeded by optical clocks: since in optical clocks the clock transition frequency is 4 to 5 orders of magnitude higher compared with microwave clocks, also the quality factor $Q = \nu_0/\Gamma$, used to characterize the properties of frequency standards, is much higher. This makes easier to achieve better clock instability and accuracy, aiming to the 1×10^{-18} relative level, or below.

Optical clocks development started in the early 2000s, when all the critical technologies had reached maturity. At first, lasers have become more reliable, stable and compact, also thanks to better electronics. The lasers instability can be further improved by stabilizing their frequency to Fabry-Pérot cavities [6], such that the laser frequency noise is only dependent on the cavity length changes: the stabilization is usually done using the Pound-Drever-Hall technique [7], introduced in 1983. Thanks to the improved laser instability, is nowadays possible to interrogate optical transitions with sub-Hz linewidth.

Finally, a key component for optical clocks development, was the invention of the frequency comb in 1999 [8], which simplified the comparison of optical and microwave frequency standards. In fact, previously, complex frequency conversion chains were used in order to down-convert the optical frequencies to a frequency which could be counted using standard electronics. The frequency comb uses a mode-locked laser in order to generate a spectrum of equally spaced sharp lines at a frequency $f_N = nf_R + f_O$, where n is an integer number, f_R is the repetition rate and f_O is an offset (Figure 1.3): both f_R and f_O are known precisely. For the comparison between the frequency of two different lasers, one can measure the beat note f_{beat} between each laser and the tooth of the comb closer to its frequency. With the frequency comb, for example, an optical frequency can be compared directly with

the microwave frequency of a cesium clock.

Optical clocks can be realized using neutral atoms, trapped in an optical lattice, or single ions confined in an electromagnetic trap. Optical lattice clocks can be operated with different species as magnesium [9], strontium [10–14], mercury [15] or ytterbium [16–19]: what makes them good candidates for the realization of optical clocks, as it will be shown in the case of strontium (Section 2.1), is the presence of two valence electrons. However, the optical lattice potential may perturb the frequency of the clock transition: the solution was proposed in 2003 [20], and consists in operating the lattice at the so-called "magic" wavelength, where the clock transition ground and excited states are shifted by the same amount, such that the clock transition frequency is not perturbed (at the first order). Optical lattice clocks has reached instability at low-10^{-16} level at $\tau = 1\,\mathrm{s}$ integration time [21–23]: the lowest value of $6 \times 10^{-17}/\sqrt{\tau}$, was achieved with a two-atom-ensemble system [24]. The lowest uncertainty reported for an optical lattice clock is 1.4×10^{-18} [25].

In ion clocks, the atoms can be trapped in the potential minimum of an electromagnetic trap: consequently most of the systematic shifts are suppressed or can be controlled accurately. The drawback of ion clocks is the fact that only one atom can be trapped and this reduces the signal to noise ratio: this is a limitation for the clock stability. Best ion clocks performances today include $5 \times 10^{-15}/\sqrt{\tau}$ instability and 3.2×10^{-18} inaccuracy [26].

Due to their better performances, the possibility of a redefinition of the SI second based on optical clocks is being investigated. This can be beneficial in the future both for scientific and technological applications. The main requirements for this redefinition are reliability of optical clocks, repeatability of the frequency measurements (including comparison between clocks in different laboratories, see below) and availability of a sufficient number of optical clocks worldwide. Furthermore, one have to choose one or more transitions to be used for the redefinition. As a first step, in 2015 the Bureau International des Poids et Mesures (BIPM) has recommended several optical transitions as secondary representations of the second [27].

1.2 Clock comparisons and transportable clocks

As mentioned above, an important step towards the redefinition of the second based on optical frequencies is to demonstrate the clock frequency measurement repeatability. This means that different clocks have to be compared in order to verify their accuracy. Since optical clocks accuracy is now better compared with the primary standards one, the latter cannot be used as reference, because they would limit the accuracy of the comparison: thus, it is necessary to directly compare optical clocks.

If optical clocks are placed in different laboratories, one can use two approaches: imple-

menting a link between the two clocks, or using a transportable clock. In the first case, the link doesn't have to limit the accuracy of the clock comparison: for optical clocks comparison, this is the case if satellite microwave links are used (with accuracy at low 10^{-16} level [28]). However, telecommunication optical fibers can be used [28–31]: an optical link with a fractional uncertainty at the low 10^{-19} level has been demonstrated, and used for comparing two strontium clocks at a distance of 1400 km, resulting in an agreement at 5×10^{-17} level [28]. A drawback is that optical links need dedicated bi-directional amplifiers every few tens of km in order to compensate for the attenuation in the optical fiber: this makes them not suitable for intercontinental comparisons.

Such comparisons will be possible using transportable clocks which can be moved from one laboratory to another. Furthermore, transportable clocks will allow to overcome one of the possible future fundamental limitation for the measurements via optical link. In fact, when two distant clocks are compared, one needs to know accurately the difference in the gravitational potential between the two sites where the clocks are located, in order to apply the proper correction for the gravitational redshift. This is given in fractional units by $\Delta\nu/\nu_0 = -\Delta U/c^2$, where ΔU is the difference in the gravitational potential. On the Earth surface, an height difference of one meter corresponds to a frequency shift of $\sim 1 \times 10^{-16}$ [32]. Thus, for comparisons at 10^{-18} level the potential needs to be known at centimeter equivalent level, which is close to the state-of-the-art of global geopotential models.

On the other hand, transportable clocks can be used for gravitational potential measurements: this is called as relativistic geodesy or chronometric leveling [33] and can be particularly useful in order to reduce the uncertainty on long distance leveling (i.e. continental and intercontinental distances). For measuring the geopotential, today, different techniques are used, e.g. geometric leveling combined with gravimetry measurements, for shorter distances (hundreds of km), or GNSS data associated with gravity field modelling, which allows comparisons on the intercontinental scale [32]: however, for the latter, the uncertainty on the potential measurement can be between 0.3 and 0.7 m^2/s^2 [34], corresponding to a clock frequency shift up to 7×10^{-18}. With optical clocks accuracy approaching the 1×10^{-18} level, it is clear that the comparison of such clocks worldwide distributed, can contribute to improve the geopotential models.

A transportable strontium optical lattice clock [35], from PTB, has successfully completed two measurements campaigns [36, 37]. In a first campaign the clock was operated at first in the mountain, by comparing it via optical fiber with a laboratory clock placed in Turin (Italy), at a distance of 90 km and an height difference of about 1000 m. Than the clock was moved at the site of the laboratory clock, and the comparison was repeated: the observed frequency shift was consistent with the expected one, as evaluated from geodetic measurement, within

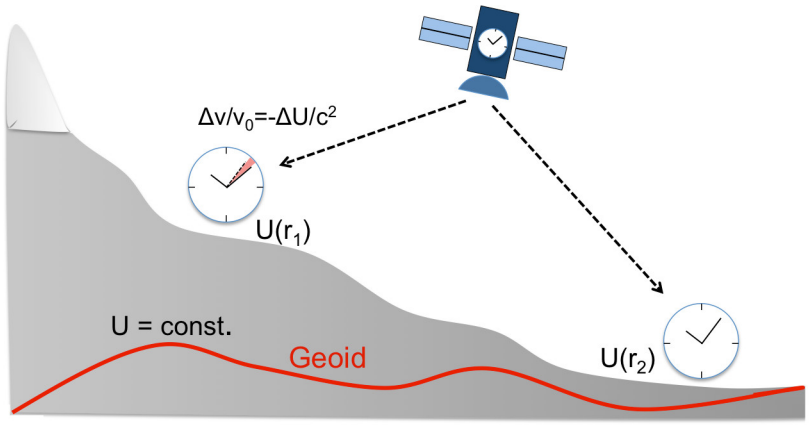

Figure 1.4: Schematic of chronometric leveling performed using a reference clock in space.

the 2×10^{-16} measurement uncertainty.

A better accuracy was achieved using two stationary clocks at 15 km distance in Japan [38]: the frequency shift was measured with an accuracy of 6×10^{-18} (corresponding to ~ 5 cm uncertainty on the height difference), and it was found to be consistent with the shift expected from leveling measurement.

1.3 Atomic clocks in space

The problem of the knowledge of the local gravitational potential can be overcome using a master clock in space. If the orbit of the clock can be determined accurately, than the gravity potential can be evaluated with high precision: therefore, such a clock can be used as reference for distant ground clocks comparisons. This is one of the goals of the ACES (Atomic Clock Ensemble in Space) mission [39], which will operate in the next few years a cesium fountain on the International Space Station (ISS). The clock will be compared with ground based clocks using a microwave link and a newly developed laser link. The comparison can be performed both, in common view (the ground clocks are compared simultaneously), or in non-common view, with the space clock acting as flywheel: this allows clock comparisons worldwide (Figure 1.4). Chronometric leveling can be performed with high accuracy by comparing the space clock with transportable clocks moved to several locations on the Earth's surface: this will contribute establishing a global reference frame for the Earth's gravitational potential. Furthermore, with more accurate reference clocks in space, in the future it will be possible to monitor geophysical effects, such as the motion of the Earth's surface or, in combination with gravitational acceleration data, the changes in the density beneath the Earth's

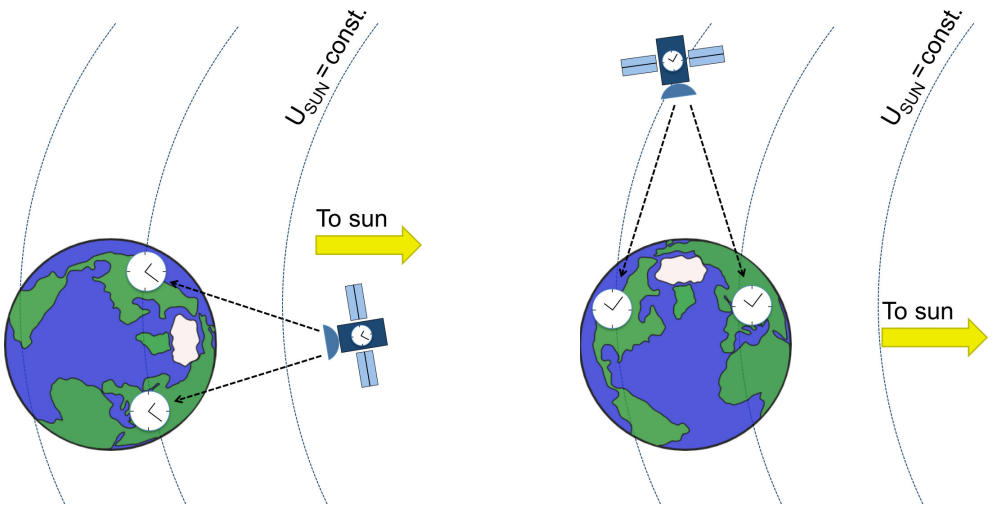

(a) (b)

Figure 1.5: Schematic of the measurement of the time dilation in the Sun's gravitational field, using a space clock as reference for comparing distant clocks on the ground. a) $U_{\mathrm{SUN}}(r_1) = U_{\mathrm{SUN}}(r_2)$; b) $U_{\mathrm{SUN}}(r_1) \neq U_{\mathrm{SUN}}(r_2)$.

surface, which may be connected to underground water or magma movements. This data can be really important in studies such as on volcanoes or earthquakes.

Other important applications of space clocks are in the field of fundamental physics. These include, for example:

- Gravitational Red-shift measurement: this can be performed exploiting the sensitivity of atomic clocks to gravitational potential differences, and provides a test for theory of general relativity. If, for example, a clock is placed on an elliptical orbit, one can use reference clocks on ground in order to measure the clock frequency dependence on the position in the gravitational field, which can than be compared to theory.

- Test of the equivalence principle in the Sun's gravitational field: as detailed in [40, 41], the effect of the Sun's potential is not seen in the comparison between ground clocks, due to cancellation between the gravitational effect of the Sun and the relativistic Doppler shift due to the Earth's motion. Using the space clock as reference, it is possible to compare ground clocks with different orientations with respect to the Sun (Figure 1.5): in this way, since the Doppler shift effect is precisely known, one can study the time dilation effects in Sun's gravitational potential [42]. In particular, when the two clocks are at the same distance from the Sun (Figure 1.5a), they experience the same potential: therefore, the measured frequency offset is due to the difference in the Earth's gravitation potential at the position of the two clocks (see Figure 1.4). While, if the two

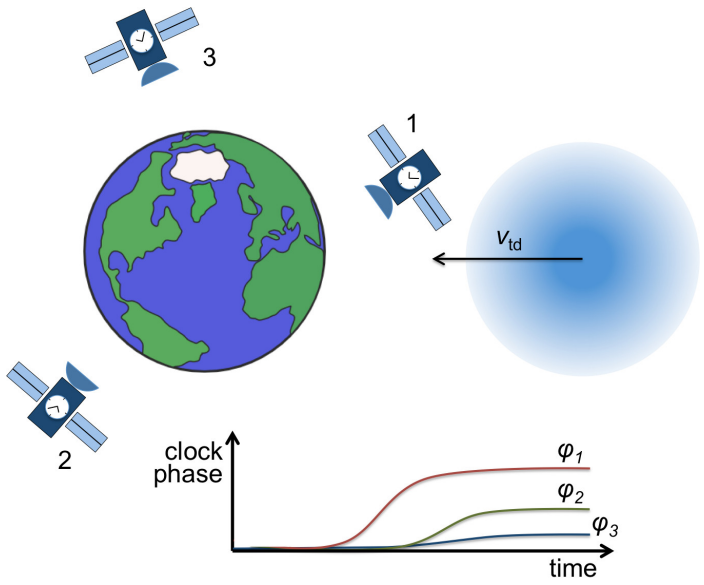

Figure 1.6: Schematic of the detection of a dark matter topological defect, moving with velocity v_{td} across the Earth, by a network of space clocks (after [43]).

clocks are at a different distance (Figure 1.5b) they experience a different potential, but this is expected to be cancelled by the relativistic Doppler shift contribution.

- Drift of fundamental constants: in particular, the strength of the electromagnetic interaction depends on the fine structure constant α. Clocks operated with different species will have a different sensitivity to changes of α [44]: therefore, comparing different clocks worldwide, and repeating the measurements over time (every few months or years), would allow to investigate a possible variation in time of the fine structure constant.

- Search for particles and fields: as suggested in [43], dark matter topological defects crossing the Earth would induce a transient in the value of fundamental constants. This results in a differential phase shift between distant clocks. In the future, a network of high performance clocks in space will allow to detect such defects and eventually to study their space structure (Figure 1.6).

1.4 The Space Optical Clock project

The Space Optical Clock project [45], funded by ESA and coordinated by Prof. Schiller (Heinrich-Heine-Universität Düsseldorf), started in 2007, as a preliminary study of the feasibility of an optical lattice clock to be operated in space. This represents the natural follow-on

mission of the ACES mission: by exploiting the advantages of optical clocks over microwave clocks, SOC aims to achieve at least one order of magnitude better performances (i.e. instability and inaccuracy) compared with ACES. Compared with laboratory based clocks, novel solutions needs to be investigated in order to reduce the mass, volume and power consumption. As a first step, a compact transportable clock demonstrator was realized in Florence (Italy) [46]: the main features of the system were a compact vacuum system, an high efficiency atomic oven, commercial diode lasers, and compact laser optical breadboards interconnected, and connected to the main vacuum chamber, via optical fibers [47].

As follow-on of this preliminary study, in 2011 a second stage of the project was started (named as SOC2 project): this was a collaboration between 16 institutions, companies and universities. The goal of the project, was the development of two transportable optical lattice clock apparatus, one based on strontium atoms [42] and one on ytterbium atoms [48], with a volume below 1 m^3 and an instability and inaccuracy better than $1 \times 10^{-15}/\sqrt{\tau}$ and 5×10^{-17}, respectively. The strontium clock atomic system was realized at the University of Birmingham, using some of the laser modules developed for the first generation SOC clock: these consist in six laser systems from Toptica Photonics, with distribution breadboards from University of Birmingham (blue laser), PTB (red cooling laser) and University of Florence (repumpers and lattice lasers), and a frequency stabilization system (FSS) from the University of Düsseldorf. In June 2015, after successful characterization of the optical lattice trap, the system was moved to PTB (Braunschweig) for the implementation of the clock laser (from SYRTE, Paris). At PTB the clock characterization and further development has been ongoing, funded partially by the Marie Curie action Future Atomic Clock Technology (FACT) and, since March 2017, in the framework of the I-SOC ESA mission.

1.5 Motivation and outline of the thesis

As it will be shown in Section 2.4, two strontium isotopes are used for the realization of optical lattice clocks, ^{88}Sr (boson) and ^{87}Sr (fermion). The fermionic isotope presents advantages for accuracy evaluation, and all the high performance strontium lattice clocks worldwide are based on this isotope. For the same reason this is the primary choice for the operation of the space optical clock for the I-SOC mission. On the other hand, the bosonic isotope presents advantages in terms of simplicity (such as absence of nuclear spin and much higher isotopic abundance) and reliability, which may be of interest for transportable clock applications and, eventually, for timescales realization. Furthermore, in the framework of the I-SOC project, ^{88}Sr is a back-up option in case of degraded operation of some of the clock subsystems (e.g. lasers, vacuum level, etc.).

For this reason, in this work, it was decided to investigate ^{88}Sr clock, and the possible solutions in order to overcome the limitations of bosonic clocks: this allowed also to gain experience which can be useful for the design of the space clock.

The work reported in this Thesis started at the University of Birmingham in September 2014, with the optimization of the atoms cooling and trapping in the optical lattice. After the atomic package was transported to PTB (June 2015), the ^{88}Sr clock transition was observed in late 2015 and the full characterization of the clock performances, including comparisons against the ^{87}Sr PTB clock, was successfully concluded in late 2017.

In Chapter 2 is given an introduction on strontium properties, atoms cooling and trapping techniques and trap characterization; the disadvantages of bosonic clocks compared with the fermionic ones will be discussed. Chapter 3 describes the experimental apparatus. In Chapter 4 is shown how the shifts which are characteristic of bosonic clocks are controlled in order to improve the clock instability; the result of the clock instability comparison with the PTB ^{87}Sr clock is reported. In Chapter 5 is described the evaluation of the clock uncertainty budget and the measurement of the ^{88}Sr-^{87}Sr isotope shift. Finally, in Chapter 6, the results and outlook are discussed.

Chapter 2

Strontium optical lattice clock

2.1 Strontium atoms

Strontium is an alkali earth metal with four stable isotopes, one fermion and three bosons (Table 2.1). The two isotopes used for optical clocks are ^{88}Sr and ^{87}Sr.

Strontium presents two valence electrons: the resulting mixture of singlet and triplet spin states, makes it a good candidate for the realization of optical clocks.

In Figure 2.1 is shown the energy diagram, with the transitions of interest: we label the states using the Russell-Saunders notation $^{2S+1}L_J$, with S total spin of the two electrons, L orbital quantum number and J total angular momentum. The strong dipole allowed transition $^1\mathrm{S}_0 - ^1\mathrm{P}_1$ (at 461 nm) is used for a first cooling stage. There is no allowed transition between the $^1\mathrm{S}_0$ state and the triplet state ^{3}P, due to electric dipole selection rules. However, thanks to the angular momentum state mixing ($L \cdot S$), the $^1\mathrm{S}_0 - ^3\mathrm{P}_1$ transition (689 nm) is observed as intercombination transition between $^3\mathrm{P}_1$ and $^1\mathrm{P}_1$ states [50]: this transition is used for the second stage cooling of the atoms. The $^1\mathrm{S}_0 - ^3\mathrm{P}_0$ transition is the clock transition: this is doubly forbidden ($\Delta S = 1$ and $J = 0 \rightarrow J' = 0$). However in ^{87}Sr the hyperfine interaction, due to the nuclear spin, introduces a state mixing between the $^3\mathrm{P}_0$ and the $^1\mathrm{P}_1$ state: as result, the transition is weakly allowed, with a transition linewidth of ~ 1 mHz. In the bosonic isotope, one can induce a coupling between the $^1\mathrm{S}_0$ and $^3\mathrm{P}_0$ states, by introducing a strong homogeneous

Isotope	Natural abundance	Nuclear spin
^{84}Sr	0.56%	0
^{86}Sr	9.86%	0
^{87}Sr	7.00%	9/2
^{88}Sr	82.58%	0

Table 2.1: Properties of the stable isotopes of strontium [49].

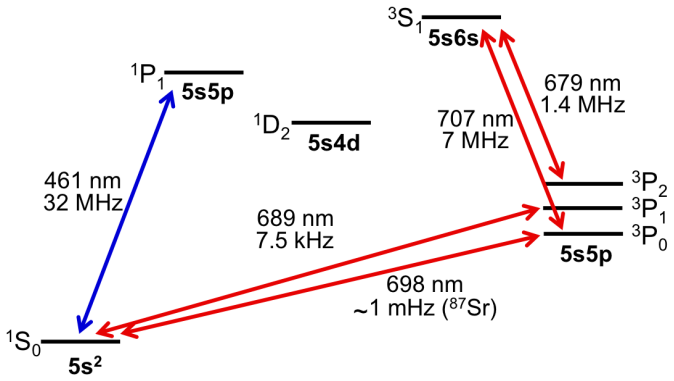

Figure 2.1: Scheme of strontium relevant energy levels and transitions (not to scale).

magnetic field (combined with a rather high interrogation beam intensity), in order to produce admixing of the $^3P_1$ and $^3P_0$ states: this is called magnetically induced spectroscopy [51] (see Section 2.4.1).

Two more transitions are of interest for Sr clocks: the $^3P_2 - {}^3S_1$ (707 nm) and the $^3P_0 - {}^3S_1$ (679 nm). These are used in order to remove the atoms from the $^3P_0$ and $^3P_2$ states: from the $^3S_1$ state the atoms can decay to one of the ^3P_j states and either spontaneously decay to the ground state (if in $^3P_1$) or be excited again to the $^3S_1$ state (if in $^3P_0$ or $^3P_2$). This process, called repumping, is used during the first stage cooling, in order to improve the cooling efficiency, and during the detection phase, for measuring the population of the clock transition excited state ($^3P_0$, which presents a lifetime of ~ 100 s) after interrogation, by repumping the atoms to the ground state and than detecting them using the 461 nm light.

2.2 Atoms cooling and trapping

The main perturbations of the transition frequency of a not confined atom are the 1st-order Doppler shift, due to the atoms' motion, and the photon recoil effect, associated with the absorption of a photon from the interrogation beam: in order to eliminate these effects, the atoms need to be cooled and trapped. This is done in two steps: at first atoms are cooled down to a temperature of few μK in a magneto optical trap (MOT). Than, they are trapped in an optical lattice: being confined in a region smaller than the clock laser wavelength (Lamb-Dick regime), the recoil energy associated with the atom-light interaction, is absorbed by the confining potential (see below). Another advantage is that the atoms can stay trapped in the lattice for many seconds, allowing for increased clock transition interrogation times.

The radiation pressure force for an atom in a laser field is given by [52]:

$$F = \hbar k \frac{\Gamma}{2} \frac{I/I_S}{1 + I/I_S + (2\delta/\Gamma)^2}, \tag{2.1}$$

where k is the radiation wavevector, Γ is the transition linewidth, I is the light intensity, δ is the detuning from resonance and $I_S = \hbar c k^3 \Gamma/(12\pi)$ is the saturation intensity. Let's consider an atom moving in a region with two counterpropagating laser beams, red-detuned from resonance: due to Doppler effect the light will be closer to resonance, and thus the absorption rate will be higher, in case the atom is moving towards one of the beam, while it will be lower for the copropagating beam. This results in an imbalance of forces which depends on the velocity v of the atom as:

$$F_\pm = \pm \hbar k \frac{\Gamma}{2} \frac{I/I_S}{1 + I/I_S + (2(\delta \mp kv)/\Gamma)^2}, \tag{2.2}$$

where F_+ refers to the copropagating beam and F_- to the counterpropagating beam: as consequence the atom is slowed down. In order to reduce the atoms velocity in the three spatial directions, three pairs of counterpropagating beams are used: this is referred as optical molasses. The cooling process is limited by the atoms spontaneous emission of the absorbed photons: this limit results from the equilibrium between the cooling process and the heating, from photon recoil. The minimum temperature (Doppler limit) is given by $T_D = \hbar\Gamma/(2k_B)$. As it can be seen, this depends on the transition linewidth: for example it results 0.76 mK for the $^1S_0 - ^1P_1$ transition and 0.18 μK for the $^1S_0 - ^3P_1$ transition.

In order to trap the atoms, while they are being cooled, a MOT is used. A magnetic field gradient is applied: in this case the detuning for the two laser beams can be rewritten as $\delta_\pm = \delta \mp kv \pm (\mu' B/\hbar)$ (the sign depends on the polarization of the beams, see below), where B is the magnetic field and μ' is the magnetic dipole moment [52]. For a transition $J_g = 0 \rightarrow J_e = 1$, this introduces a splitting of the excited state in three states with angular momentum $M_J = 0, +1, -1$ (Figure 2.2). The energy difference between these three states increases with the distance from the center of the trap. If the two counterpropagating beams have opposite circular polarization (σ_+ and σ_-), due to selection rules for momentum transfer, the $M_g \rightarrow M_e = +1$ transition is excited only by the σ_+ beam, while the $M_g \rightarrow M_e = -1$ transition is excited only by the σ_- beam. Thus, with reference to Figure 2.2, an atom on the right side will absorb more likely a photon from the σ_- beam and vice-versa: the result is a net force, which drives the atoms towards the center of the trap.

Experimentally, we use a pair of coils in anti-Helmholtz configuration (MOT coils) in order to produce the magnetic field gradient (of the order of 40–50 G/cm for the first stage MOT). The six MOT beams are generated by retro-reflecting three beams, in the three spatial

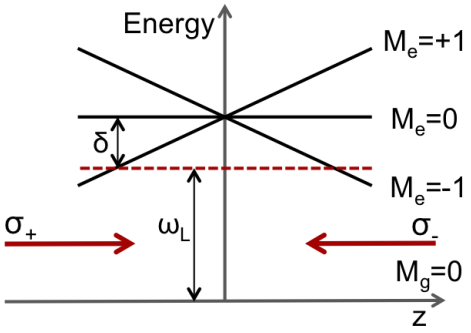

Figure 2.2: Scheme of a 1-D MOT.

directions, with a diameter of 10 mm and a maximum intensity of the order of ~ 6 mW/cm^2 and ~ 2 mW/cm^2 for the first and second stage MOT, respectively: the diameter of the beams, together with the magnetic field gradient, defines the size of the trapping region and thus also the maximum atoms' capture velocity. As mentioned in Section 2.1, during this stage, two additional beams (repumpers) are needed, in order to increase the cooling efficiency.

For increasing the trapping efficiency, the atoms coming from the oven, at a temperature of $\sim 350-400$ °C (corresponding to a velocity of about $\sim 400-450$ m/s) are slowed down before to reach the trapping region, using a counterpropagating laser beam at 461 nm (slower beam), red-detuned from the $^1S_0 - ^1P_1$ transition by about 400 MHz. In order to keep the atoms in resonance during the slowing process, a variable magnetic field is introduced, which compensates for the changes in the Doppler shift.

After a first stage of cooling, using the $^1S_0 - ^1P_1$ transition, up to few 10^6 atoms can be trapped at a temperature of 2-3 mK [53]. As it can be seen in Figure 2.3, showing the clock timing diagram, after few hundreds ms of loading into the first stage MOT, the atoms are cooled down, by reducing the beams intensity, and transferred into the second stage MOT ($^1S_0 - ^3P_1$ transition): since the transition linewidth is really small (7.5 kHz), in order to cover the velocity distribution of the atoms in the first stage MOT, the frequency of the 689 nm laser needs to be modulated during the transfer. Afterwards, the modulation is switched off, and the intensity of the red beams is ramped down to < 10 μW/cm^2: the final temperature of the atoms is few μK and the total number of atoms is $\sim 10^5$ [53].

At the end of the second stage of cooling the MOT beams are switched off and the atoms are trapped in the optical lattice: this consists in a standing wave, obtained by retro-reflecting a laser beam with rather high intensity. The spatial modulation of the field intensity along the beam propagation axis z is given by $I(z) = 4I_0 cos^2(k_L z)$: this modulation confines the atoms in the longitudinal direction (Figure 2.4a). In order to confine them also in the transverse direction r, the beam is focused at the center of the trap, such that, assuming a Gaussian

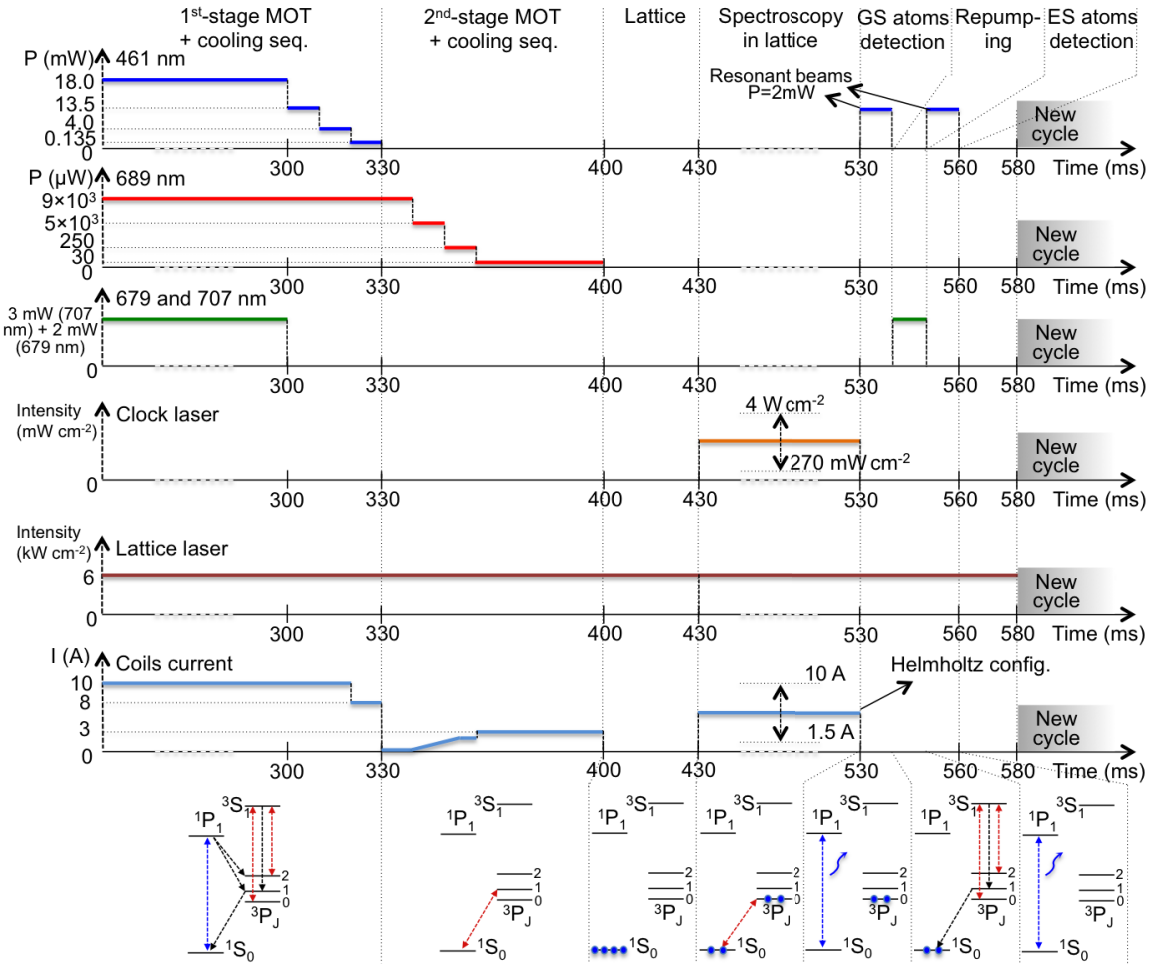

Figure 2.3: Clock timing diagram, including cooling, trapping into the lattice, clock transition interrogation and excited state fraction detection (modified from Figure 5 in [54]). The duration of the atom loading into the first stage MOT can be changed from few hundreds ms up to 1 s, depending on the operating conditions. As explained in Section 4.2, also the duration of the spectroscopy may vary from few tens of ms to few seconds.

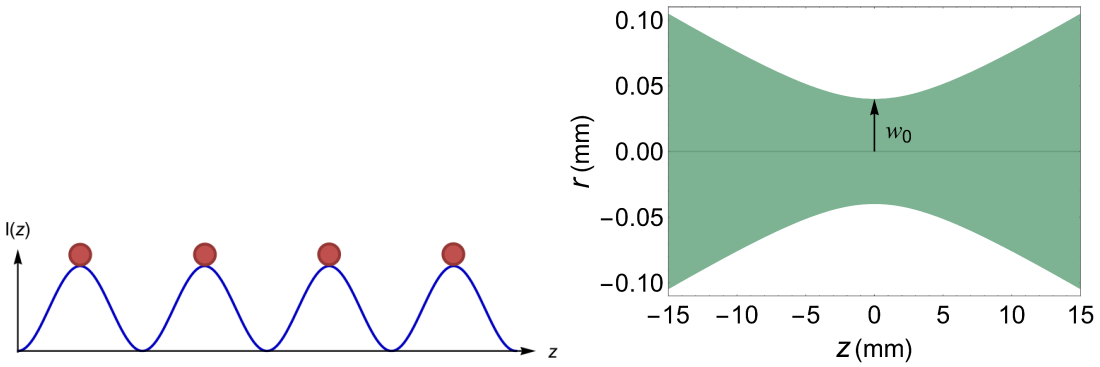

(a) (b)

Figure 2.4: a) Schematic of the lattice potential with atoms trapped at the maximum of the standing wave ($\omega_L < \omega_0$). b) Schematic of the Gaussian profile of the lattice beam, with waist size $w_0 = 40\ \mu$m.

profile (Figure 2.4b), the resulting potential can be written as:

$$U(r,z) = -U_0 e^{-2r^2/w_0^2} \cos^2(k_L z), \tag{2.3}$$

where U_0 is the peak trap depth:

$$U_0 = \frac{\hbar\Gamma}{2} \frac{\Gamma}{(\omega_0 - \omega_L)} \frac{I_0}{I_S}, \tag{2.4}$$

and k_L is the lattice wavenumber, w_0 is the lattice waist, ω_0 is the clock transition frequency and ω_L is the lattice frequency. Therefore the atoms are trapped at the maximum of the potential if $\omega_L < \omega_0$ and at the minimum when $\omega_L > \omega_0$. For strontium, a lattice wavelength of 813 nm is used (the so called magic wavelength, see Section 5.5), thus $\omega_L < \omega_0$.

In our experiment, the waist size is $w_0 \simeq 40\ \mu$m. The power of the beam is between 120 and 240 mW (depending on operational conditions). Up to few thousand atoms can be trapped in the lattice, with a temperature of $\sim 2\ \mu$K [53].

2.3 Clock spectroscopy and trap characterization

The beam used for the clock transition interrogation is co-propagating with the lattice beam. This means that the motional effects that we observe in the spectroscopy are mainly related to the motion in the axial direction (z-axis). Since the potential depth is higher than the atoms temperature ($U_0 > k_B T$, where T is the temperature of the atoms), the atoms motion can be described as a quantized harmonic oscillator, with oscillation frequency ω_z (Figure 2.5). The

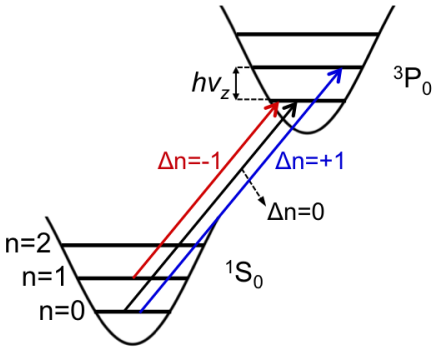

Figure 2.5: Schematic of the vibration energy levels in the lattice.

resulting absorption spectrum can be written as:

$$\nu = \nu_0 \pm m\frac{\omega_z}{2\pi}, \tag{2.5}$$

where ν_0 is the frequency of the carrier transition. If the trap frequency ω_z is much smaller compared with the clock transition linewidth Γ, the motional sidebands are well resolved from the carrier: this corresponds to the well-resolved sideband regime (see next section). In particular, with reference to Figure 2.5, the transition corresponding to $\Delta n = -1$ is called red sideband, while the one corresponding to $\Delta n = +1$ is the blue sideband.

If the atoms are confined in a space z_0 much shorter compared with the clock laser wavelength λ_0, we are in the so-called Lamb-Dicke regime [55]. By introducing the Lamb-Dicke parameter $\eta = 2\pi z_0/\lambda_0$, which can be expressed in terms of oscillation frequency and recoil frequency $\omega_r = \hbar\omega_0^2/(2Mc^2)$ (ω_0 being the frequency of the absorbed photon and M the atom mass) as:

$$\eta = \sqrt{\frac{\omega_r}{\omega_z}}, \tag{2.6}$$

the Lamb-Dicke regime is realized when $\eta\sqrt{\langle n+1\rangle} \ll 1$, with n vibrational quantum number. In this condition, the recoil energy associated with the absorption of photons by the atoms, is absorbed by the confining potential, without any effect on the transition frequency and lineshape.

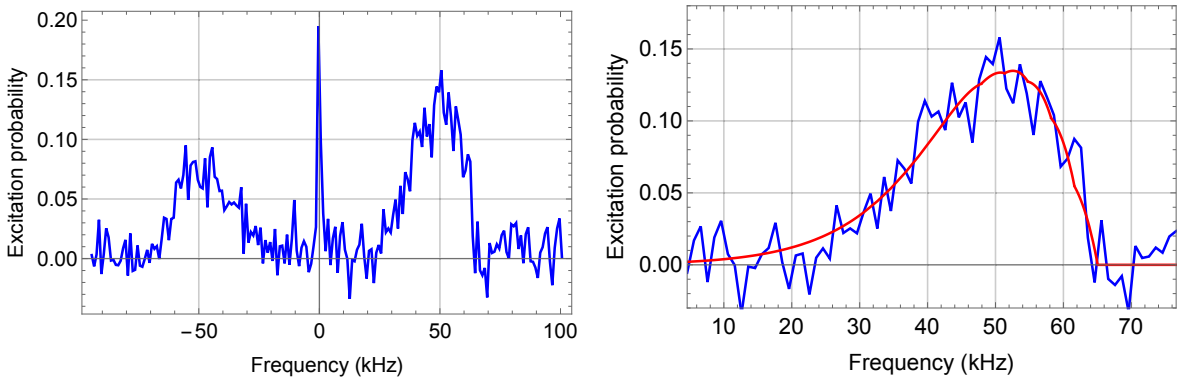

Figure 2.6: a) Sideband spectrum. b) Blue sideband with fit function (red, see text). Resulting trap parameters are: $\nu_z = 68$ kHz, $T_z = 6.4\ \mu$K and $T_r = 7.0\ \mu$K.

2.3.1 Sideband spectroscopy

Sideband spectroscopy can be used in order to characterize the trap parameters, in particular the longitudinal trap frequency [56]:

$$\nu_z = 2\nu_{\mathrm{rec}}\sqrt{\frac{U_0}{h\nu_{\mathrm{rec}}}}, \tag{2.7}$$

with U_0 lattice depth and $\nu_{\mathrm{rec}} = h/(2m\lambda_L^2)$ lattice recoil frequency (λ_L is the lattice wavelength). A typical sideband spectrum is shown in Figure 2.6a. From the ratio between the integral of the red sideband (Σ_{red}), and blue sideband (Σ_{blue}) one can evaluate the longitudinal atom temperature T_z as [56]:

$$\frac{\Sigma_{\mathrm{red}}}{\Sigma_{\mathrm{blue}}} = 1 - \frac{e^{-E_0/k_B T_z}}{\sum_{n_z=0}^{N_z} e^{-E_{n_z}/k_B T_z}}, \tag{2.8}$$

where $N_z \simeq \sqrt{\frac{U_0}{4h\nu_{\mathrm{rec}}}}$ is the number of occupied longitudinal states n_z and E_{n_z} is the energy of the state n_z. Figure 2.6b shows the blue sideband fitted with the function [56]:

$$\sigma_{\mathrm{blue}}(\delta) = \left(\sum_{n_z}^{N_z} e^{-E_{n_z}/k_B T_z}\right)^{-1} \sum_{n_z}^{N_z} e^{-E_{n_z}/k_B T_z}\sigma_{\mathrm{blue}}^{n_z}(\delta) \tag{2.9}$$

where $\sigma_{\mathrm{blue}}^{n_z}(\delta)$ is the line shape for a fixed n_z and it is given by:

$$\sigma_{\mathrm{blue}}^{n_z}(\delta) \propto \left[1 - \frac{\delta}{\widetilde{\gamma}(n_z)}\right] e^{-\alpha[1-\delta/\widetilde{\gamma}(n_z)]}\Theta\left[\widetilde{\gamma}(n_z) - \delta\right], \tag{2.10}$$

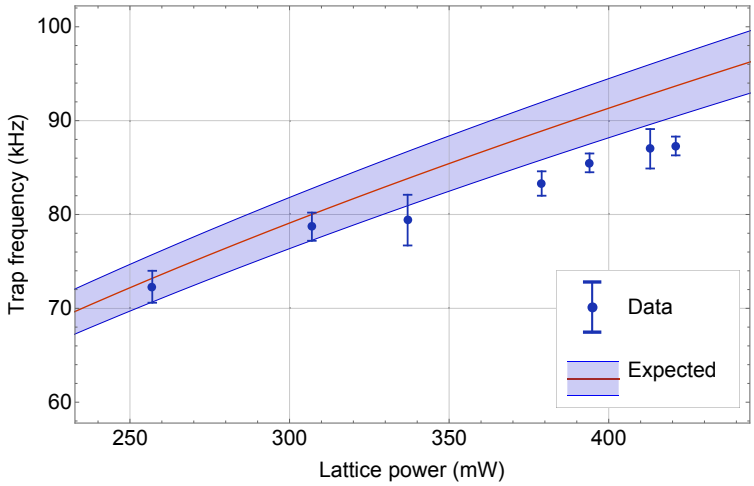

Figure 2.7: Comparison between the measured trap frequency and the one evaluated from the lattice parameters.

with $\alpha \equiv [\widetilde{\gamma}(n_z)/\nu_{\mathrm{rec}}]\,(h\nu_z/k_{\mathrm{B}}T_{\mathrm{r}})$, $\widetilde{\gamma}(n_z) \equiv \nu_z - \nu_{\mathrm{rec}}(n_z+1)$ and T_{r} radial atom temperature.

The trap frequency measured from the sideband spectrum can be compared with the expected one, as evaluated from Equation 2.7 using the lattice parameters (Figure 2.7). The plot shows a good agreement for lower lattice depth, while for deeper lattice the measured values are lower compared with the expected ones. This may be due to the fact that, the deeper is the lattice, the larger is the trapping volume: thus, some of the atoms may be trapped farer away from the lattice waist and experience a smaller potential.

2.3.2 Lattice lifetime

Atoms may leave the lattice due to absorption of lattice photons (even though the laser is far detuned from any strontium transition), or collisions with background gas. The first effect limits the lattice lifetime to many seconds, depending on operating conditions [57]. The atom loss rate due to background particle collisions depends on the density of the background gas (and thus, on the pressure of the vacuum system), and on the interaction potentials between the Sr atoms and the background particles.

A strong dependence of the lifetime on the vacuum system pressure was observed experimentally: initially, when only a small 2 l ion pump was implemented on the main chamber side of the vacuum system (see Section 3.5), the pressure was close to 1×10^{-9} mbar and the resulting lattice lifetime was smaller than 500 ms (Figure 2.8, red points). After a major improvement of the vacuum system, including the implementation of a new ion getter pump, the pressure reduced close to 1×10^{-10} mbar, with a typical lattice lifetime above 5.0 s (Figure 2.8, blue points). This allowed to interrogate the atoms for many seconds, as it will be

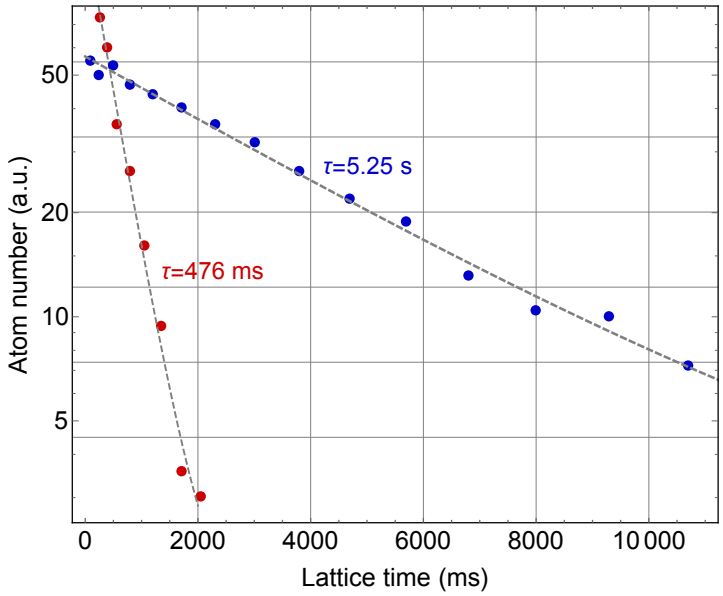

Figure 2.8: Lattice lifetime measured before (red points) and after (blue points) the upgrade of the vacuum system (details in the text).

shown in Section 4.2.

2.4 Bosonic vs. Fermionic strontium clocks

Bosonic clocks presents many advantages compared with fermionic ones, mainly in terms of simplicity. In strontium the isotopic abundance of the bosonic isotope ^{88}Sr (87%) is more than ten times higher compared with the fermionic one ^{87}Sr (7%). This, together with the absence of hyperfine structure, makes the atom cooling easier.

The hyperfine structure complicates also the spectroscopy in fermions: in fact, the presence of an external magnetic field, results in a splitting of the clock transition in ten Zeeman sublevels ($F = 9/2$). One can compensate for this 1$^{\text{st}}$-order Zeeman shift of the clock transition by preparing the atoms in two opposite magnetic sublevels (optical pumping), e.g. $m_g = \pm 9/2$, and using the average frequency of the two components. The presence of the nuclear spin is also the cause of tensor and vector shift in ^{87}Sr (Section 5.5), making it more sensitive to lattice polarization effects and external magnetic field changes.

On the other hand, while for the fermionic isotope the $^1S_0 - ^3P_0$ clock transition presents a finite linewidth of ~ 1 mHz, in bosons it is completely forbidden, making it necessary to introduce an external field in order to induce the coupling between the $^3P_0$ state and another electronic state. For example, one can use electromagnetically induced transparency (EIT) [58], where a strong light field induces the coupling between the $^3P_0$ and the broad $^1P_1$ state, while

a second laser probes the clock transition; or three-photon EIT [59], using two light fields for inducing the coupling. In our case, we implemented magnetically induced spectroscopy [51] where, instead of a light field, a relatively large bias magnetic field is introduced, which mixes a fraction of the $^3P_1$ state into the $^3P_0$ state (see next section).

An additional disadvantage of bosonic clocks is the presence of *s*-wave collisions, suppressed for spin-polarized fermions, and which may cause decoherence effects as well as a significant frequency shift of the clock transition (Section 2.4.2).

Table 2.2 gives an overview of Sr lattice clocks reported in the literature.

2.4.1 Magnetically induced spectroscopy

In magnetically induced spectroscopy, in order to excite the clock transition $^1S_0-^3P_0$ at a frequency ω_{21}, we introduce a static bias magnetic field $\mathbf{B}$, which couples the $\left|^3P_0\right\rangle$ and $\left|^3P_1\right\rangle$ states [51] (Figure 2.9). The $\left|^3P_0\right\rangle$ state acquires a small admixture of the $\left|^3P_1\right\rangle$ state, leading to a first order perturbed state:

$$\left|^3P_0'\right\rangle = \left|^3P_0\right\rangle + \frac{\Omega_B}{\Delta_{32}}\left|^3P_1\right\rangle, \tag{2.11}$$

where $\Omega_B = \left\langle ^3P_0\right|\hat{\mu}\cdot\mathbf{B}\left|^3P_1\right\rangle/\hbar$ is the coupling matrix element between the two states, $\hat{\mu}$ is the magnetic-dipole operator and Δ_{32} is the hyperfine splitting between the two states. The result is that the $^1S_0-^3P_0$ transition becomes weakly allowed, and can be excited by an electric field $\mathbf{E}$ at a frequency ω. The corresponding coupling matrix element can be written as $\Omega_L = \left\langle ^3P_1\right|\hat{\mathbf{d}}\cdot E\left|^1S_0\right\rangle/\hbar$, where $\hat{\mathbf{d}}$ is the electric dipole operator.

The resulting Rabi frequency for the $^1S_0-^3P_0$ clock transition is:

$$\Omega_{12} = \frac{\Omega_L\Omega_B}{\Delta_{32}}. \tag{2.12}$$

Assuming that the bias field $\mathbf{B}$ and the optical field $\mathbf{E}$ are parallel, and using the values for $\langle\|\mu\|\rangle$, $\langle\|d\|\rangle$ and Δ_{32} for strontium as given in [51], the Rabi frequency can be written as $\Omega_R = \alpha\sqrt{I}\,|\mathbf{B}|$, where the coupling coefficient α results $198\,\mathrm{Hz}/\left(\mathrm{T}\sqrt{\mathrm{mW/cm^2}}\right)$ and I is the light field intensity. When high Rabi frequency is required (e.g. for sideband spectroscopy, $\Omega_R > 10^2$ Hz), typical values for I and $|\mathbf{B}|$ are $\sim$1.2 W/cm^2 and 20 to 60 mT, respectively. As it will be shown in Section 4.2, the minimum Rabi frequency we worked with is $\Omega_R \simeq 0.125$ Hz: in that case we used $I \simeq 23$ mW/cm^2 and $|\mathbf{B}| \simeq 0.2$ mT. The Rabi frequency can also be expressed in terms of π pulse interrogation time T_π as:

$$\Omega_R = \alpha\sqrt{I}\,|\mathbf{B}| = 1/2T_\pi. \tag{2.13}$$

institute	*isotope*	*uncertainty*	*instability*	*comment*	*most recent publication*
PTB (DE)	^{87}Sr	2.6×10^{-17}	$1.6 \times 10^{-16}/\sqrt{\tau}$	used as reference in this work	[11, 23, 28]
PTB (DE)	^{87}Sr	7.4×10^{-17}	$1.3 \times 10^{-15}/\sqrt{\tau}$	transportable	[35]
NPL (UK)	^{87}Sr	Not published	$3.2 \times 10^{-15}/\sqrt{\tau}$		[14]
SYRTE (FR)	^{87}Sr	4.1×10^{-17}	$< 3 \times 10^{-15}/\sqrt{\tau}$		[28, 60, 61]
Uni. Tokyo (JPN)	^{88}Sr, ^{87}Sr	^{88}Sr: 5.8×10^{-16}, ^{87}Sr:	$2.8 \times 10^{-15}/\sqrt{\tau}$ combined ^{88}Sr, ^{87}Sr	uncertainty on $\nu(^{88}\text{Sr})$–$\nu(^{87}\text{Sr})$: 2.2×10^{-17}	[62]
RIKEN (JPN)	^{87}Sr (2×)	7.2×10^{-18}	$1.8 \times 10^{-16}/\sqrt{\tau}$	cryogenic. Unc. difference between the two clocks 4.4×10^{-18}	[13]
FAMO (PL)	^{88}Sr (2×)	4.1×10^{-15}, 6.5×10^{-15}	$\sim 3.2 \times 10^{-15}/\sqrt{\tau}$		[63]
JILA (USA)	^{87}Sr	2.1×10^{-18}	$2.2 \times 10^{-16}/\sqrt{\tau}$		[12]
HHU, UoB, PTB et al.	^{88}Sr	2.0×10^{-17}	$4.1 \times 10^{-16}/\sqrt{\tau}$ combined SOC ^{88}Sr, PTB ^{87}Sr	This work. Modular, rack.	[42, 54]

Table 2.2: Overview of currently operating Sr lattice clocks. PTB: Physikalisch Technische Bundesanstalt, Braunschweig (DE); NPL: National Physical Laboratory, Teddington (UK); SYRTE: SYstèmes de Référence Temps Espace (Observatoire de Paris), Paris (FR); University of Tokyo, Tokyo (JPN), RIKEN: Tokyo (JPN); FAMO: Krajowe Laboratorium Fizyki Atomowej, Molekularnej i Optycznej, Toruń (PL); JILA: Joint Institute for Laboratory Astrophysics, Boulder (USA); HHU: Heinrich-Heine-Universität, Düsseldorf (DE); UoB: University of Birmingham, Birmingham (UK).

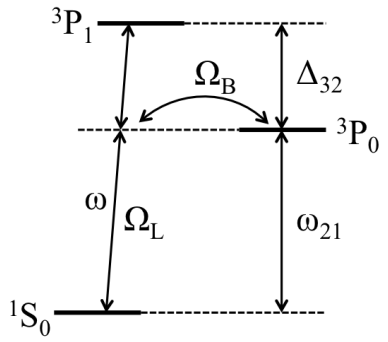

Figure 2.9: Schematic of the magnetically induced spectroscopy.

In Figure 2.10 is shown a typical clock transition acquired using this technique ($\Omega_R \simeq$ 20 Hz). This was one of the first transitions observed in our clock and it represents the best result obtained with the clock laser stabilized only on the SOC2 transportable cavity (see Section 3.4).

The drawback of magnetically induced spectroscopy, is the fact that the external fields induce a shift of the clock transition. The rather high value of these shifts, has so far limited the accuracy of bosonic clocks. For ^{88}Sr, the clock laser AC Stark shift is given by [51]:

$$\Delta\nu_L = \frac{\Omega_L^2}{4\Delta_{32}} = kI, \;\; k = -18 \text{ mHz}/(\text{mW}/\text{cm}^2), \tag{2.14}$$

while the finite magnetic field leads to a 2$^{\text{nd}}$-order Zeeman shift [51]:

$$\Delta\nu_B = -\frac{\Omega_B^2}{\Delta_{32}} = \beta\,|\mathbf{B}|^2, \;\; \beta = -23.8(3) \text{ MHz}/\text{T}^2. \tag{2.15}$$

Using Equation 2.13, we derive that, by choosing $|\mathbf{B}|$ and I optimally, the minimum realizable shift magnitude is $|\Delta\nu_L + \Delta\nu_B|_{\min} = 3.3/T_\pi$. From this expression it is seen that $\Delta\nu_L$ and $\Delta\nu_B$ can be reduced by using increased interrogation times: this will be discussed in more detail in Section 4.2.

2.4.2 Collisional effects in ^{88}Sr

In typical operating condition the density of the atoms trapped in the optical lattice is really small (with maximum few tens of atoms trapped in each lattice well): thus, the interaction between the atoms can be described as two body collisions [64]. For these interactions the wavefunction can be expanded in partial waves with different angular momenta s, p, d,... (correspondingly we speak about s-wave, p-wave, d-wave, ... interactions). Not null angular momenta introduce a rotational kinetic energy of the atom pair which is responsible for a

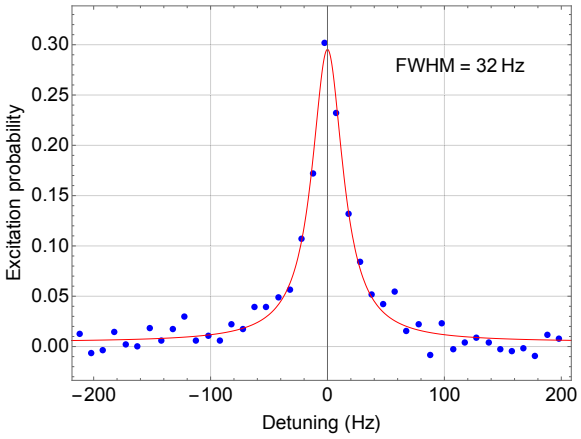

Figure 2.10: Clock transition obtained using only the SOC2 transportable cavity as reference cavity for the clock laser.

centrifugal barrier: for ultracold atoms, this strongly suppress all the partial waves different than s-wave [64].

During the clock transition interrogation, in the lattice are trapped atoms in both ground and excited state. Due to elastic collisions there will be a shift in the energy of the ground and excited state given by [65]:

$$\delta E_{\mathrm{g}} = \frac{4\pi\hbar^2}{m}(g_{\mathrm{gg}}a_{\mathrm{gg}}\rho_{\mathrm{g}} + g_{\mathrm{ge}}a_{\mathrm{ge}}\rho_{\mathrm{e}}), \tag{2.16}$$

$$\delta E_{\mathrm{e}} = \frac{4\pi\hbar^2}{m}(g_{\mathrm{ee}}a_{\mathrm{ee}}\rho_{\mathrm{e}} + g_{\mathrm{ge}}a_{\mathrm{ge}}\rho_{\mathrm{g}}), \tag{2.17}$$

where m is the atomic mass, $a_{i,j}$ is the s-wave scattering length, ρ_{g} and ρ_{e} are the atoms density for ground and excited state, respectively. The two atoms correlation function:

$$g_{ij} = \frac{\left\langle \Psi_i^\dagger \Psi_j^\dagger \Psi_i \Psi_j \right\rangle}{\left\langle \Psi_i^\dagger \Psi_i \right\rangle \left\langle \Psi_j^\dagger \Psi_j \right\rangle}, \tag{2.18}$$

indicates the probability that two atoms are in the same position at a given time. Thus the density dependent frequency shift of the clock transition can be written in Hz as [65]:

$$\Delta\nu_{\mathrm{col}} = \frac{2\hbar}{m}(g_{\mathrm{ge}}a_{\mathrm{ge}}(\rho_{\mathrm{g}} - \rho_{\mathrm{e}}) + g_{\mathrm{ee}}a_{\mathrm{ee}}\rho_{\mathrm{e}} - g_{\mathrm{gg}}a_{\mathrm{gg}}\rho_{\mathrm{g}}). \tag{2.19}$$

Due to the Pauli exclusion principle, indistinguishable fermions do not collide, thus for fermions $g_{\mathrm{g,g}} = g_{\mathrm{e,e}} = 0$; furthermore, if the excitation is driven in a coherent way, the fermions evolution is also indistinguishable (i.e. the electronic degree of freedom remain the same), thus

$g_{g,e} = 0$ [66]. For this reason fermions are, in first approximation, not affected by collisional shift. For bosons, due to exchange symmetry, $g_{g,g} = g_{e,e} = 2$; depending on whether the exchange symmetry is maintained (i.e. by coherent excitation) or not by the excitation process, it results $g_{g,e} = 2$ or $g_{g,e} = 1$, respectively. Thus, in general, the collisional shift is linearly dependent on the total atoms density. However, as shown in [67], this is true for relatively low atoms density: for higher density a saturation is observed, attributed to a changed excitation dynamics.

A second effect due to collisions is density dependent broadening. As shown in [67], in case of inelastic collisions, the atoms loss rate in the lattice is larger for excited state atoms: in fact, these atoms can be lost for collisions either with ground state or with other excited state atoms (in addition to background gas collisions); on the other hand, ground state atoms can only interact with excited state atoms. The different lifetime of the ground and excited state atoms leads to density dependent broadening.

Decoherence effects on the clock transition arise from elastic collisions, leading to a shift of the energy levels of the two colliding atoms. If ν_0 is the frequency of the unperturbed transition, during the interaction the absorbed frequency will be shifted by an amount $\Delta\nu$, which depends on the interaction potential between the atoms. This induces a phase change which leads to an additional broadening of the transition lineshape [68].

All these unwanted effects related to atoms collisions can be reduced, by reducing the atoms density. One way is to trap the atoms in a 2D or 3D lattice [69]: this solution increases the complexity of the atomics system, making it difficult to be applied to a compact transportable apparatus. While a different approach consists in the use of photoassociation (PA) to form Sr_2 molecules from atoms in multiply occupied lattice sites, which then fall out of the lattice [70]: PA was implemented in our setup and results will be discussed in Section 5.4.2. In this work we investigated also a different approach, consisting in loading the atoms in the lattice starting from a slightly warmer (i.e. less dense) red MOT: this allows to spread the atoms over more lattice wells, reducing the number of multiply occupied sites (Section 5.4).

Chapter 3

The experimental apparatus

In this chapter is given an overview of the clock apparatus, including atomic package and clock laser, focusing mainly on the improvements introduced in the framework of this work. In fact, all the laser breadboards, as well as the main vacuum system, were already assembled and operational when I started working on the project: more details, photos and drawings can be found in [42, 53].

3.1 Transportable optical lattice clock

As mentioned in Section 1.4, the clock was built in the framework of the SOC2 project. The goal was to develop a transportable Sr optical lattice clock with $< 1 \times 10^{-15}\tau^{-1/2}$ instability and accuracy below 5×10^{-17} level. Most of the laser breadboards were already in use in Firenze (Italy), for the SOC1 project and than transported to Birmingham (UK). There, the atomic package was developed and the laser breadboards implemented in early 2014. In June 2015, after atoms were trapped in the lattice, the atomic system was housed in a transportable rack (Figure 3.1) and transported by van to PTB (Braunschweig, Germany). At PTB we implemented the transportable clock laser, developed at Syrte (Paris) and transported to Braunschweig few months earlier.

The size of the atomic package, including electronics is $\sim 170 \times 150 \times 60$ cm. It consists of the main vacuum system, the Frequency Stabilization System (FSS) and six laser units: the blue cooling laser, the red cooling and stirring laser, the lattice laser and the repumpers. In Table 3.1 and Table 3.2 are reported the estimated mass and volume budget.

Almost no effort was made to make the electronics more compact or to reduce the power consumption, since this was not part of the project: commercially available electronics is implemented. The only exceptions are the main components of the vacuum system, i.e. the Zeeman slower, the oven and the MOT coils system (see Section 3.5). We measured the power

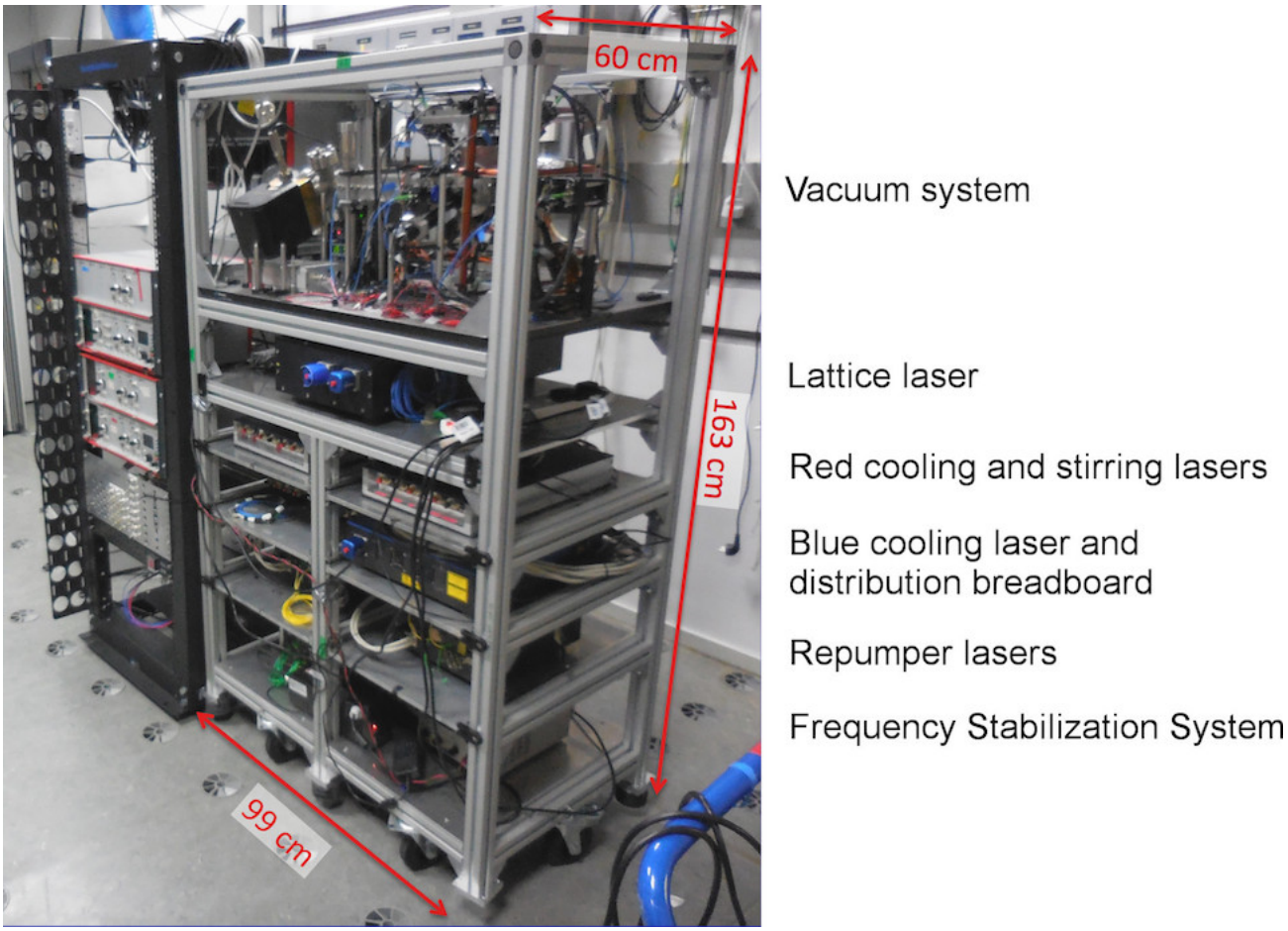

Figure 3.1: Clock atomic package in the transportable rack (right), with electronics (left).

Vacuum system	50 kg
Blue cooling laser	20 kg
Distribution breadboard blue laser	3 kg
Red cooling laser	12 kg
Red stirring laser	12 kg
Lattice laser	30 kg
Repumpers (679+707 nm)	30 kg
FSS	25 kg
Power supplies	30 kg (c.a.)
Electronics	200 kg (c.a.)
Clock laser	20 kg
Clock laser cavity incl. vibration insulation	37 kg
Total	466 kg

Table 3.1: Mass budget of the clock apparatus. This doesn't include the mass of the racks.

Vacuum system	143 l
Blue cooling laser	18 l
Distribution breadboard blue laser	3 l
Red cooling laser	16 l
Red stirring laser	16 l
Lattice laser	20 l
Repumpers (679+707 nm)	20 l
FSS	38 l
Clock laser	90 l (c.a.)
Clock reference cavity incl. vibration insulation	32 l
Electronics	600 l (c.a.)
Total	996 l

Table 3.2: Volume budget of the clock apparatus. The actual size of the system is larger, since it was left some empty space in the atomic package rack in order to allow for easier access to the laser breadboards.

consumption of the main atomic package components: this is reported in Table 3.3. The total power consumption for the clock apparatus (i.e. including clock laser electronics) is expected to be slightly higher than 1 kW.

3.2 Lasers and light distribution

The laser system is made of independent laser and light distribution modules: the lasers, distribution breadboards, FSS and atomic package are interconnected by single mode polarization maintaining optical fibers. The use of a modular laser system allows for easy replacement of the laser modules or distribution breadboards: this can be useful for example if new units have to be implemented or tested. All the laser heads implemented in the atomic package are commercial lasers from Toptica Photonics.

3.2.1 Blue cooling laser

The laser for the first stage cooling (461 nm) is a frequency doubled system (Toptica DL-SHG pro), which can provide up to ~ 400 mW of power at 461 nm. A secondary output at the fundamental wavelength (922 nm) is delivered to the FSS for locking, with a resulting linewidth of less than 1 MHz [71].

The output is fiber coupled and sent to a distribution breadboard (Figure 3.2a): this was designed to be compact (size $25 \times 20 \times 6$ cm) and robust, using commercially available optics and optomechanical components (Appendix A). Here it is splitted in two beams: one is deliv-

Blue laser	145 W
Red cooling laser	62 W
Red stirring laser	58 W
Lattice laser	93 W
Repumpers (679+707 nm)	59 W
FSS	153 W
Amplifiers for AOMs	140 W (ca.)
Oven	20 W
MOT coils	12 W
Total	742 W

Table 3.3: Power consumption of the main atomic package devices. This excludes scopes, computers and clock laser electronics. The total power consumption is expected to be around 1.1-1.2 kW

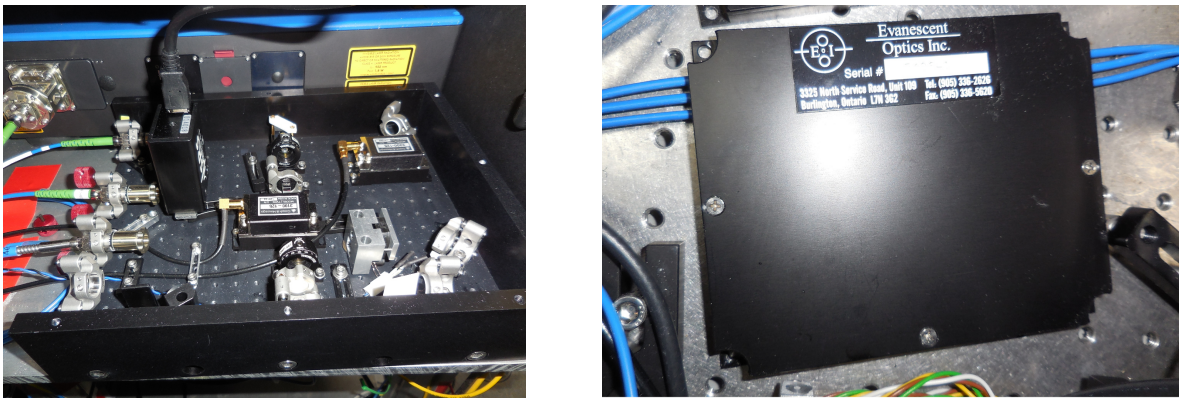

(a) (b)

Figure 3.2: a) Compact blue distribution breadboard (size $25 \times 20 \times 6$ cm), placed in the transportable rack. On the background there is the laser head. The output is delivered to the distribution module via optical fiber. The breadboard has two outputs, for slower and MOT beams. Optionally, an additional output for a detection beam can be implemented. b) Custom made fiber array from Evanescent Optics. The three inputs from blue cooling laser, red cooling and stirring lasers are combined and delivered to the three MOT beams. The size is $12.5 \times 10 \times 1.3$ cm.

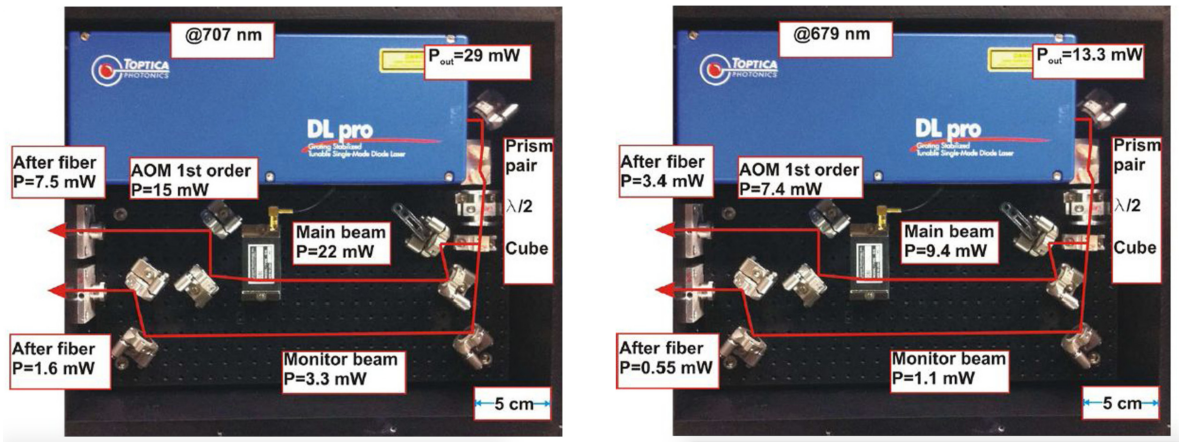

(a) (b)

Figure 3.3: Repumper breadboards [42]: a) 707 nm; b) 679 nm.

ered to the slower beam (power ~ 30 mW), whose frequency is red-detuned with respect to the $^1S_0$-$^1P_1$ transition frequency by about 400 MHz (using a single pass AOM), while the second one (total power ~ 30 mW) is used for the MOT beams (with a double pass AOM, see below), at a frequency ~ 45 MHz red-detuned. The latter is delivered to a custom made fiber array (from Evanescent Optics, Figure 3.2b): this combines the light from the three inputs, from blue cooling, red cooling and stirring lasers, and splits it in three outputs, for the three MOT beams. The use of the fiber array allows to reduce considerably the size of the optical system needed for combining the three beams, since usually this is done using free space optics (beam splitters, dichroic mirrors, etc.). Due to the limited optical access to the main vacuum chamber, the MOT beams are also used for detection (only the two beams in the directions perpendicular to the PMT's optical axis, the third one is closed by a shutter before entering the chamber): this is the reason why a double pass AOM is needed, in order to be able to steer the frequency from the one needed for the MOT beams, to resonance (for detection).

3.2.2 Repumper lasers

The repumpers (707 and 679 nm) are diode lasers (Toptica DL pro) implemented, together with the distribution modules, in two breadboards (size $26.5 \times 32 \times 12.2$ cm^3, mass 15 kg; Figure 3.3). This breadboards provide two outputs each, one delivered to the main vacuum chamber (with about 10 mW each), and one for the wavemeter. The frequency of the lasers is not stabilized, since the passive stability is enough for short measurements (few hours). However it was necessary to implement a stabilization for the 707 nm laser for long term stability: this is done by the computer control program (Section 3.11). The frequency of

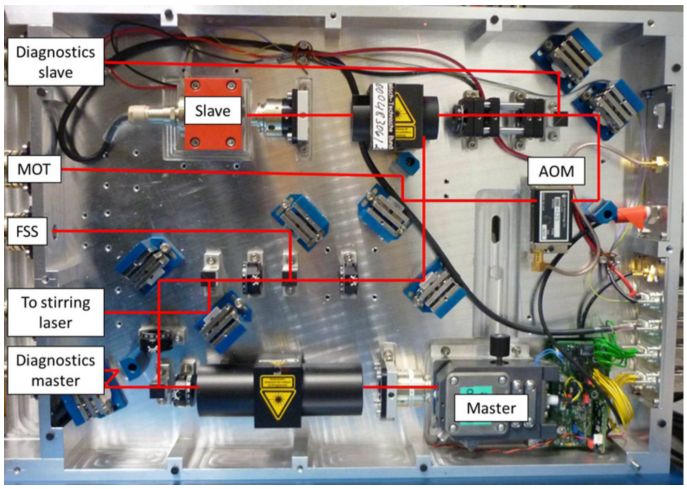

Figure 3.4: Red cooling laser breadboard [42].

the laser is changed (acting on the piezo voltage) by a small step every clock cycle and the program evaluates the difference in terms of number of atoms trapped into the lattice; if the number is higher compared with the previous cycle, in the next cycle the frequency is changed in the same direction, and vice-versa.

3.2.3 Red cooling laser

The red cooling laser (689 nm) is generated by injection locking of a slave laser to a master laser (Toptica DL pro). Both the lasers, without their original housing, are implemented in a custom made breadboard (size $30 \times 45 \times 12$ cm^3; Figure 3.4), developed at PTB. The output of the master is split and one output is delivered to the FSS for locking: when locked, the linewidth is expected to be less than 1 kHz [71]. One additional output can be used for offset locking the stirring laser (for ^{87}Sr) [42]. About 1 mW of power is used for the injection locking, while the slave output power is about 30 mW. An AOM is used for steering the red beams frequency. The output power to the MOT beams is ~ 9 mW. The laser frequency needs to be broadened with a peak to peak amplitude of few MHz during the first phase of the red MOT, in order to address a large range of atomic velocities: this can be done by modulating the FSS sideband frequency [71] (see Section 3.3).

3.2.4 Lattice laser (TA)

The lattice laser is a Master Oscillator Power Amplifier (MOPA) system (Toptica TA pro). The output power is about 1.8 W at 813 nm. The laser is placed in a breadboard (Figures 3.5), including distribution module, whose size is $50 \times 20 \times 20$ cm^3. One output is sent to the atoms

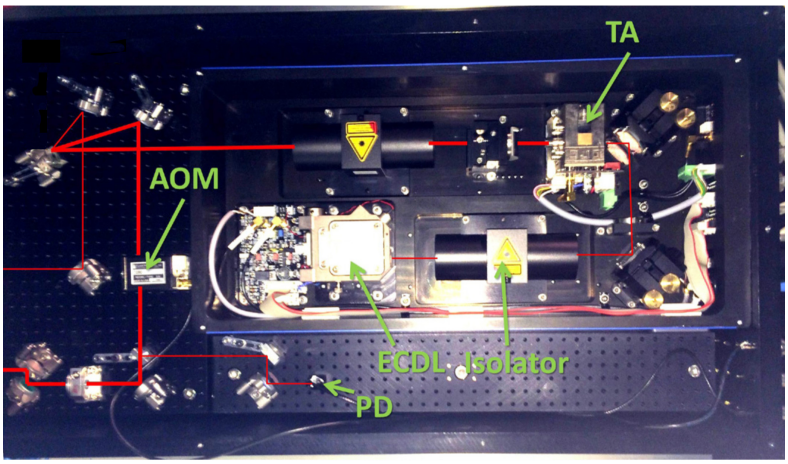

Figure 3.5: Lattice laser breadboard [42].

(up to 500 mW), one to the wavemeter and one to the FSS for locking: the resulting linewidth is smaller than 1 MHz. The breadboard includes an AOM used for intensity stabilization and a photodetector for measuring the power of the back-reflected beam, coupled back into the fiber from the vacuum system: this is used for optimizing the lattice back-reflection alignment (see Section 3.9).

3.2.5 Clock laser

The clock laser (689 nm) is a filter stabilized laser from Leibniz-Universität Hannover, with an output power of 10 mW. The breadboard (Figure 3.6; size $60 \times 45 \times 12$ cm^3) has four outputs. One is delivered to the reference cavity (Section 3.4) for the locking: a double-pass (reference) AOM is used in order to tune the offset frequency between the laser and the reference cavity. A second output is supposed to be delivered to the comb: however, during this work, this was used for phase locking to the PTB Sr system clock laser (Section 3.4): the fiber used for this output is 30 m long and a phase noise cancellation system[1] is needed. A third fiber is used for the wavemeter.

Finally, the forth output delivers up to 1 mW of light to the atomic package using a 10 m fiber: also in this case a phase noise cancellation system is implemented. An AOM is used for frequency steering (clock transition scanning and locking), beam switching and intensity stabilization (Section 4.4.1).

[1] A change in the length of the fiber (for example due to temperature fluctuations or vibrations), may introduce a phase noise in the transmitted light. In order to compensate for this noise, a heterodyne Michelson interferometer is used: a fraction of the light transmitted by the fiber is back-reflected and beated with a reference beam in the clock laser breadboard. The heterodyne beat is used for stabilizing the phase of the transmitted light to the one of the reference beam [72].

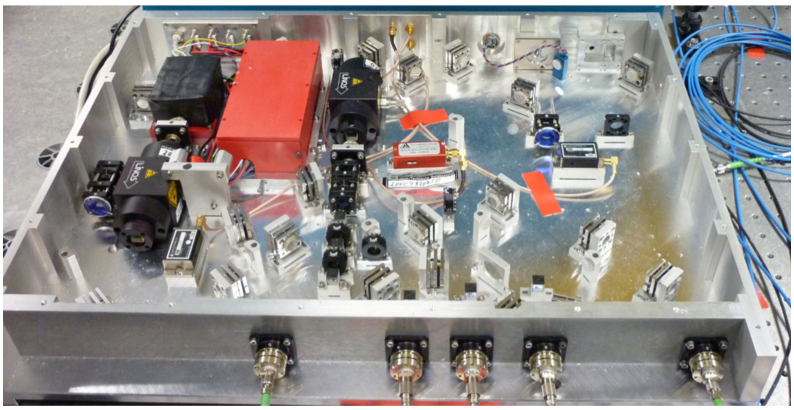

Figure 3.6: Clock laser breadboard.

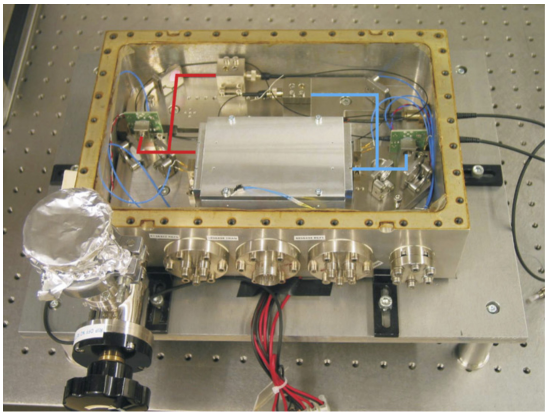

(a)

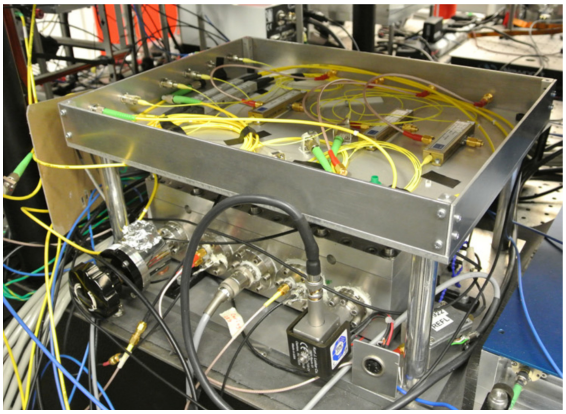

(b)

Figure 3.7: The FSS [42]. a) vacuum chamber with the ULE block; b) complete system, including the box with the EOMs on the top.

3.3 Frequency Stabilization System (FSS)

The FSS, developed at Heinrich-Heine-Universität Düsseldorf [71], is used for stabilizing the lattice laser and the first and second stage cooling lasers. It consists of three cavities implemented in a single ultra-low expansion (ULE) block: this is placed in a vacuum housing of size $30 \times 20 \times 7$ cm^3 (Figure 3.7a). In principle, on each cavity two lasers can be stabilized: 813 and 922 nm, 689 and 698 nm, 679 and 707 nm. However, only the 813 nm, 922 nm and 689 nm stabilizations are implemented at the moment, since the repumpers (679 and 707 nm) doesn't need to be stabilized (see Section 3.2.2) and the clock laser is stabilized to a more stable cavity (Section 3.4).

For the tuning of the offset frequency ω_{off} between the laser and the cavity the sideband locking technique is used [73]: the laser light is modulated, using fiber-coupled EOMs mixing

two frequencies, one being ω_{off} and the second one being a smaller modulation frequency for the Pound-Drever-Hall (PDH) locking [74]. Thus the PDH locking is implemented on the sideband at a frequency ω_{off} from the laser frequency: ω_{off} (and thus the laser frequency) can than be freely changed over a 700 MHz range, while the laser stays locked. This is useful for frequency tuning of the lasers and frequency modulation (e.g. for the red MOT broadband phase). In order to be able to lock two lasers to the same cavity, two different PHD modulation frequencies are used.

The system is rather compact ($60 \times 45 \times 12$ cm^3, including the box with the EOM, see Figure 3.7b) and it has proven to be robust and reliable for transportation. When the clock was moved from Birmingham to PTB in June 2015, even though during transportation neither the ion pump or the temperature control were active, the system was operational less than one day after arrival and the 689 nm cavity frequency (being the most critical one, since we have to address the $^1S_0$-$^3P_1$ transition which is only 7 kHz wide) was shifted only by few hundreds kHz.

3.4 Clock laser reference cavity

The clock laser needs to be stabilized to an ultrastable cavity, which can provide the linewidth and short term (i.e. few hundreds ms to few seconds) stability necessary for the atoms interrogation. The cavity originally used in the SOC2 apparatus is the one described in [75] (Figure 3.8). This is a vertically oriented ULE made cavity, by Syrte (Paris), with fused silica mirror substrates. The length of the cavity is 10 cm. The vacuum system is made of three golden coated aluminum shields. The temperature of the second shield is actively stabilized. This system was designed in such a way that no additional thermal insulation is required. The mass and volume of the cavity are 9 kg and 5 l, respectively. The best instability achieved with this cavity was below 1×10^{-15} for integration times between 200 ms and 1 s [75].

This cavity was integrated with the clock in 2015 after transportation to PTB, and the same year the clock transition was observed for the first time. The smaller transition linewidth observed with this cavity is 32 Hz (Figure 2.10), limited by the cavity instability due to problem with the vacuum system. For this reason the cavity was later sent back to Syrte for an upgrade.

Consequently, as backup solution, the laser was pre-stabilized to a 10 cm horizontal cavity available at PTB [76], whose stability is at the level of 2×10^{-15} at 1 s, and than phase locked to the PTB Sr system clock laser, which is stabilized to a 48 cm long cavity, with an instability below 1×10^{-16} level for averaging times between 1 and 1000 s [77]. For the stabilization, we generate an heterodyne beat between the two lasers (Figure 3.9): this is fed into a phase frequency comparator, which compares the phase of the beat note with the one of a reference

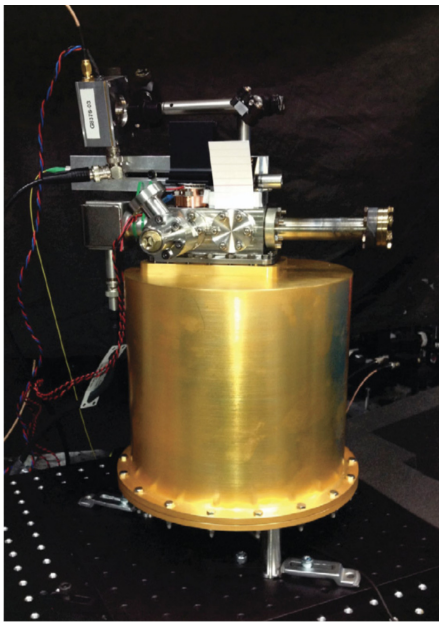

Figure 3.8: SOC2 clock laser reference cavity [75].

RF signal generated by a reference DDS. An error signal is produced, which is used to steer the phase of the wave feeding the reference AOM for the stabilization to the 10 cm cavity. The same AOM is used for the locking to the atomic transition.

The PTB system clock laser can be further stabilized to a cryogenic silicon cavity [78]: this is done using the transfer lock scheme, using an optical frequency comb as transfer oscillator [79] (Figure 3.9). The virtual beat between the two lasers generated by the comb is used for the stabilization, which is achieved by steering the phase of the signal sent to the reference AOM used for the locking to the 48 cm cavity. As it will be shown in Section 4.2, the stabilization to the Si cavity provides exceptionally long clock transition interrogation coherence time.

3.5 Compact vacuum system

The vacuum system (Figure 3.10) was designed and assembled at the University of Birmingham. The main goal of the design was to realize a compact and robust system, with low power consumption, but without compromising the clock performances. The total volume is 143 l and the mass is 50 kg, including breadboard.

In Figure 3.11 is shown the design of the vacuum system. The main components of the system are the high efficiency atomic oven (Section 3.6), the permanent magnet Zeeman slower (Section 3.7) and the compact vacuum chamber and coil assemblies (Section 3.8). Recently, a

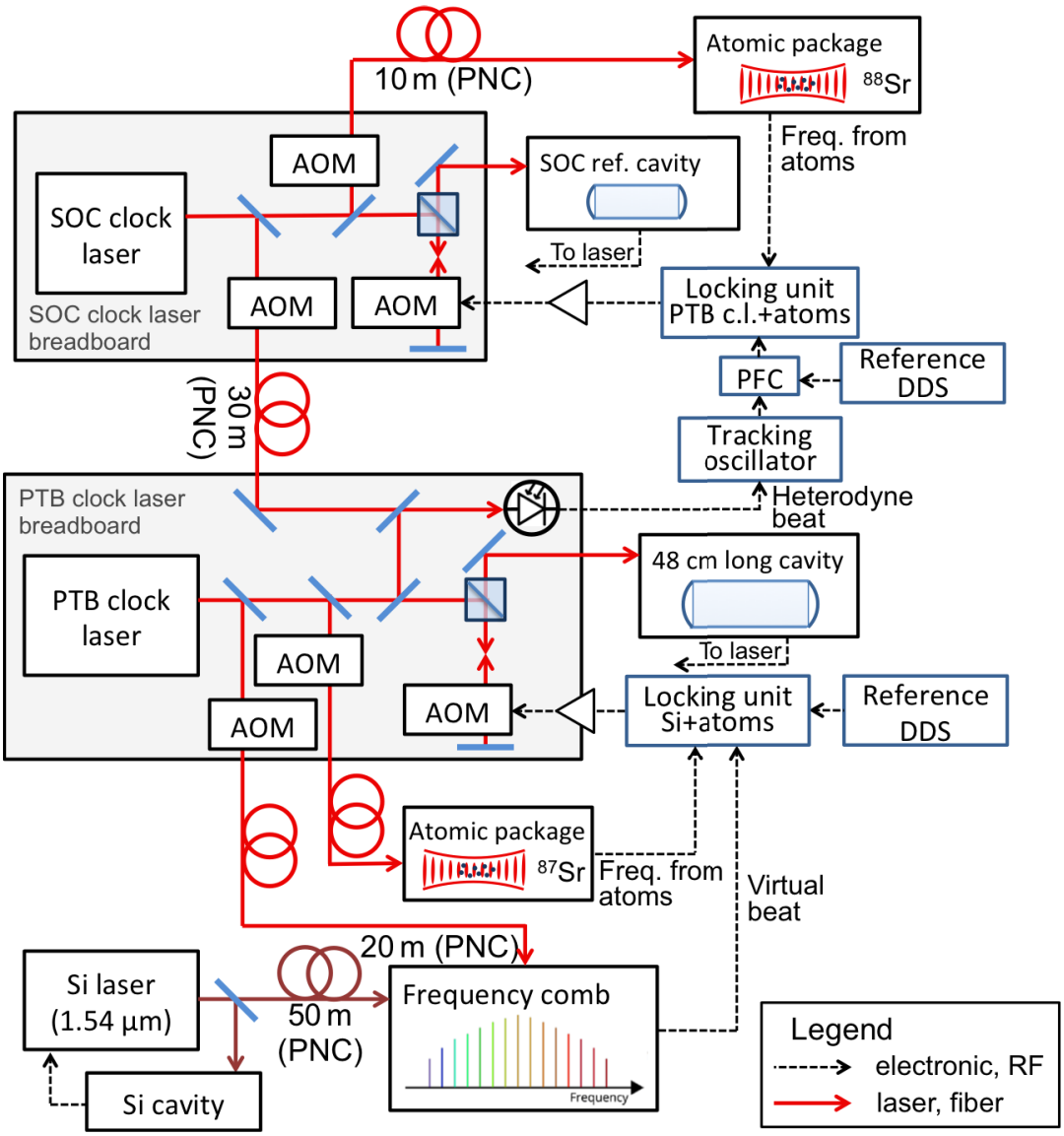

Figure 3.9: Schematic of the optical and electronics setup for the stabilization of the SOC clock laser to the atoms and to the PTB system clock laser, and of the latter to the ^{87}Sr atoms and to the cryogenic Si cavity. PNC: Phase-Noise-Cancelled fiber. AOM: acousto-optic modulator. PFC: phase frequency comparator. DDS: direct digital synthesizer.

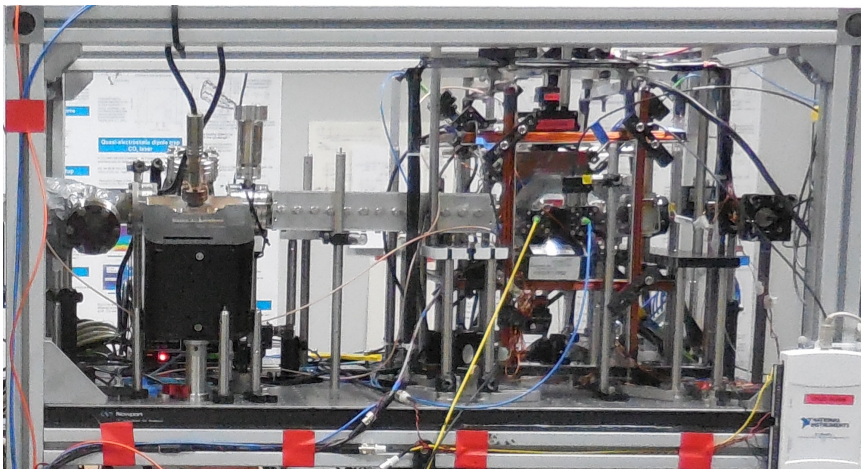

Figure 3.10: Vacuum system. Volume 143 l; mass: 50 kg.

temperature control system was implemented for the main vacuum chamber (Section 3.10), including heat pipes and an heat sink on the top of the rack for dissipating the heat. Two vacuum pumps are implemented: a 25 l ion pump close to the oven and an ion getter pump (NexTorr D100-5 from SAES) on the vacuum chamber side. The latter is a rather novel solution: even though it is quite compact (volume 0.5 l, mass 2.2 kg), it allows, thanks to the presence of the getter element, for relatively high pumping speed (e.g. 100 l/s for H_2 and 40 l/s for N_2).

In between the oven region and the main vacuum chamber, just before the slower tube, there is a 2.5 mm pinhole, acting as differential pumping stage. The expected pressure ratio across the pinhole is about 100. Important updates were the implementation of the new ion getter pump (in replacement of a small 2 l ion pump) and of the differential pumping stage, since they allowed to improve the vacuum level in the main vacuum chamber by almost one order of magnitude, (down to low 10^{-10} mbar level during clock operation): as consequence, the lifetime of the atoms into the lattice increased from $\sim$ 500 ms to more than 5 s (Figure 2.8), making possible ultra-long clock transition interrogation times (see Section 4.2).

In Figure 3.12 and 3.13 it is shown a more detailed view of the main vacuum chamber setup. The chamber is not visible, since it is enclosed in between the MOT coil assemblies. The main vacuum system components are described in detail in the next sections.

3.6 Oven and atomic shutter

The oven design is based on the one presented in [80], developed in Firenze for the SOC1 project, with minor modifications [53] (Figure 3.14). The strontium (maximum 5 g) is contained in a reservoir ending with a nipple with 25 micro-capillaries, with inner diameter

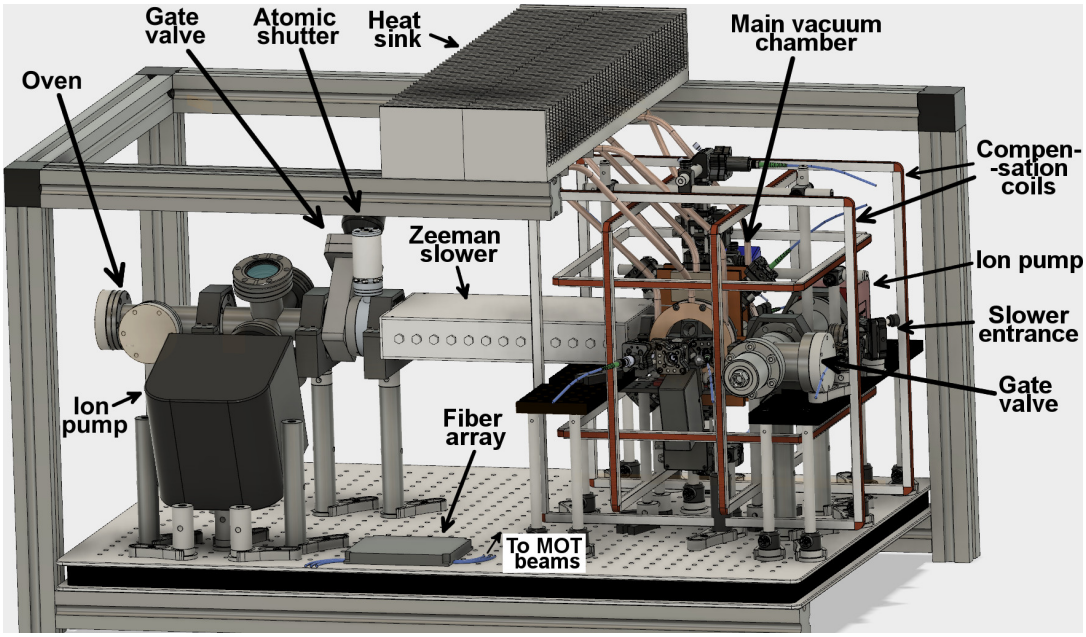

Figure 3.11: Vacuum system design.

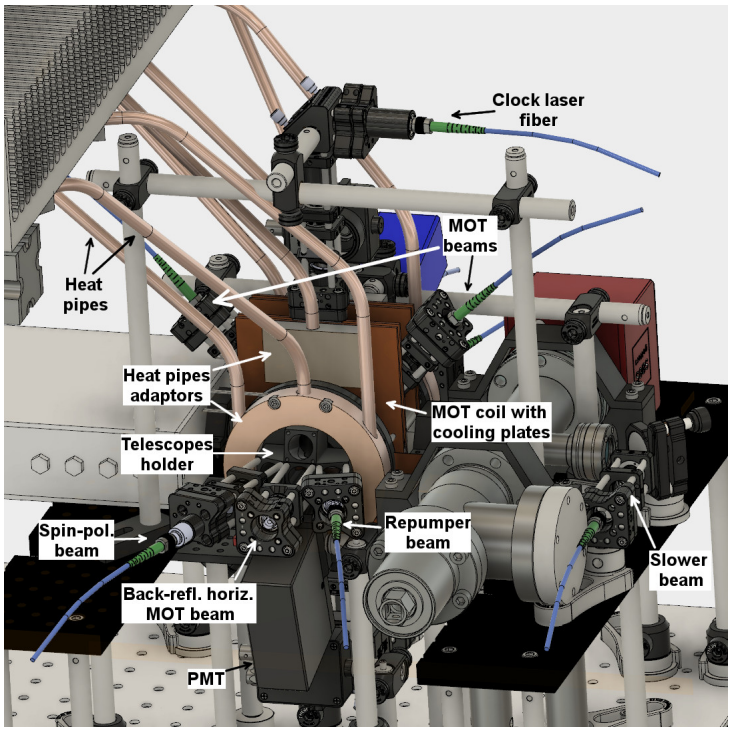

Figure 3.12: Main vacuum chamber setup, front view. The compensation coils are not shown for reason of clarity.

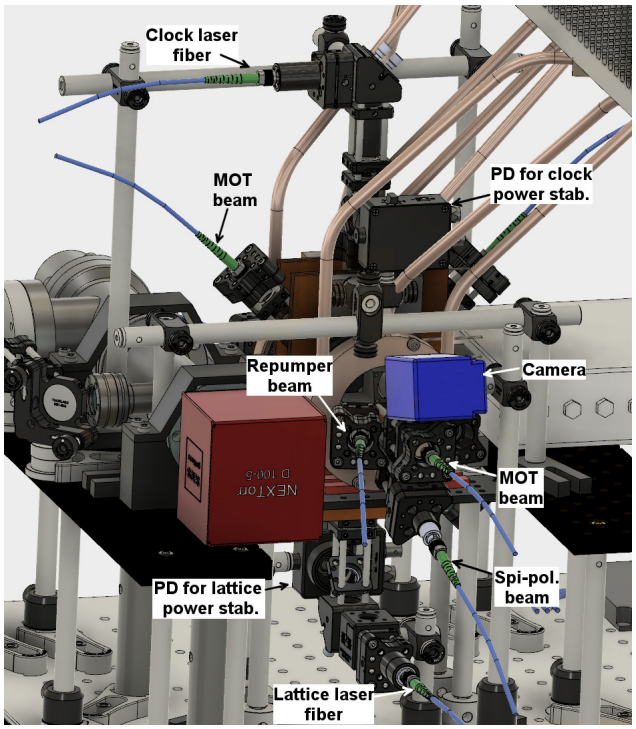

Figure 3.13: Main vacuum chamber setup, back view. The compensation coils are not shown for reason of clarity.

200 μm. These capillaries are used to collimate the atomic beam: the beam divergency was measured to be ~ 20 mrad [53]. The reservoir is heated by a tantalum wire, housed in an alumina multibore tube: the latter is an electrical insulator, with high thermal conductivity. The atomic flux, in standard clock operation, was measured to be $\sim 7 \times 10^{13}$ atoms s^{-1}. The oven is housed in an aluminum shield, with highly polished inner surface, in order to reflect the BBR, and it is mounted on a CF35 flange using steatite ceramic supports for insulation.

The design is optimized for high efficiency: the necessary atomic flux is obtained by operating the oven at relatively low temperature (between 300 and 400 °C), with a power consumption of only 8 to 10 W. The fact that the oven can be operated at low temperature is also an advantage for the clock operation: in fact the BBR from the oven may produce a rather large shift of the clock transition (see Section 5.1). Furthermore, the heat produced by the oven may introduce large gradients in the vacuum system temperature, which result in a larger uncertainty on the BBR shift evaluation.

In order to further shield the atoms from the BBR coming from the oven, an atomic shutter is implemented: the shutter is open during the first stage MOT, and than is closed during the clock transition interrogation. The atomic shutter also avoid the problem of collisions between the atoms being interrogated and the atoms in the atomic beam, which may produce

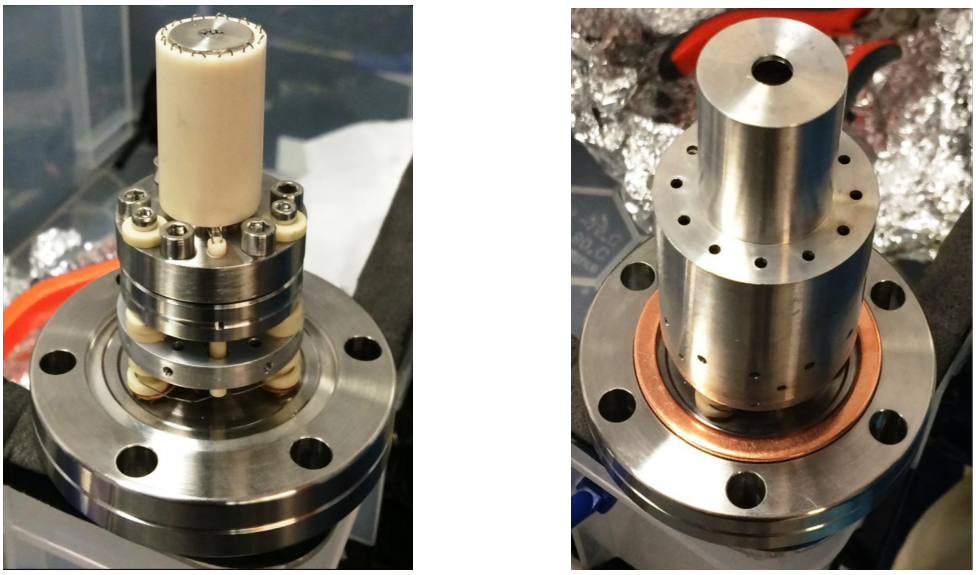

(a) (b)

Figure 3.14: a) Oven without external heat shield. b) Oven with external heat shield. Courtesy L. Smith [53].

an additional collisional shift (see Section 5.7.2). A commercial flag shutter (CF35 Pneumatic Viewport Shutter from Kurt J. Lesker) is used. The shutter is connected via a feedthrough to an external actuator which is operated using a servo motor (model SB2272MG from Savöx). The switching from open to close position takes about 200 ms. The motor is not fixed to the vacuum system but, via proper supports, directly to the optical breadboard: this is done to reduce the vibrations of the main chamber optical system, which may produce Doppler shift of the clock transition frequency.

3.7 Zeeman slower

In the system a permanent magnet Zeeman slower is implemented: this allows for no power consumption, which means also no heat introduced near the main vacuum chamber, compared with more standard tapered solenoid slowers, which require high current. The slower was designed by NPL [81] as part of the SOC2 project (Figure 3.15) and it consists of a 2D array of neodymium permanent magnets. A different number of magnets are stacked together at different positions along the slower, depending on the needed field strength. In addition the field strength at the center of the vacuum system tube (i.e. at the atomic beam position) can be finely adjusted by means of threaded screws on which the magnets are mounted. The array is mounted in an aluminum frame; the plate towards the main vacuum chamber is made by iron

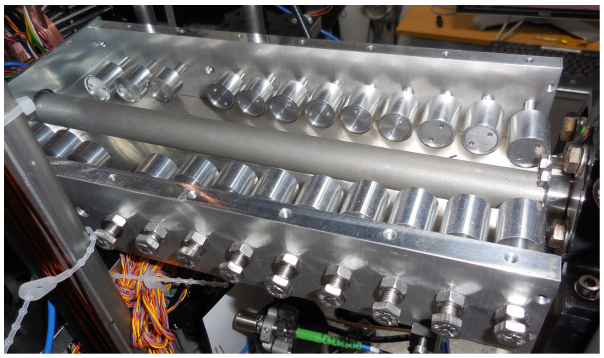

Figure 3.15: Photo of the Zeeman slower from NPL. The size is $276 \times 140 \times 50$ mm.

in order to shield the atoms from the residual magnetic field.

As shown in [81], the magnets position was tuned based on simulation, and than tested on the NPL Sr clock before implementation on the SOC breadboard. No further optimization was necessary. Experimentally, the slowing efficiency can be optimized by changing the slower beam parameters (intensity and frequency).

3.8 Main vacuum chamber and MOT coils system

The vacuum chamber design is presented in detail in [53]: a photo of the chamber is shown in Figure 3.16. The idea was to reduce as much as possible the dimensions of the chamber, without degradation of the clock performance. The advantage of a vacuum chamber with small size is also the fact that the MOT coils can be really compact, thus the power consumption (and therefore the heat produced) is rather small. The main design constraint, for the chamber miniaturization, is the needed optical access for the MOT beams, since a minimum diameter of ~ 10 mm is necessary in order to obtain a large enough trapping region and thus a reasonable trapping efficiency.

The final external size of the chamber is 51 mm (diameter)$\times$22 mm (thickness). Including the tubes for the connection to the rest of the vacuum system, the total length is 130 mm. It presents six small lateral windows (diameter 10 mm) and two large windows on the horizontal plane (diameter 40 mm): the windows material is BK7. The chamber is made by titanium and the windows are sealed with indium, without need for flanges (this further reduce the external size of the chamber). Titanium was chosen since it is lightweight and due to its non-magnetic properties. Furthermore the thermal expansion coefficient of titanium and BK7 are similar: this helps to preserve the vacuum level in presence of large temperature changes (e.g. during baking).

The chamber presents four threaded holes on the two sides for mounting the MOT coils

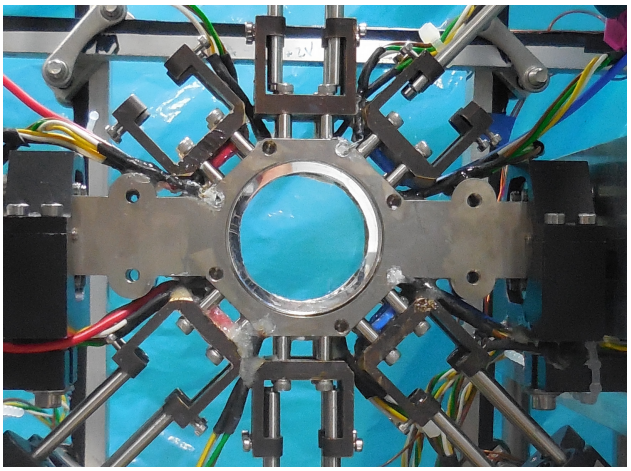

Figure 3.16: Profile view of the vacuum chamber, including telescopes' supports and temperature sensors.

system, on which the horizontal optical cage systems are fixed (see below). The optical cage systems on the vertical plane are fixed directly to the vacuum chamber through custom made adaptors (Figure 3.16). A number of temperature sensors are placed on the external surface of the chamber for evaluation of the BBR shift (see Section 3.10).

Three pairs of electrodes were implemented for DC-Stark shift measurement (see Section 5.6). The electrodes are made of normal electrical wire and placed around the two large windows (z-direction) and four of the small windows (x and y-directions). The field homogeneity was evaluated by simulation and, considering a region within ± 5 mm from the center of the chamber, results to be better than 5% in the z-direction and better than 2% in x and y-directions.

3.9 Optical and monitoring system

As shown in Figure 3.12 and 3.13, all the optics for the beams entering the chamber (a part for the slower beam) are implemented in compact 16 mm cage systems: these are fixed to the main chamber using custom made adaptors. The adaptors for the beams on the vertical plane can be seen in Figure 3.16, while the one for the horizontal beam is shown in Figure 3.12 (named as "telescopes holder"). For the MOT beams, the three outputs of the fiber array (Figure 3.2b), are collimated with a 50 mm lens and the polarization is turned to circular with a quarter waveplate: the three beams are retroreflected with three mirrors. The repumper beams are delivered directly to the main vacuum system via optical fiber and collimated by a 12 mm focal length collimator.

The schematic of the lattice and clock laser beams optical setup is shown in Figure 3.17.

The lattice beam is collimated with a 6.2 mm collimator; after the fiber, a PBS cube is used to ensure that the lattice light is linearly polarized and aligned with the bias magnetic field and with the clock laser polarization. A 75 mm lens is used for focusing the beam at the center of the main chamber (waist size $\sim 40\,\mu$m). On the other side of the vacuum chamber a 75 mm lens collimates the beam and an hot mirror is used for the back-reflection and overlap with the clock laser beam: the hot mirror reflects more than 99% of the lattice laser light and transmits about 90% of the clock laser light. In order to make sure that the back-reflected beam is overlapped with the incoming beam, we couple back the back-reflected light into the lattice fiber, and use a PD in the lattice breadboard for optimizing the coupling efficiency. A beam sampler, before the first 75 mm lens, splits off 10% of the lattice laser light, which is delivered to a PD for intensity stabilization. The same beam sampler is used to reflect part of the clock laser light exiting the vacuum chamber and to deliver it to a PD for the out of loop monitoring of the clock intensity stabilization system (see Section 4.4).

A similar setup is used for the clock laser beam: the beam is collimated with a 4.5 mm collimator and a 2.6:1 telescope is used in order to reduce the beam size. A beam splitter reflects back $\sim$10% of the light for the fiber phase noise cancellation [72] (Section 3.2.5). Than, the beam goes through a PBS cube, with polarization axis aligned with the polarization of the lattice laser. With a beam sampler, 10% of the light is split off for intensity stabilization. Finally, before the hot mirror for the overlap with the lattice laser, we can optionally place a filter (with 10% or 5% transmission, not shown in the scheme): this is done in order to increase the power of the laser light going to the PD for low clock beam intensity to the atoms (since replacing the beam sampler, which is fixed in the cage system, would mean losing the overlap between clock laser and lattice laser beam, see below). The waist size of the clock laser beam is $\sim 105\,\mu$m: this is larger compared with the lattice laser waist in order to ensure an homogeneous intensity of the clock laser beam over the atom sample (i.e. homogeneous Rabi frequency).

For the same reason, it is important that the two beams are properly overlapped and we have to reduce as much as possible the residual misalignment. This is done by placing a pellicle beam splitter before the clock laser entrance window on the top of the chamber (see Figure 3.17) and looking, using the beam profiler (CinCam CMOS-1201-Pico, from Cinogy Technologies, pixel size $2.2 \times 2.2\ \mu$m), to the beam reflected by the upper surface: this allows to image both the clock laser beam and the backreflected lattice laser beam, as they appear at the waist. The pellicle beam splitter is chosen in order to minimize the displacement of the transmitted lattice beam. In this way, the overlap can be controlled at few μm level, with a residual misalignment between the probe and lattice axes of less than 0.1 mrad.

In order to ensure the mechanical stability of the lattice and clock optical systems, both of

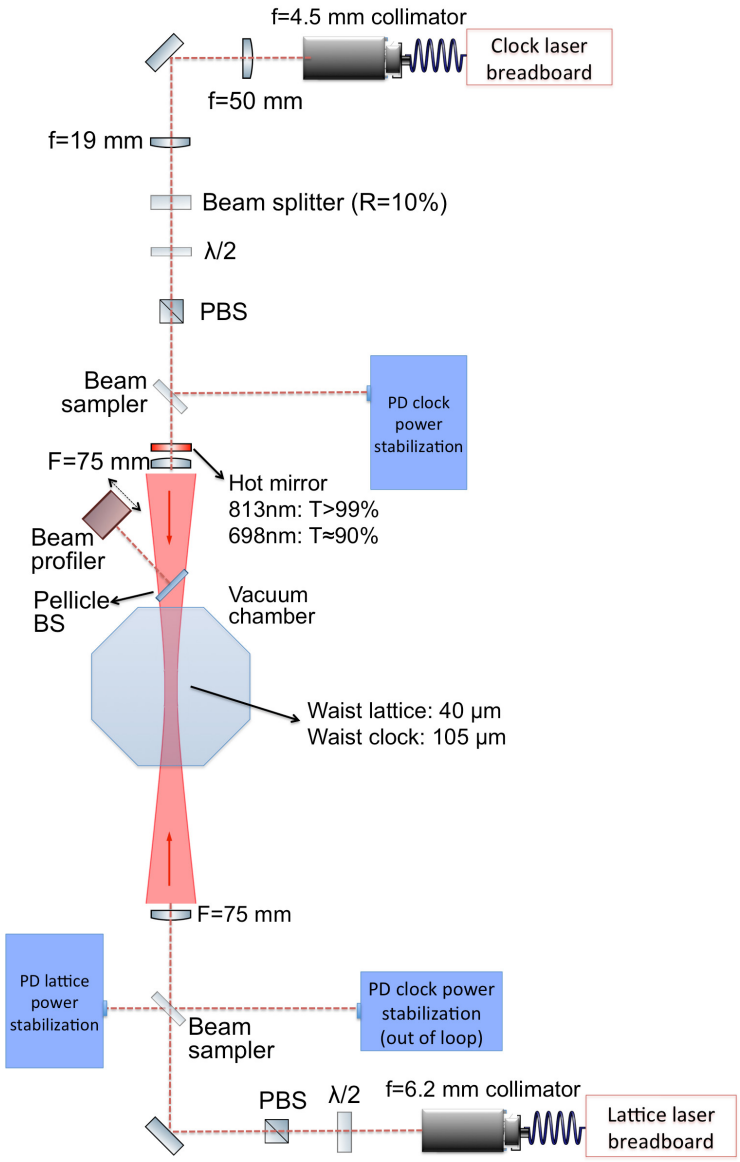

Figure 3.17: Schematic of the lattice and clock beams optical setup.

them are secured not only to the vacuum chamber, through the cage system, but also to the main optical breadboard.

3.10 Temperature monitoring and control system

The accurate knowledge of the temperature and temperature gradients across the main vacuum chamber is necessary in order to evaluate the black-body radiation (BBR) shift (Section 5.1). For this purpose eighteen sensors (thin film PT100, model F3107 from Omega) are used: ten of them are placed on the windows (one on each small window and two on each of the large windows), the others on the chamber itself, in some preexisting holes around the large windows. It is important to have sensors on the windows, since these constitute more than 50% of the internal surface of the chamber. The temperature sensors were calibrated, with a resulting uncertainty of 16 mK (see Appendix B for the details on the calibration). The acquisition device used here is a two channels high-precision thermometer (Anton Paar, MKT50), with 1 mK accuracy.

In order to control the temperature gradients across the main vacuum chamber, a temperature control system was designed and implemented (Appendix C): however, it was found, after the implementation of the temperature sensors, that this was not necessary, since the temperature homogeneity of the chamber was good enough (i.e. the resulting uncertainty on the BBR was not a limiting factor for the clock uncertainty).

3.11 Computer control system

The computer control system is divided in two subsystems. The first one is the LabVIEW program for the Field Programmable Gate Array (FPGA, PCIe 7842R from National Instruments): this is used to run the main clock sequence (Figure 2.3), via analog and digital output channels. In particular it controls the shutters switching, the AOMs power and switching, the current in the MOT and compensation coils and the set point of the intensity stabilization systems. The LabVIEW code was provided by the Institut für Quantenoptik at Leibniz Universität Hannover, and minor modifications were necessary.

The second program is the one for the control of the clock operations. The program is written in Python and includes a GUI (see Figure 3.18). This is completely independent of the LabVIEW program, a part that the acquisition of the PMT signal is triggered (via the DAQ board), by a TTL signal from the FPGA . The main functions of the program are:

1. acquisition of the PMT signal (via a DAQ board) and evaluation of the number of atoms

and excitation probability;

2. scan of the clock transition: this is done by changing the frequency of the offset AOM in the clock laser breadboard for the locking to the 10 cm reference cavity (see Section 3.2.5);
3. locking to the clock transition (Section 4.6.1);
4. Rabi flopping;
5. clock beam power stabilization (slow stabilization, see Section 4.4);
6. bias field current stabilization (Section 4.3);
7. number of atoms stabilization (Section 5.4);
8. 707 nm repumper frequency stabilization (Section 3.2.2).

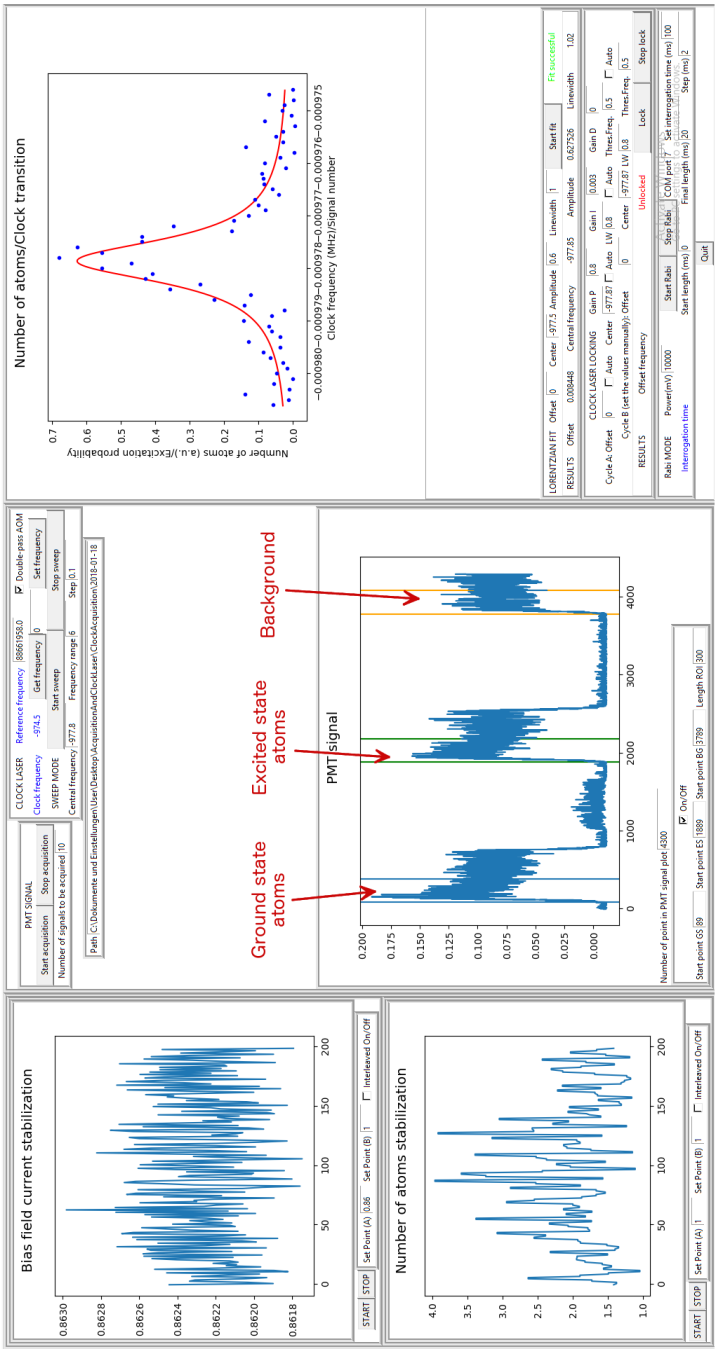

Figure 3.18: GUI of the Python program for the control of the clock operation. In the center is shown the fluorescence signal from the atoms (PMT signal) with indicated the ground (GS) and excited state (ES) atoms detection signals, as well as the background detection signal (which is subtracted from the two previous signals). In between the GS and ES atoms detection, the atoms in the $^3P_0$ and $^3P_2$ state are repumped to the ground state (see Figure 2.3). The number of atoms and bias field current stabilization (plots on the left side) were not running at the time when the screenshot was taken.

Chapter 4

An ultrastable bosonic clock

4.1 Laser frequency noise and Dick effect

As shown in Figure 2.3, the clock operation consists of a preparation phase (atoms cooling and loading into the lattice), an interrogation phase and a detection phase (during which the excitation probability is measured): we "acquire" information on the laser frequency noise only during the interrogation phase, and this information is used in order to steer the clock laser frequency for the following interrogation cycle. This non continuous interrogation of the clock transition gives rise to the Dick effect [82], usually being the main limiting factor for optical lattice clocks instability. In order to reduce the Dick effect it is necessary to increase the Duty cycle: this can be obtained with a longer interrogation time, for which a laser with long enough coherence time is needed, using multi-Ramsey spectroscopy [83], or with an interleaved interrogation of two atom ensembles [24] (i.e. running two clocks sharing the same clock laser).

As described in Section 3.4, in our work we lock the clock laser to the PTB system clock laser, which is stabilized to a 48 cm long cavity [77] (see Section 3.4): in this configuration, we have demonstrated atoms-light coherence times up to 1 s (Figure 4.1). Optionally, the PTB clock laser can be further stabilize to a cryogenic silicon resonator, operated at 124 K [78]: the linewidth of the laser is 10 mHz and the expected usable coherence time for Rabi interrogation is more than 50 s.

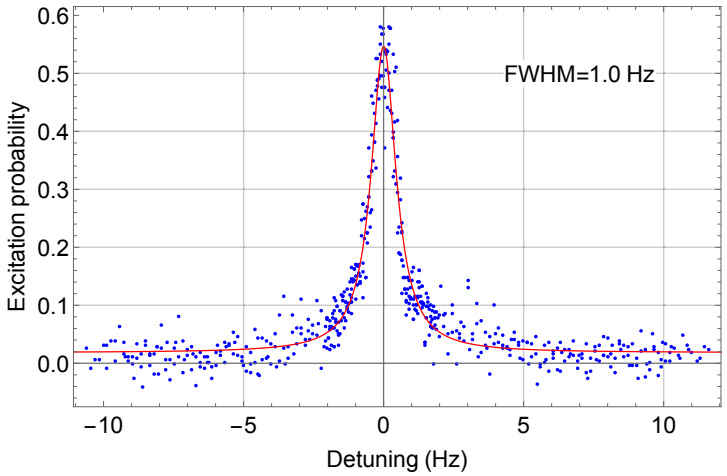

Figure 4.1: Clock transition obtained by phase-locking the clock laser to the PTB Sr system clock laser stabilized on the 48 cm cavity. The interrogation time is $T_\pi = 1$ s.

4.2 Ultra-long coherence times and advantages for magnetically induced spectroscopy

As introduced in Section 2.4.1, the clock laser light induces an AC Stark shift of the clock transition that, for ^{88}Sr, is given by $\Delta\nu_L = kI$, with $k = -18$ mHz/(mW/cm^2), while the finite magnetic field leads to a 2nd-order Zeeman shift $\Delta\nu_B = \beta\,|\mathbf{B}|^2$, where $\beta = -23.8(3)$ MHz/T^2. Therefore, working with bosons, the possibility to interrogate the atoms with longer coherence time is not only an advantage in terms of instability, but also for the clock accuracy: in fact, given the expression for the Rabi frequency $\Omega_R = \alpha\sqrt{I}\,|\mathbf{B}| = 1/2T_\pi$, it is clear that, to longer interrogation times T_π, corresponds smaller I and B, leading to small probe light and 2nd-order Zeeman shift ($\Delta\nu_L$ and $\Delta\nu_B$). With the clock laser being stabilized to the Si cavity, we investigated interrogation times T_π up to 8 s. The longest for which we observed Fourier-limited clock transition linewidths ($\Gamma_{Fourier} = 0.8/T_\pi$ [55]) was $T_\pi = 4$ s: therefore, this was chosen as operational value for all the measurements. For longer interrogation times we assume to be limited by residual collisional effects (see Section 5.4). This implies a Rabi frequency $\Omega_R/2\pi = 0.125$ Hz. The values of I and B are chosen such that both the induced shifts (i.e. their instability) can be controlled at a similar level (see Section 4.3 and 4.4): we chose $I \simeq 28$ mW/cm^2 and $B \simeq 0.21$ mT, leading to shifts $\Delta\nu_L = -0.50$ Hz and $\Delta\nu_B = -1.03$ Hz (from Equations 2.14 and 2.15). These shifts (mainly $\Delta\nu_B$) are much smaller compared with previous works, allowing a better control (i.e. in terms of stability) and more accurate evaluation. Figure 4.2 shows a clock transition taken under the abovementioned conditions, obtained as single scan (i.e. no averaging) with a total scan time of 165 s. This represents one of the

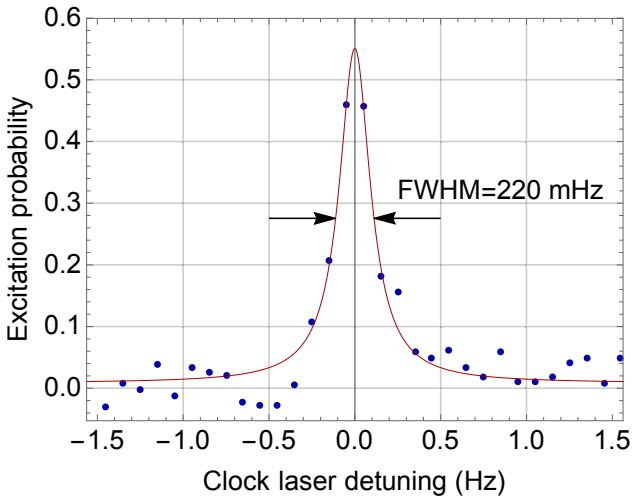

Figure 4.2: Typical ^{88}Sr clock transition line, acquired with the clock laser stabilized to the cryogenic silicon cavity. Rabi frequency $\Omega_R/2\pi \simeq 0.13$ Hz (4.0 s interrogation time), bias field ~ 0.21 mT, clock laser intensity ~ 28 mW/cm^2. The red line represents a lorentzian fit with 220 mHz FWHM linewidth.

smallest optical atomic linewidth ever observed.

Even though $\Delta\nu_L$ and $\Delta\nu_B$ are rather small (10^{-15} relative level), in order to achieve sub-10^{-17} instability and inaccuracy, it was necessary to implement a stabilization system both for the clock laser beam intensity and for the current in the coils used for generating the bias magnetic field. These stabilization systems will be described in the next sections.

4.3 Control of the 2nd-order Zeeman shift

4.3.1 Bias field current stabilization

For producing the bias field necessary for the magnetically induced spectroscopy we use the MOT coils: this allows to generate a relative strong magnetic field with small currents, allowing for a more accurate stabilization. In order to switch from anti-Helmholtz configuration (MOT phase) to Helmholtz configuration (interrogation phase) a system of current switches is implemented (Figure 4.3): it consists of two 60 A MOSFET switches (from Semikron, model SKM111AR) S1 and S2, and five 20 A MOSFET switches (from Crydom, model D1D20) S3 to S7. This switch system allows also to invert the bias magnetic field, in Helmholtz configuration, for a more accurate determination of the 2nd-order Zeeman shift. In particular: during MOT phase only switches S1, S2 and S3 are closed; for a "positive" bias field switches S1, S4 and S5 are closed; for a "negative" bias field switches S6, S7, and S3 are closed.

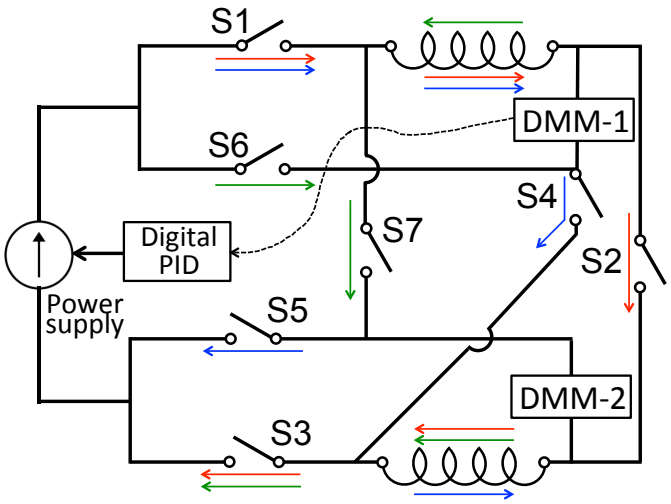

Figure 4.3: Scheme of the circuit used for the MOT coils. Red, blue and green arrows indicates the current flow for anti-Helmholtz configuration (MOT phase), Helmholtz "positive" field and Helmholtz "negative" field, respectively.

Two DMMs are used (Agilent 34401A and Keysight 34461A, with same specification in terms of accuracy): one is used for the stabilization (in-loop) and the second one for monitoring (out-of loop). The DMM are placed in such a way that the high current during MOT phase doesn't pass through them, and they are in two different sections of the circuit with respect to the coils: in this way we can continuously check that the current follows the right path, and that the switches are working as expected.

The commercial power supply (Dana, model "DAB 20-25", selected for providing an external analog control input) that drives the MOT coils, was found to have sufficient short-term stability, but exhibits oscillations on the timescale of a few minutes and at the level of 1%. Thus, it was only necessary to implement a slow stabilization. The DMMs were set in maximum accuracy mode, implying a slow acquisition rate (30 s^{-1}). The average of the digital readings of each interrogation cycle is fed into a digital PID (implemented in Python) acting on the external control voltage of the power supply.

4.3.2 Stabilization results

The resulting in-loop instability of the current is shown in Figure 4.4, together with the not stabilized case and the out of loop instability (as measured by the second DMM): this gives an independent measurement of the long term performance of the stabilization system.

The expected contribution of the current instability (left axis) to the clock frequency instability (right axis) can be inferred based on the measurement of the 2^{nd}-order Zeeman shift

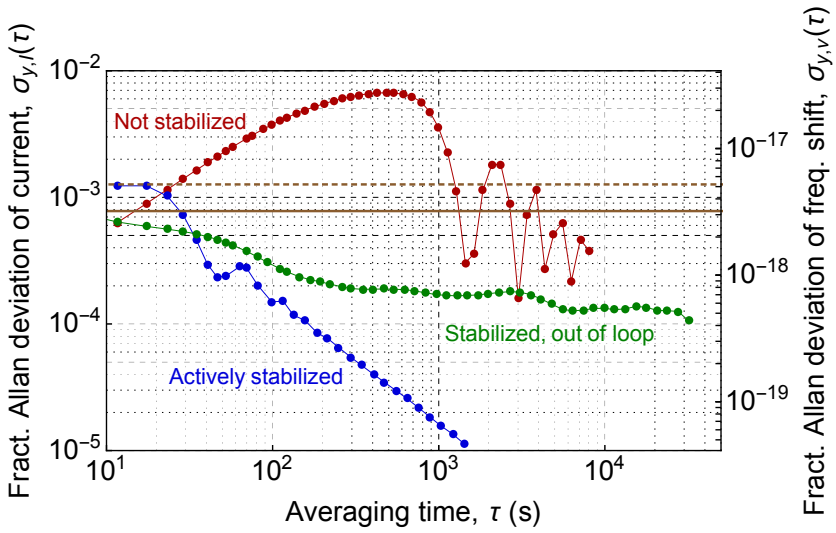

Figure 4.4: Instabilities and inaccuracies related to the bias field applied during clock transition spectroscopy, at a mean current of 215 mA, corresponding to a Rabi frequency $\Omega_R/2\pi \simeq 0.13$ Hz. Brown solid line: inaccuracy specification of the DMM on the 24 h time scale; brown dashed line: same, on 90 days time scale.

(Section 5.2). The expected frequency instability drops below 1×10^{-18} for $\tau \geq 70$ s. However, the actual stability is expected to be limited by the long-term drift of the DMM. At a bias current of 215 mA, corresponding to $\Omega_R/2\pi \simeq 0.13$ Hz, the expected drift is 0.17 mA on the 24 h time scale and 0.27 mA on the 90 days time scale. From the evaluation of the 2nd-order Zeeman shift, the corresponding frequency shifts are 1.3 mHz (3.1×10^{-18}) and 2.2 mHz (5.1×10^{-18}), respectively (brown solid and dashed horizontal lines in Figure 4.4). For comparison, we estimate the case in which the Rabi frequency is $\Omega_R/2\pi \simeq 0.5$ Hz: this is the typical Rabi frequency when the clock laser is stabilized only to the 48 cm long cavity (and not to the Si cavity). Assuming the same clock laser intensity as the case above, the bias current increases to about 0.86 A, where the DMM long-term drift is 0.49 mA at 24 h and 0.79 mA at 90 days, corresponding to 15.3 mHz (3.56×10^{-17}) and 24.6 mHz (5.7×10^{-17}), respectively. This is approximately one order of magnitude higher compared with the case above.

However, the out of loop measurement (Figure 4.4, green points) suggests a drift much smaller than expected and at the level of 30 μA (or 5×10^{-19} as relative frequency shift) on a daily timescale. Furthermore, the difference in the reading between the two DMMs was always below 100 μA: this indicates proper operation of the switches system.

The bias field is "switched on" as soon as the atoms are transferred into the lattice, while the interrogation starts 70 ms later, when the clock laser beam is turned on. It was verified that this delay is sufficient to ensure that the current is stable when the interrogation begins.

A drift of the geometry of the coils, e.g. due to temperature variations, will also contribute

to a drift of the Zeeman shift. Modelling the coils system as a torus, and assuming temperature fluctuations of 5 K, it was evaluated that this would result in a difference of less than 1 nT, five orders of magnitude smaller compared with the applied field.

An additional effect, whose influence is difficult to evaluate, is the mechanical stress to which the coils are subjected due to the fast switching between MOT configuration, when they experience an attractive force, and bias field configuration, when repulsion occurs. However we assume this effect to be negligible, mainly for the long term stability.

4.4 Control of the probe light shift

4.4.1 Probe beam wave power stabilization

The scheme of the clock laser wave power stabilization is shown in Figure 4.5. The polarization of the light, delivered to the atomic package from the clock laser breadboard, through an optical fiber, is linearized using a PBS. A beam sampler (not shown) splits off $\simeq$10% of the clock laser light before being overlapped with the lattice laser and delivers it to a photodetector (PD; from Thorlabs, model PDA36A); a T=5% neutral density (ND) filter is placed after the beam sampler, but before the hot mirror used for the overlap with the lattice laser beam, in order to increase the power of the laser light going to the PD for low clock beam intensity to the atoms (e.g. $I_{\mathrm{CL},0} = 28$ mW/cm^2 corresponds to about 4 μW to the atoms)[1]. The signal from the PD is split and sent to the analog stabilization module (fast stabilization) and to a DAQ board (NI USB-6210) for the implementation of a slow digital PID (Python): this controls the set point of the analog power stabilization via a dedicated analog input. In addition, the analog module has a TTL input, used to activate the stabilization and reset the integrator when the beam is switched off. The output of the analog stabilization controls the amplifier for the AOM in the clock laser optical breadboard.

In order to ensure a fast settling time when the beam is switched on, the "sample and hold" technique is implemented. A rectangular signal, synchronized with the clock laser pulse, is added to the output of the analog stabilization module: the signal has the same amplitude as the control voltage sent to the RF-amplifier in the last 100 ms of the previous cycle. In this way the analog power stabilization module is always working around zero volts.

The limitation to the ultimate probe light shift stability may depend on a number of factors: (1) the PD noise (e.g. instability of the PD reading due to thermal drift or shot noise); (2) the noise in the transmission to and acquisition of the signal by the DAQ board used for the slow

[1] Instead of using the filter, one could simply replace the beam sampler, using one with higher reflectivity. However, the beam sampler is difficult to be replaced since it is fixed in the cage system.

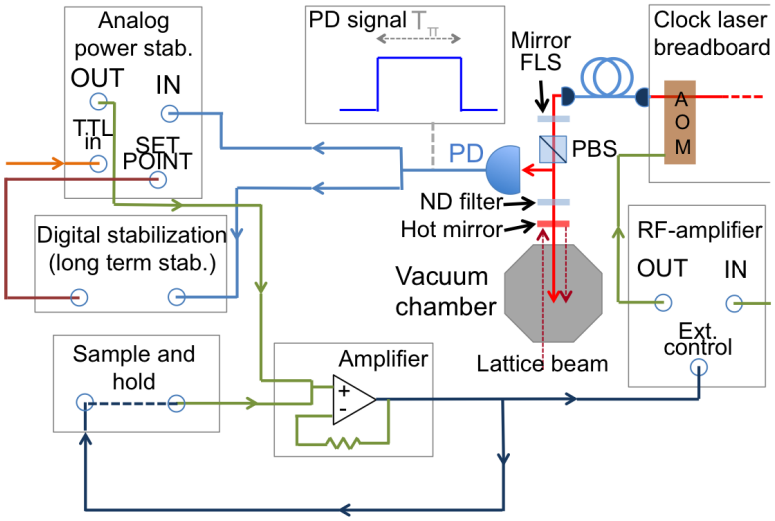

Figure 4.5: Scheme of the clock power stabilization system. A detailed description is given in the text. FLS: fiber length stabilization. PBS: polarization beam splitter.

stabilization; (3) the stability of the transmissivity of the optics after the beam sampler (ND filter, hot mirror for the overlap with the lattice laser, chamber window); (4) the pointing stability of the clock laser beam compared with the lattice position; (5) the stability of the temporal shape of the clock laser pulse, since it is the clock laser beam switching which 'triggers' the interrogation; (6) etalon effect within the clock laser optical system.

(1), (2) These contributions can be estimated by measuring the instability of the PD signal, acquired by the DAQ board, with the clock beam off. The resulting contribution to the PD signal instability is less than 3×10^{-3} over many days (corresponding to a frequency shift of 2.6×10^{-18}). This value is used as uncertainty on the PD signal. The problem of the PD background signal drift can be avoided in the future, by measuring for every cycle the PD signal when the clock beam is off (e.g. just after the interrogation phase, before the detection) and subtracting the measured value from the PD signal with the beam on.

(3) The stability of the transmissivity of the optics after the beam sampler can be tested by monitoring the clock beam power after the vacuum system, while the clock power stabilization is running. The measurement was performed by measuring the light transmitted by the chamber with a PD (same model as the one used for the stabilization). The PD signal was acquired with a digital multimeter (Keysight 34461A): given the higher accuracy of the DMM compared with the DAQ board used for the stabilization, this allows also to test independently the noise in the PD signal acquisition (point (2)). The results are discussed below.

(4) Measurements acquired over few weeks, demonstrate a displacement in the overlap between the clock laser beam and the lattice laser beam of less than 5 μm. Such a displacement

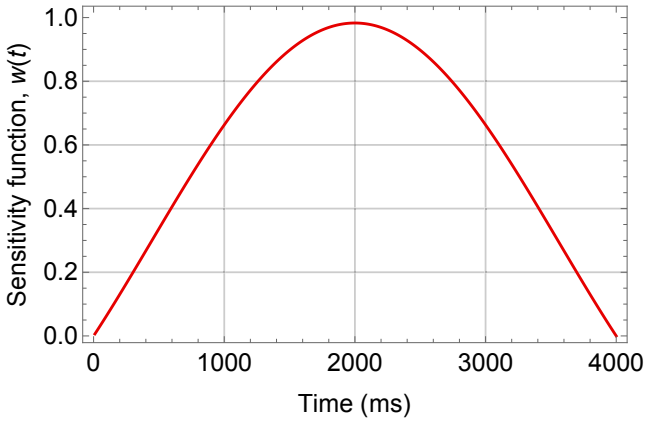

Figure 4.6: Sensitivity function evaluated for an interrogation time $T_\pi = 4$ s, using Equation 11 in [82].

results in a change of the intensity of $\simeq 0.5\%$, corresponding to 2.0 mHz (or 4.5×10^{-18}) shift. It is assumed that, in a shorter time scale of few days (which is the time necessary for the evaluation of the clock uncertainty budget and frequency ratio measurement, see Section 5.9), the contribution due to this effect is reduced at low 10^{-18} level.

(5) Since the bias magnetic field for the spectroscopy is switched on as soon as the atoms are loaded into the lattice (i.e. about 70 ms before the interrogation) and off few tens of ms after the interrogation is finished, it is the clock laser switching that 'triggers' the interrogation. Therefore, the switching time can be of critical importance for the clock instability. In particular, what we are interested in here, is the instability of the integrated power of the clock laser pulse, weighted using the sensitivity function, which describes the temporal dependence of the sensitivity of the measured excitation probability to the clock laser frequency changes during the clock interrogation [23, 82] (Figure 4.6). The sensitivity function is really small at the beginning and end of the interrogation, reaching the maximum (100%) at $T_\pi/2$. For example, using $T_\pi = 4.0$ s, its value is below 1% for the first (and last) 16 ms of the interrogation pulse: since the power stabilization settles (i.e. the maximum deviation is smaller than 1% from the reference value) after less than 1 ms, the settling time is clearly not a problem for the clock instability.

(6) Some etalon effect was observed in the back-reflected signal for the fiber length stabilization (FLS, see Figure 4.5), when the T= 5% filter was not installed: this is due to the fact that about 10% of the clock laser light is reflected back by the hot-mirror used for the overlap with the lattice beam. This can be a problem also for the beam transmitted by the hot mirror and reaching the atoms. However, the presence of the filter strongly attenuates this effect: in fact, it was not observed in the measurement of the light transmitted by the vacuum system (point (3)).

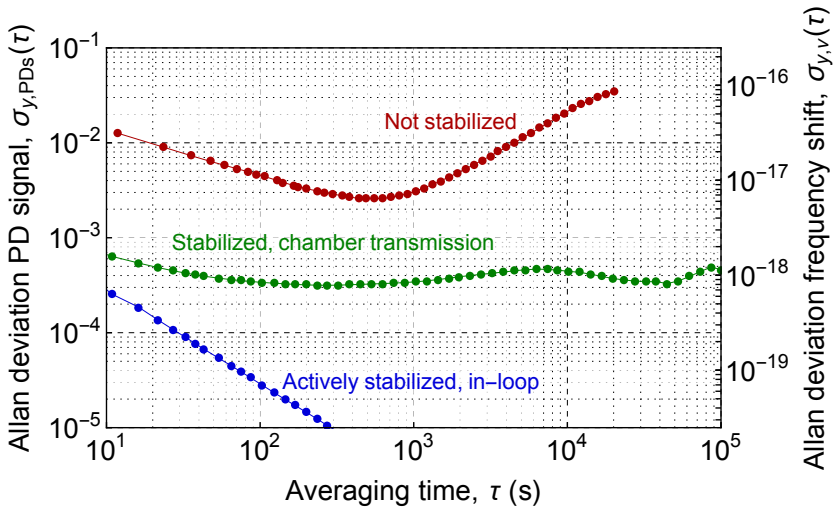

Figure 4.7: Instabilities and inaccuracies related to the clock laser wave power.

4.4.2 Stabilization results

The result of the power stabilization is shown in Figure 4.7. As mentioned above, the PD signal for the chamber transmission (green points) was acquired with a digital multimeter (Keysight 34461A): the resulting instability was found to be less than 5×10^{-4} over few days. The expected contribution to the clock frequency instability is evaluated based on the measurement of the probe light shift (Section 4.4) and, for the out of loop signal, is at 1×10^{-18} level for $10 < \tau < 10^5$ s.

4.5 Control of collisions in 1D optical lattice

As discussed in Section 2.4.2, the interaction between the atoms trapped into the lattice introduces two effects: decoherence and collisional frequency shift of the clock transition [67].

Figure 4.8 shows the effect of collisions on the clock transition line-shape, while the atom number is changed by a factor of ~ 10: with the increase in the number of atoms, also the linewidth increases. In order to investigate the effect of collisions on the atoms-light interaction coherence time, we used Rabi flopping (Figure 4.9): as expected the coherence time it is negatively affected by higher atom density. Furthermore, it was observed that the collisional dependent decoherence effects are more and more critical at lower Rabi frequencies (i.e. for longer interrogation times).

In order to be able to work with sub-Hz Rabi frequencies, it is necessary to find a way to reduce the atoms density into the lattice, which means reducing the number of multiply occupied lattice sites. One simple way would be to operate with a small number of atoms,

as small as a few hundred, i.e. significantly smaller than the number of lattice sites (several hundred). Working with small atom number, the quantum projection noise (QPN), related to the measurement of the excitation probability while probing the clock transition, may become a limiting factor for the clock instability [23]. The quantum projection noise limited instability is given as [84]:

$$\sigma_{\mathrm{QPN}}(\tau) \simeq \frac{\Gamma}{\nu_0}\sqrt{\frac{T_{\mathrm{c}}}{N\tau}} \tag{4.1}$$

where Γ and ν_0 are the clock transition linewidth and frequency, N is the number of atoms, T_{c} is the cycle time and τ is the measurement time. For example, if the clock laser is stabilized to the Si cavity ($T_c \approx 5$ s, $\Gamma = 0.2$ Hz), the QPN limit is below $1 \times 10^{-16}/\sqrt{\tau}$ level, with more than 100 atoms being interrogated: thus, assuming to work with few hundreds atoms into the lattice, this doesn't represent the main limitation to our instability (being at the level of $2-3 \times 10^{-16}/\sqrt{\tau}$, as shown in Section 4.6).

Another problem when operating with low atom number is the low signal to noise (S/N) ratio in the atoms fluorescence signal (PMT signal), which results in a noisier clock transition. This is why, while working with sub-Hz spectroscopy linewidths, it was found that reducing the atom number was not enough to be able to observe transitions with Fourier limited linewidth and a S/N ratio allowing a reliable stabilization.

A way to reduce the atoms occupancy, without reducing too much the total number of atoms, is by loading the atoms into the lattice starting from a slightly warmer red MOT, corresponding to a lower density: this allows to spread the atoms over more lattice sites. This is the approach used in our experiment. In order to observe usable transitions working with $T_\pi = 4$ s interrogation time, a reasonable atoms temperature was found to be between 7 and 10 mK (as measured by sideband spectroscopy). A drawback of this solution is the fact that a large fraction of atoms is lost in the transfer from the red MOT to the lattice. Furthermore, higher atoms temperature may lead to tunneling between the lattice sites, which can cause a shift of the clock transition frequency [85]: however, for temperatures below 10 mK, tunneling is strongly suppressed since the lattice is vertically oriented, and this, due to gravity, results in lifting the energy degeneracy between the lattice sites [85].

Another way of reducing the atoms density is the use of photoassociation [70]: two atoms in the same lattice site are combined in an excited Sr_2 molecule, by interacting with a photon from the photoassociation beam (an additional beam overlapped with the lattice laser beam). The molecules may either decay to ground state molecules in high vibrational states or hot atoms, which cannot stay trapped into the lattice. Photoassociation was demonstrated in our setup and results are discussed in Section 5.4.2.

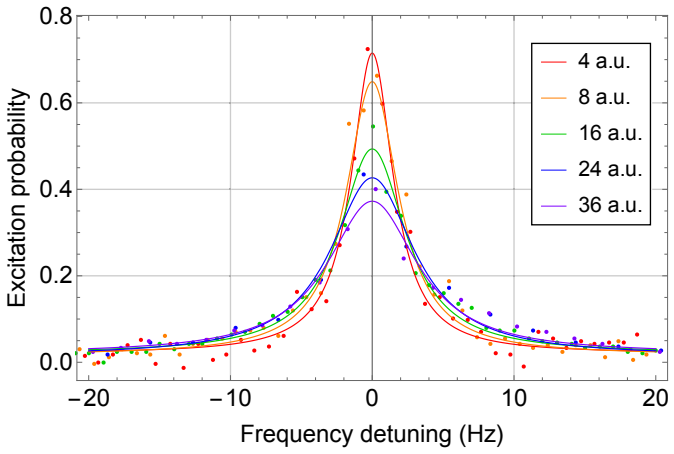

Figure 4.8: Collisional broadening and decoherence of the clock transition.

The presence of density dependent frequency shift of the clock transition may also affect the clock instability: in fact, collisional shift may be between a few tens of mHz and a few Hz [62, 63, 67]. As it is shown in Section 5.4, the shift it was measured to be below 5×10^{-18} level, meaning that, with typical number of atoms fluctuations below 20%, the contribution to the clock instability is below 1×10^{-18} level, and therefore almost negligible.

4.6 Clock instability measurement

4.6.1 Stabilization to the atomic transition

In order to stabilize the clock laser to the atomic transition, the line is probed at the two sides, with detuning about $\pm\Gamma/2$ (being Γ the transition linewidth) from the center. From the difference between the measured excitation probability for the two interrogations (ep_1 and ep_2), and assuming a Lorentzian lineshape, one can evaluate the frequency offset between the clock laser frequency and the transition frequency as [68]:

$$\Delta\nu \simeq \pm\Gamma\frac{ep_2 - ep_1}{2(ep_2 + ep_1)} \tag{4.2}$$

This value is fed into a digital proportional integral (PI) filter in order to evaluate the correction to be applied to the clock laser frequency for the next interrogation.

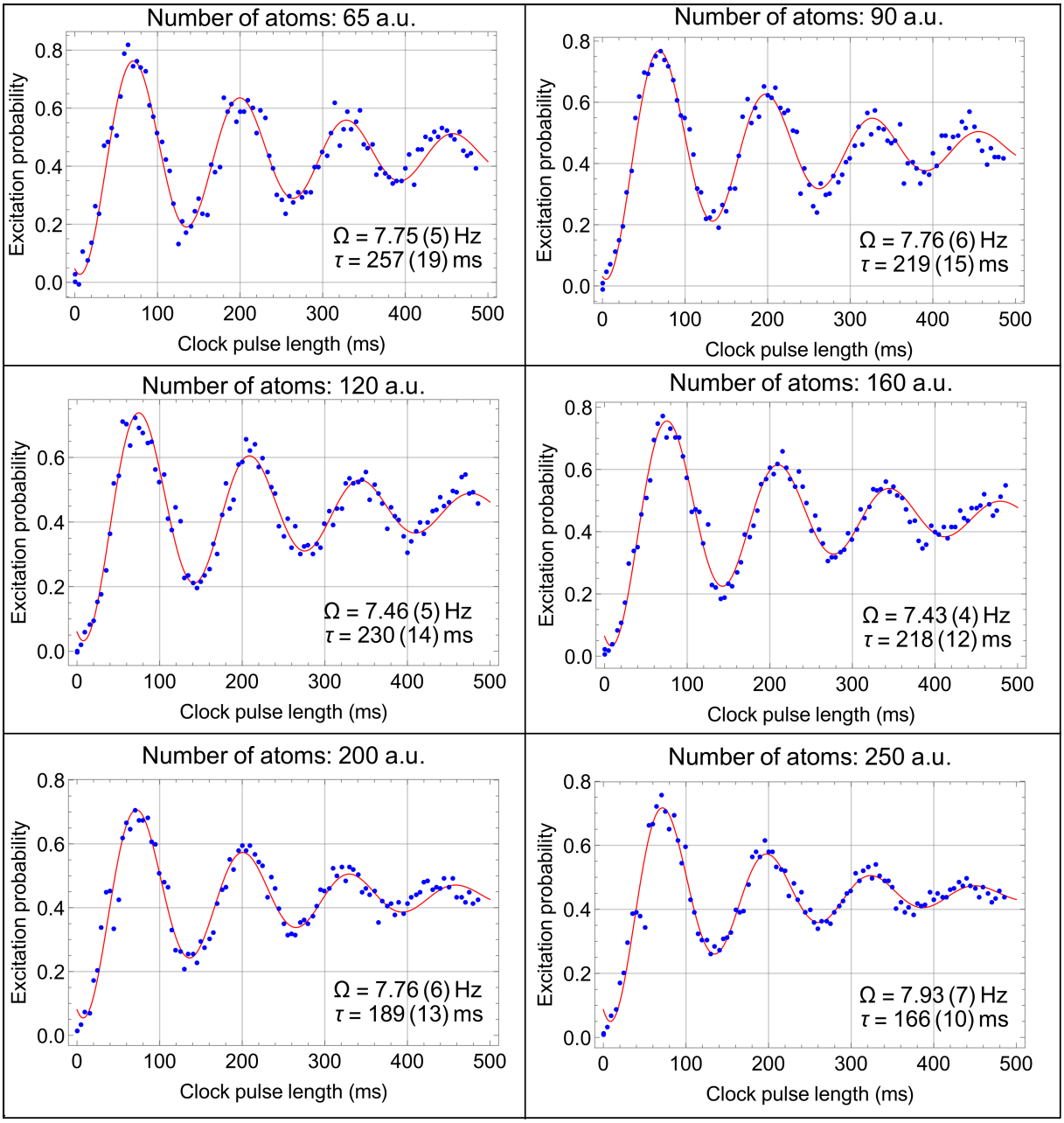

Figure 4.9: Rabi flopping of the excited state probability (ep) at different atom number. The fit function is $\text{ep} = a(1 - cos(2\pi\Omega\Delta t)exp(-\Delta t/\tau))$, where Ω is the Rabi frequency, τ is the decay time and Δt is the clock pulse length. Note: the atom number scale is not the same as the one in Figure 4.8.

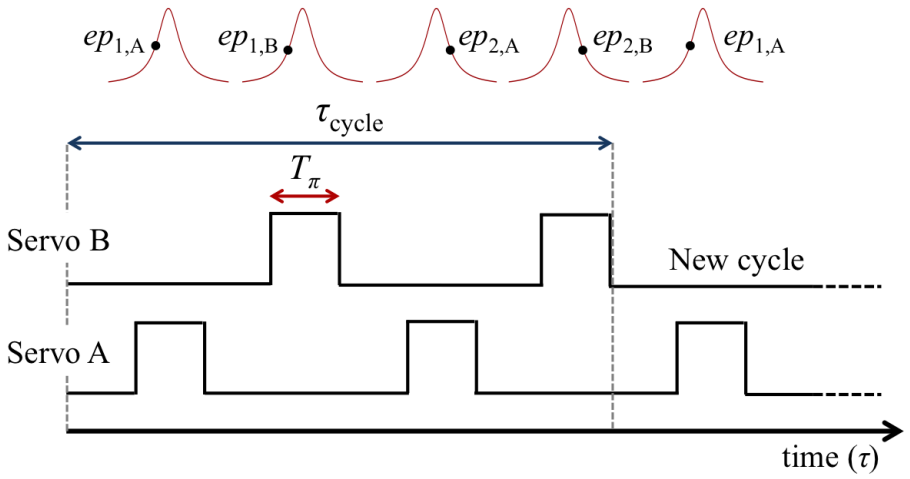

Figure 4.10: Schematic of the interleaved stabilization method. Two independent atomic servos ("Cycle A" and "Cycle B") alternatively probe the clock transition.

4.6.2 Interleaved instability

A first characterization of the clock instability is performed by interleaved measurement. Two stabilization cycles (atomic servos) are implemented, alternatively stabilizing the clock laser to the clock transition (Figure 4.10). The difference between the frequency of the two servos is used for the evaluation of the interleaved instability. This measurement is used to characterize the clock instability as combination of detection noises and clock laser noise [23]. However, it is not useful in order to characterize long term drifts, for example due to changes in the clock laser intensity, bias magnetic field or temperature of the chamber, since these effects are common to both the interleaved cycles.

In Figure 4.11 it is shown an example of Allan deviation[2] plot for interleaved instability measurement: this was acquired when the PTB system clock laser was not locked to the silicon cavity but only stabilized to the 48 cm long cavity [77]. The clock transition interrogation time was 550 ms (1.5 Hz Fourier limited linewidth) and the total cycle time was 2.4 s. The interleaved instability ($4.7 \times 10^{-16}/\sqrt{\tau}$) is about a factor of two larger compared with the single lock instability [23]. The expected Dick limited instability, as evaluated from the power spectral density frequency fluctuations of the silicon cavity and from the cycle parameters [23], is about $1.5 \times 10^{-16}/\sqrt{\tau}$. Thus, the measured instability is about 50% higher, which may

[2]The clock frequency (f) instability is usually expressed in terms of Allan deviation [86]:

$$\sigma_y(\tau) = \left[\frac{1}{2(N-1)} \sum_{n=1}^{N-1} (f_{n+1} - f_n)^2 \right]^{1/2}$$

where N is the number of measurements acquired with averaging time τ. Even though not explicitly stated in the plot, this is expressed as fractional value $\sigma_y(\tau)/\nu_0$, ν_0 being the frequency of the clock transition.

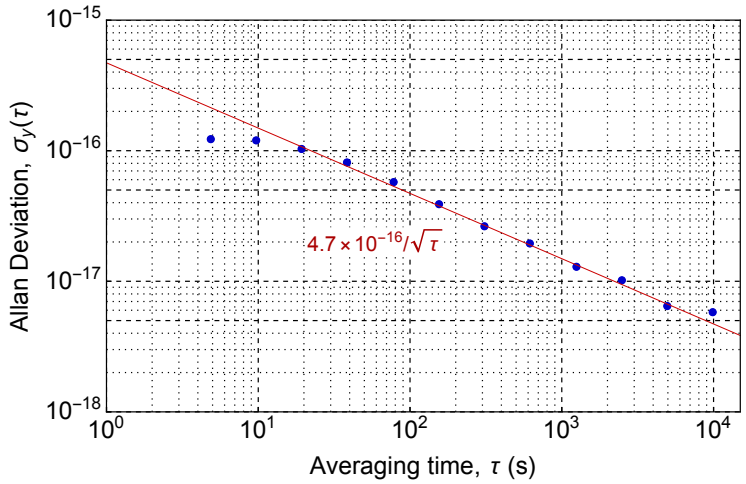

Figure 4.11: Allan deviation of the frequency offset between the two interleaved cycles.

indicate a significant contribution due to detection noises.

The interleaved measurement is used also for the evaluation of the clock transition frequency shifts, as probe and lattice light shift (Sections 5.3 and 5.5), 2^{nd}-order Zeeman shift (Section 5.2) and DC-Stark shift (Section 5.6). In this case the physical quantity which induces the shift (e.g. light intensity, bias magnetic or electric field) is different in the two interleaved cycles and the frequency offset provides the corresponding clock transition shift: the measurement can be repeated with different values of the field and, from the fit of the resulting data, one can deduce the clock transition frequency at zero field. For the uncertainty on the frequency offset we use the Allan deviation, extrapolating its value to the total measurement time, using the fit function.

4.6.3 Clock comparison

The clock instability was than measured against the PTB ^{87}Sr clock. As described in Section 3.4, the SOC transportable clock laser is phase-locked to the PTB clock laser, which is in turn stabilized to the cryogenic silicon cavity [78], for short-term stability, and to the ^{87}Sr clock transition, for the long term stability. Thus, the SOC clock laser is not affected by long term drift, but it includes the corrections of the atomic servo of the PTB Sr clock.

In Figure 4.12 are shown the raw data for the longer measurement that we have acquired: the two clocks were operated continuously for about 1.3×10^5 s. The intervals within the red regions were not used for the evaluation of the Allan deviation (Figure 4.13): in the first interval it was noticed a decrease in the lattice laser intensity (which the intensity stabilization system was not able to compensate), while the next two regions correspond to time intervals during which the stationary system clock laser was not locked.

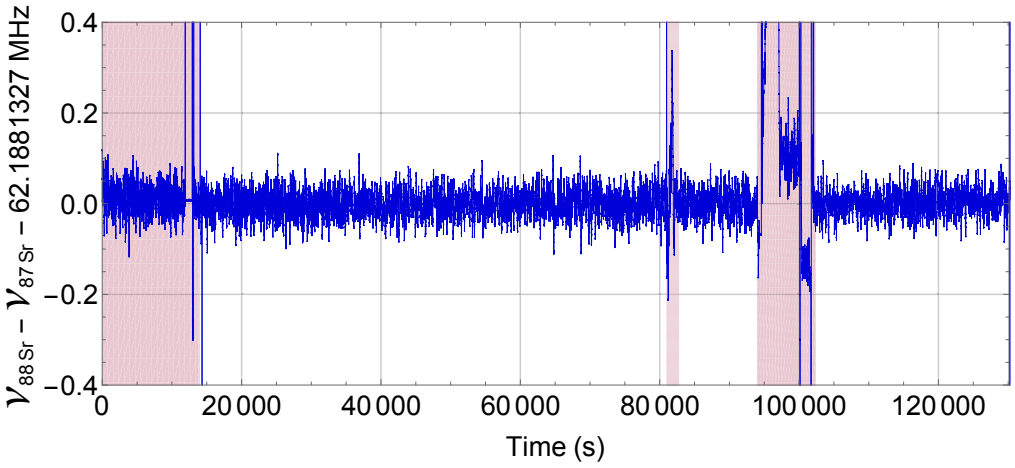

Figure 4.12: Beat note between the SOC clock laser and PTB system clock laser, locked respectively to ^{88}Sr and ^{87}Sr clock transition. The beat note is measured directly by a frequency counter. The intervals within the red regions were not used for the evaluation of the Allan deviation (Figure 4.13): in the first interval it was noticed a decrease in the lattice laser intensity, while the next two regions correspond to time intervals during which the PTB clock laser was not locked. This data represent the raw data, without any correction applied.

The Allan deviation of this measurement is shown in Figure 4.13. The fact that the Allan deviation starts to average down only after $\sim 10^2$ s, compared for example with the interleaved instability (Figure 4.11), where this happens after few tens of seconds, can be explained with the longer stationary clock servo time constant, due to the fact that four interrogations (for the two $m_F = \pm 9/2$ components) are necessary per each stabilization cycle. The combined instability results $i_{comb} = 4.1 \times 10^{-16}/\sqrt{\tau}$, thus the single clock instability, assuming it to be similar for the two clocks, is between 2 and $3 \times 10^{-16}/\sqrt{\tau}$. The instability reaches the 3×10^{-18} level after about 20 000 s averaging. This represents a new record for a bosonic clock. Furthermore, it demonstrates the proper operation of the clock laser power stabilization and bias field current stabilization systems.

A number of measurements were acquired between May 2017 and September 2017 in similar conditions (Figure 4.14): all of them show an instability whose averaging is similar to the one reported in Figure 4.13, with an ultimate instability below 6×10^{-18}. This confirms the reliability of the bosonic clock operation and represents an enabling step towards the next phase of the clock characterization, namely the uncertainty evaluation.

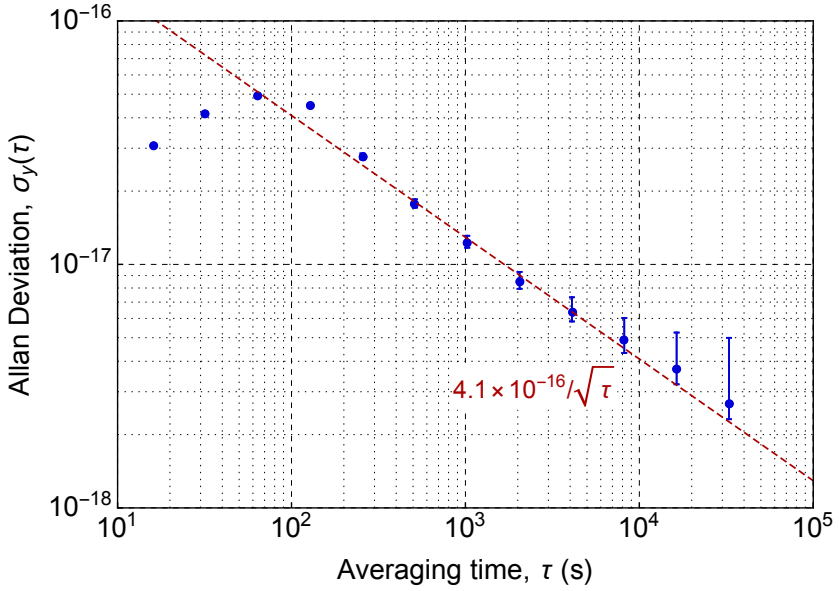

Figure 4.13: Allan deviation of the beat note between the bosonic and the fermionic Sr clocks. The instability is evaluated using the raw frequency data as measured by the counter (Figure 4.12), without any post-processing (a part for the exclusion of the time intervals delimited by the red regions in Figure 4.12).

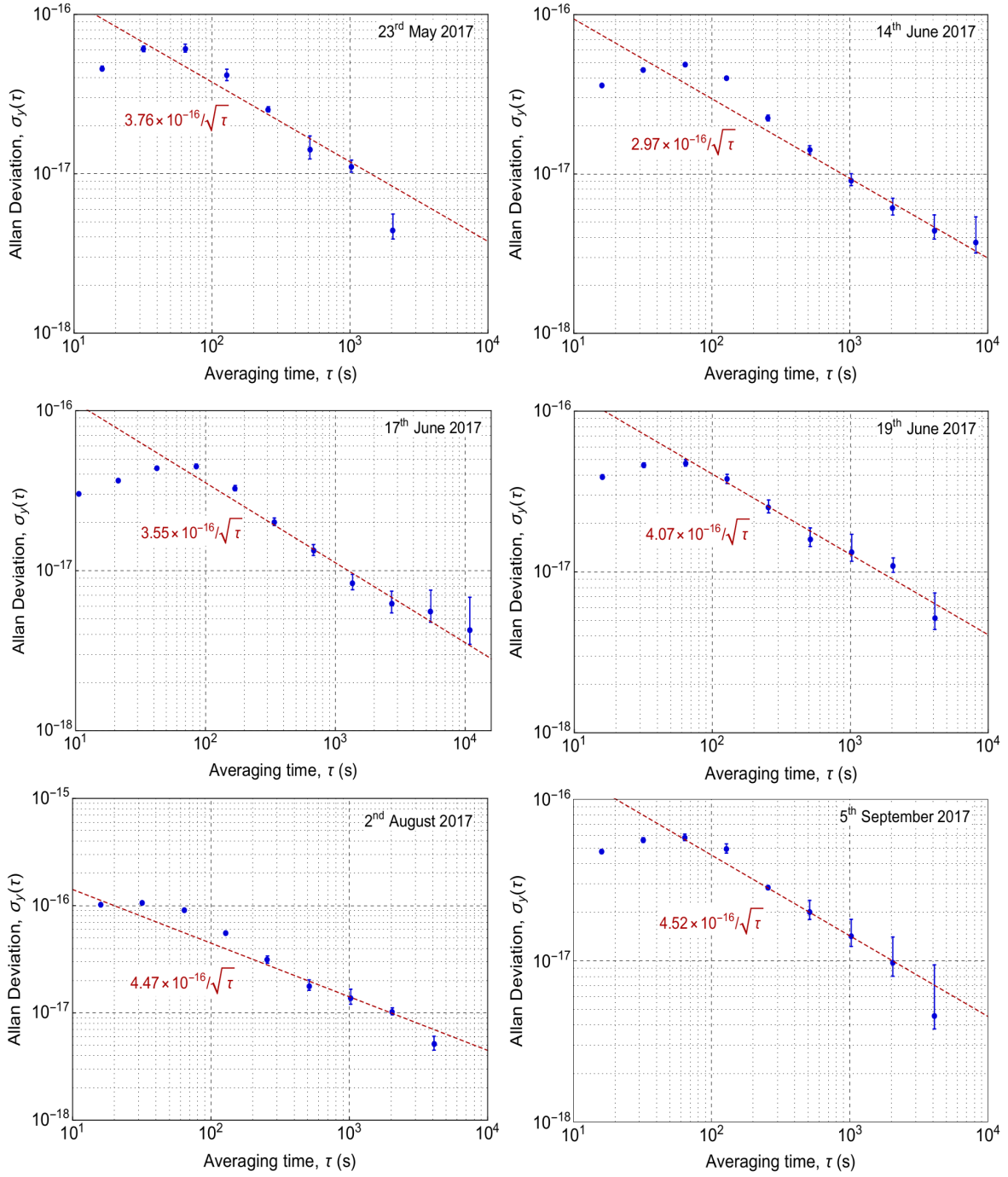

Figure 4.14: Allan deviation of the beat note between the bosonic and the fermionic Sr clocks, acquired between 23/05/17 and 05/09/17.

Chapter 5

A low 10^{-17} uncertainty bosonic clock

Any interaction of the atoms with the external environment, as electric and magnetic fields, laser light, collisions between strontium atoms or with background gases, etc. may introduce a frequency shift of the clock transition. These shifts need to be measured and the corresponding corrections have to be applied to the clock transition frequency in order to obtain the frequency of the unperturbed transition.

Usually, for optical lattice clocks, the largest contribution to the clock frequency shift (and uncertainty) is the one due to the black body radiation (BBR) emitted by the environment surrounding the atoms (unless the interrogation is performed in a cryogenic environment [13]). However, when magnetically induced spectroscopy is used, for bosons, the probe light shift and, mainly, the 2^{nd}-order Zeeman shift can be much larger compared with the BBR shift, and, therefore, be the main contribution to the clock uncertainty [62, 69]. In our work, as already discussed in Section 4.2, we exploit the ultra-long coherence time of the clock laser, being stabilized to the cryogenic Si cavity, such that we reduced the necessary clock laser and bias field intensity, reducing the probe light and 2^{nd}-order Zeeman shifts to sub-Hz level (thus much smaller compared with the BBR shift): also the related uncertainties are reduced to the 1×10^{-17} relative level or below.

Another important shift in bosons is the one due to collisions between the atoms trapped into the lattice: the way how collisions are controlled, in order to reduce the decoherence and line broadening effects, was discussed in Section 4.5. As it will be shown in Section 5.4, by operating in the same conditions, also the collisional shift is strongly reduced, with an uncertainty well below the 1×10^{-17} level.

5.1 BBR shift

As any electromagnetic field, the blackbody radiation generates a differential frequency shift of the clock transition energy levels, which can be written as [87]:

$$\Delta\nu_{\mathrm{BBR}} = \Delta\nu_{\mathrm{stat}}\left(\frac{T}{T_0}\right)^4 + \Delta\nu_{\mathrm{dyn}}\left(\left(\frac{T}{T_0}\right)^6 + \mathscr{O}\left(\frac{T}{T_0}\right)^8\right), \tag{5.1}$$

where $\Delta\nu_{\mathrm{stat}}$ depends on the differential dc polarizability between the clock transition excited and ground state, $T_0 = 300$ K, T is the temperature of the environment around the atoms and the second term is a dynamic correction. The most accurate experimental values for the static and dynamic coefficients are $\Delta\nu_{\mathrm{stat}} = -2.13023(6)$ Hz [88] and $\Delta\nu_{\mathrm{dyn}} = -147.7(7)$ mHz [12].

Experimentally, it is not possible to measure the temperature at the position of the atoms. In order to estimate this temperature, we measure the temperature of the coolest and warmest point (T_{c} and T_{w}) of the vacuum chamber, i.e. the lowest and highest reading among the 18 temperature sensors placed on the chamber (Section 3.10). Thanks to the good temperature stability of the lab, these values are stable within 50 mK for many hours. We indicate with T_{min} the minimum value of T_{c} over the measurement interval and with T_{max} the maximum value of T_{w}. Assuming a rectangular probability distribution for the temperature seen by the atoms [89], the representative temperature results $T = (T_{\mathrm{min}} + T_{\mathrm{max}})/2$ and the uncertainty $(T_{\mathrm{max}} - T_{\mathrm{min}})/\sqrt{12}$ [11]. Usual values for T and ΔT are ~ 22 °C and ~ 350 mK, respectively, resulting in a shift of 5.0×10^{-15} Hz with uncertainty 6×10^{-18} level.

Usually, one would have to consider also the shift due to the BBR from the oven: in fact, even though the oven is far away from the atoms, its temperature is really high (between 350 and 400 °C) and the induced shift can be at few 10^{-17} level. In addition, it can be difficult to precisely evaluate the shift, since one would have to consider not only the BBR with direct line of sight to the atoms, but also the radiation being reflected by the vacuum system inner surfaces [11, 19]. However, in our setup, the atomic shutter shields the atoms from the BBR emitted by the oven during interrogation.

In our analysis we have assumed the BBR all coming from the inner of the chamber. However, even though BK-7 glass filters most of the radiation, a small fraction of the BBR from the external environment can be transmitted by the windows. This may introduce a significant shift if the windows subtend a large solid angle as seen from the atoms position, as it is the case in our experiment ($\Omega \backsimeq 0.4 \times (4\pi)$). Furthermore, the two large windows are in the direction of the inner side of the MOT coils, where the temperature is measured to be between the chamber temperature T_{ch} and $T_{ch} + 1$ K. Assuming again a rectangular probability distribution, the external temperature results: $T_{ext} = T_{ch} + 1.0(3)$ K. We used the

spectral absorption coefficient of BK-7 glass [90] in order to determine the spectrum of the BBR transmitted by the windows. The modification to the spectral power density of the BBR due to the external field, for a solid angle of 4π, is:

$$\Delta S_{BBR}(\nu, T_{ext}, T_{avg}) = e^{-a(\nu)t}(S_{BBR}(\nu, T_{ext}) - S_{BBR}(\nu, T_{avg})) \tag{5.2}$$

Therefore, the BBR frequency is modified as:

$$\Delta\nu_{BBR,ext} = \frac{1}{2hc\varepsilon_0}\int_0^\infty \Delta\alpha(\nu) \times \Delta S_{BBR}(\nu, T_e, T_{avg}) d\nu, \tag{5.3}$$

with $\Delta\alpha(\nu)$ differential dipole polarisability (Section 5.5) given, at low frequencies, by $\Delta\alpha(0) = 4.07873(11) \times 10^{-39}$ m^2 C/V [87]. Evaluating the integral up to 150 THz, since we know the contribution of higher frequencies to be negligible, we obtain $\Delta\nu_{BBR,ext}/\nu_0 = -25(17) \times 10^{-20}$. Here we have considered a solid angle of 4π: in our experiment the solid angle is smaller, therefore we use this value as an upper limit to the shift. The value of the BBR shift shown in Tables 5.1 and 5.2 includes this correction.

5.2 2nd-order Zeeman shift

For the measurement of the 2nd-order Zeeman shift we used interleaved measurement (Section 4.6.2), by changing the current in the coils used to generate the bias magnetic field B_z (MOT coils, see Section 4.3). The current in the second interleaved cycle was changed between five different values ($I_{B,z}$), while the current in the first cycle was always fixed at the reference (operational) value, $I_{ref,z} = +215$ mA (Figure 5.1). The current in the coils was stabilized for both cycles as described in Section 4.3: as uncertainty on the current value, we take the accuracy specified for the digital multimeter used for the stabilization, evaluated for $I_{B,z}$.

The uncertainty on the value of the frequency shift is evaluated from the Allan deviation of the interleaved measurement, extrapolating its value to the measurement time (see Section 4.6.2). Using as reference current $I_{ref,z}$, the frequency shift can be expressed as $\delta\Delta\nu_{B,exp} = \beta((I_{ref,z} - I_{0,z})^2 - (I_{B,z} - I_{0,z})^2)$, where $I_{0,z}$ is the position of the vertex of the parabola. For the measurement reported in Figure 5.1 (September 2017), by fitting the data with this function, we obtain $I_{0,z} = -0.009(2)$ A and $\beta = 17.94(1)$ Hz/A^2. The resulting shift at the reference current is: $\Delta\nu_{B,ref} = \beta(I_{0,z} - I_{ref,z})^2 = -900.2(22)$ mHz, where the uncertainty corresponds to 5.2×10^{-18} in fractional units.

In a previous evaluation of the clock uncertainty budget (June 2017, see Section 5.8) only four switches were implemented in the MOT coils circuit, such that it was possible to generate

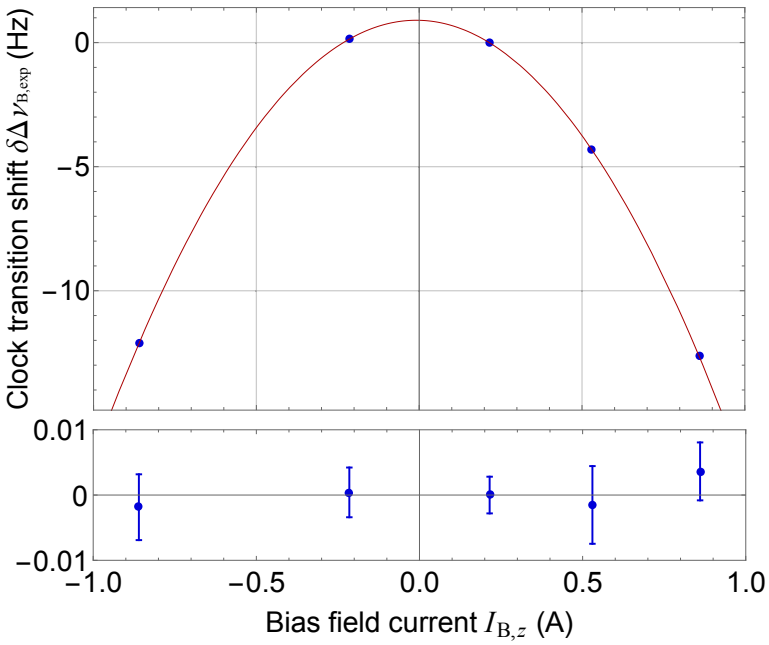

Figure 5.1: Measurement of the 2nd-order Zeeman shift (September 2017), and fit residuals, relative to the frequency shift at the operating point $I_{\mathrm{ref},z} = +215$ mA, which is $\Delta\nu_{B,\mathrm{ref}} = -900.2(22)$ mHz. Details on the fit function are given in the text.

a bias magnetic field only in one direction. Therefore, the resulting uncertainty on the shift evaluation, with similar measurement time, is much higher (Figure 5.2), and results $\sigma_{\Delta\nu_{B,\mathrm{ref}}} = 11.1$ mHz (or 2.6×10^{-17} in fractional units). The different value of the shift, compared with the measurement acquired in September, may be due to a change of the background field. In order to reduce the uncertainty in this case (i.e. fixed direction of the bias field), one way would be to increase the lever arm (i.e. working with higher currents): however, for currents above 1 A we have to change the range of the multimeter, and this corresponds to a much higher uncertainty on the value of the current.

5.2.1 Perpendicular fields compensation

Two pairs of compensation coils are used in the directions perpendicular to the induced bias magnetic field (x and y directions), in order to compensate for the offset field. The measurement of the 2nd-order Zeeman shift is repeated in the same way as it is done for the z-direction, both for the x and y directions, using as reference current $I_{\mathrm{ref},x} = I_{\mathrm{ref},y} = 0$ A. Finally the current is set to the value which minimize the shift, $I_{0,x}$ and $I_{0,y}$. Since the shift is quadratic and the offset field is really small, meaning that also the sensitivity to intensity fluctuations is small, no stabilization is required for the current in these coils.

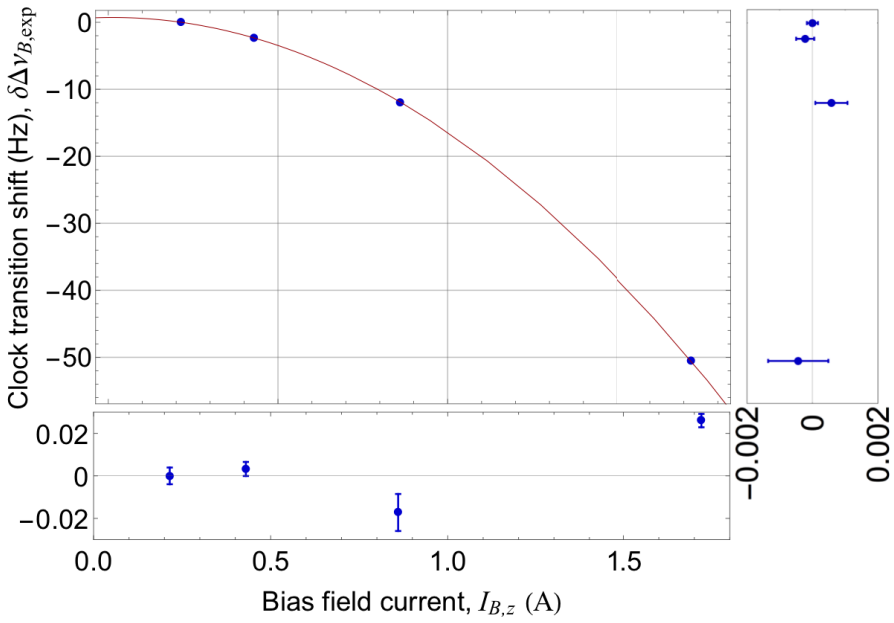

Figure 5.2: Measurement of the 2nd-order Zeeman shift (acquired in June 2017, see text), and fit residuals, relative to the frequency shift at the operating point $I_{\mathrm{ref},z} = +215$ mA, which is $\Delta\nu_{B,\mathrm{ref}} = 722.5(11)$ mHz. Details on the fit function are given in the text.

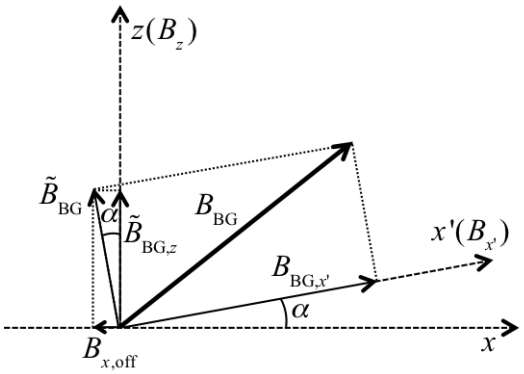

Figure 5.3: Scheme of the magnetic field components for the 2nd-order Zeeman shift measurement. Details are given in the text.

The perpendicular fields compensation was done before the measurement of the 2nd-order Zeeman shift in the z-direction: this is necessary in case the field produced by the compensation coils is not perfectly perpendicular to the z-direction, and consequently it presents some component in that direction which adds to the offset field.

The same circumstance may result in an additional issue. With reference to Figure 5.3, we indicate with x' the direction of the field B_x produced by the compensation coils in the x-axis. x' is separated by an angle α from the x-direction, perpendicular to the bias field B_z. B_{BG} is the background offset field. When we null the $B_{\mathrm{BG},x'}$ component of the background field, the remaining field $\tilde{B}_{\mathrm{BG}}$ presents a residual component along the x-axis ($B_{x,\mathrm{off}}$). This will introduce an additional shift, which is not taken into account in the final measurement of the 2nd-order Zeeman shift. The angle α can be evaluated as follow: we acquire an interleaved measurement with two different values of B_z in the two cycles. Than, the measurement is repeated by varying B_x: from the observed change in the frequency offset between the two cycles and using Equation 2.15, we can evaluate the corresponding change in the offset field in the z-direction ($\Delta B_{z,0}$) and, from that, the angle $\alpha = \tan^{-1}(\Delta B_{z,0}/\Delta B_x)$. When $B_{\mathrm{BG},x'}$ is compensated, the measurement of the 2nd-order Zeeman shift in the z-direction provides the value of $\tilde{B}_{\mathrm{BG},z}$. From that, we can estimate $B_{x,\mathrm{off}}$ and, finally, the residual frequency shift induced by $B_{x,\mathrm{off}}$, as $\Delta\nu_{B,x,\mathrm{off}} = \beta B_{x,\mathrm{off}}^2$ (with $\beta = -23.8(3)$ MHz/T^2 [51]). This was found to be much smaller than 1×10^{-18}. The same was repeated for the y-direction with similar result.

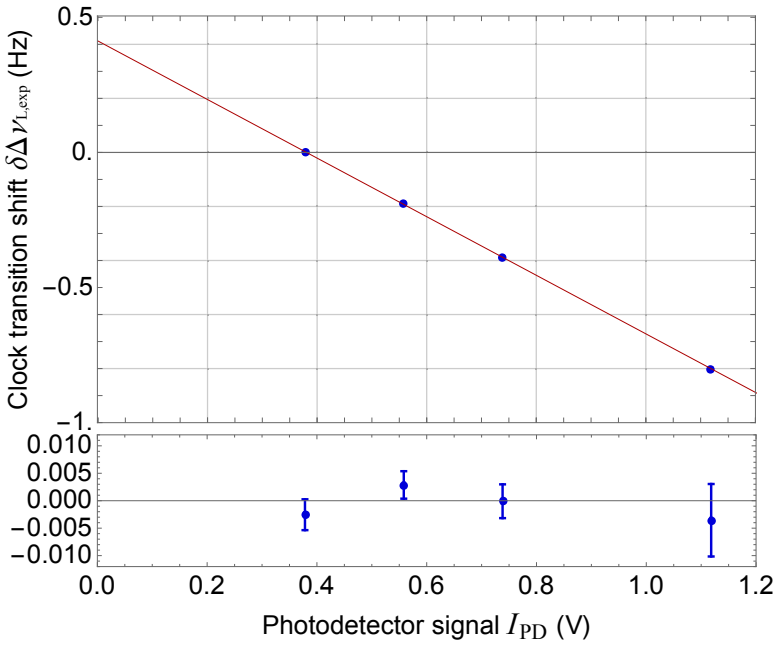

Figure 5.4: Measurement of the probe light shift with residuals. The frequency shift at the operating point of $I_{\mathrm{PD},0} = 360$ mV is $\Delta\nu_{I,\mathrm{exp},0} = 413.0(53)$ mHz. The data are fitted with a linear function.

5.3 Probe light shift

The probe light shift was evaluated in a similar way as the 2$^{\mathrm{nd}}$-order Zeeman shift, with an interleaved measurement, by varying the clock laser beam power. As reference value (first interleaved cycle), it was used the intensity at the operating point $I_{\mathrm{PD},0} \simeq 360$ mV (expressed as photodetector (PD) signal).

Based on the considerations made in Section 4.4, we assume the main source of uncertainty on the PD signal to be the fluctuations in the background level of the PD reading due to electronic noises (as combination of PD noise and noise in the transmission of the signal to the stabilization module): this was measured over few days, and the standard deviation, corresponding to 1.0 mV, is used as uncertainty. The shift at the operating point of $I_{\mathrm{PD},0} \simeq 360$ mV (PD voltage), is $\Delta\nu_{I,\mathrm{exp},0} = 412.5$ mHz, with statistical uncertainty of 5.6 mHz (1.2×10^{-17}). From Equation 2.14 we can infer a laser intensity at the operating point of $I_{\mathrm{CL},0} \simeq 23$ mW/cm^2. The difference compared with the expected shift of 0.50 Hz is attributed to the uncertainty on the calibration of the PD used for the intensity stabilization.

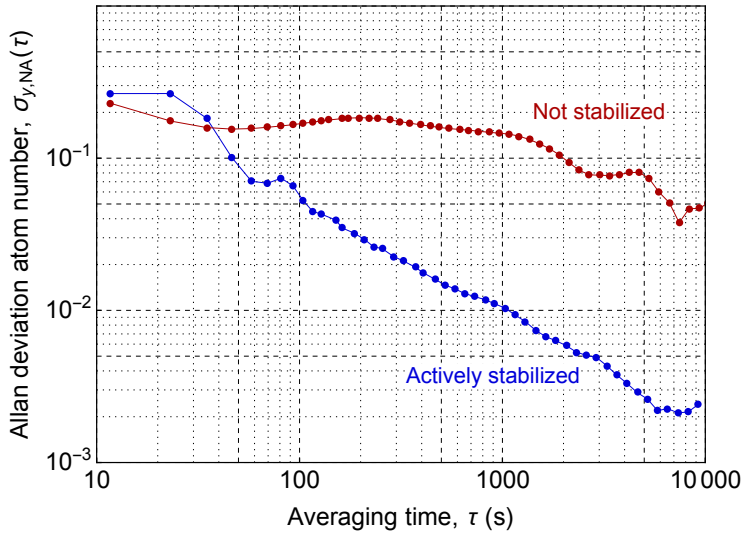

Figure 5.5: Fractional Allan deviation of the number of atoms (i.e. fluorescence signal). The stabilized case corresponds to the first point (atom number ∼1.3 a.u.) in Figure 5.7, while the not stabilized case corresponds to the third point in the same plot (atom number ∼3.2 a.u.).

5.4 Collisional shift

The *s*-wave collisions between atoms in multiply occupied lattice sites may cause a frequency shift of magnitude between a few tens of mHz and a few Hz [62, 63, 67] (Section 2.4.2). As already mentioned in Section 4.5, in this work we tried to reduce the effect of collisions on the transition lineshape (decoherence and line broadening), at first by operating with a small number of atoms (much smaller compared with the number of lattice sites) and secondly by loading the atoms into the lattice starting from a warmer (i.e. less dense) red MOT. As it will be shown in this section, operating in this conditions, allowed us to reduce the shift down to below the 1×10^{-17} level.

Here we used two methods in order to characterize the shift. The standard one, using interleaved measurements with different atom number being interrogated, and a new approach based on the analysis of the clock transition lineshape [91].

5.4.1 Standard measurement

For characterizing the collisional shift, the fluorescence signal from the trapped atoms (which we assume to be proportional to the number of atoms) can be actively stabilized. This allows a more accurate determination of the collisional shift and a control of its stability. The atom number stabilization is implemented by adjusting the power of the Zeeman slower laser beam with a control system. The result of the stabilization is shown in Figure 5.5. For integration

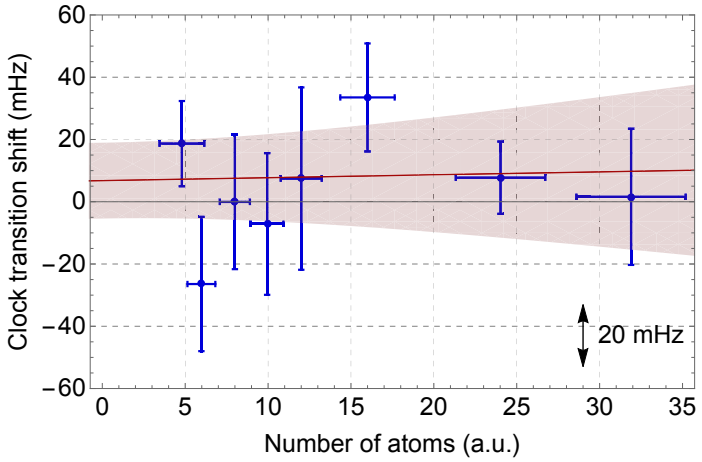

Figure 5.6: Density shift measurement I acquired using an interleaved measurement. The red solid line shows a linear fit; the red region represents the 1σ uncertainty band. The reference value (zero atom difference) corresponds to 8 a.u. and represents the usual operating value. The number of atoms was stabilized during all measurements. The uncertainty on the atom number for each point is given by the standard deviation during the corresponding measurement interval. The resulting shift at the operating point (atom number $\sim$8 a.u.) is 7(12) mHz ($1.6(2.8)\times10^{-17}$).

times above 500 s, the stability of the atom number is improved by one order of magnitude or more compared to the free-running case. We point out that we do not stabilize actively the atom density in the lattice; we rely on the stability of the whole optical system to achieve this as a consequence of fluorescence signal stabilization.

A first measurement of the density shift (measurement I) was acquired in October 2016 (Figure 5.6). At that time, due to not ideal vacuum conditions, the atoms lifetime in the lattice was only few hundreds ms, limiting the maximum achievable interrogation time and thus the clock instability: this was the limiting factor for the final measurement accuracy. Afterwards, the vacuum system was improved (see Section 3.5), as well as the fluorescence detection system, allowing to operate with sub-Hz linewidth and reduced atom number. The measurement was repeated in June 2017 (Figure 5.7). From linear fit to the data, we deduce the frequency shift at the operational atom number and its error: for both the measurements the shift was found to be compatible with zero within the 1σ uncertainty (12 mHz (2.8×10^{-17}), and 2.2 mHz (5.2×10^{-18}), respectively). In order to make sure that the interrogation conditions are similar, for the second measurement we have acquired sideband spectra corresponding to the different atom numbers and found differences in the trap frequency smaller than 4%, and radial and longitudinal atoms' temperature changes smaller than 25% and 20%.

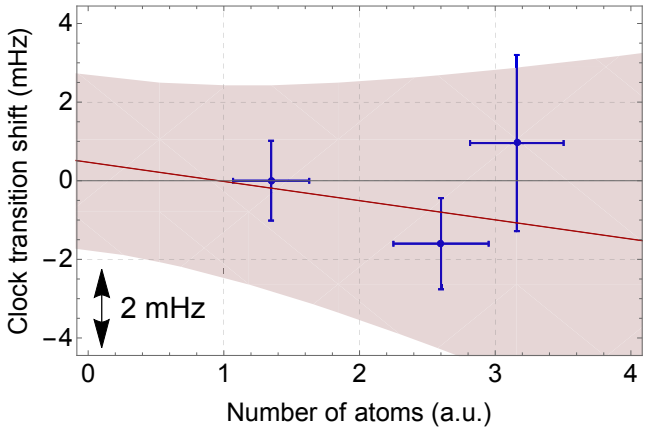

Figure 5.7: Density shift measurement II acquired using a reference clock, the PTB Sr clock. The red solid line shows a linear fit; the red region represents the 1σ uncertainty band. The atom number was stabilized only for the first data point. The uncertainty on the atom number for each point is given by the standard deviation during the corresponding measurement interval. The three intervals lasted (from low to high atom number) 23200 s, 20880 s and 4640 s. The resulting shift at the operating point (atom number $\sim$1.3 a.u.) is 0.5(22) mHz ($1.1(5.2)\times10^{-18}$). Note that the atom number scales of measurement I and II are not the same.

5.4.2 Alternative evaluation by lineshape analysis

In this work we suggest a different approach for the evaluation of the shift, based on the lineshape analysis [91]. The collisional effects on the clock transition lineshape (broadening and decoherence) were already discussed in Section 4.5. We observed that the transition lineshape was always slightly asymmetric: therefore, instead of using a normal lorentzian fit, we decided to model the lineshape with the sum of two lorentzian profiles. One results from atoms in singly-occupied lattice sites, while the second one from atoms in multiply occupied lattice sites. Thus, the first profile is supposed to be almost Fourier-limited, while the second one shall be broader and with negative frequency shift. The resulting function seems to fit well to experimental data (Figure 5.8, top).

In order to verify the model, we used photoassociation (PA) for reducing the number of atoms in multiply occupied lattice sites [70]: two atoms interact with a photon from the PA beam and form an excited Sr_2 molecule. This can decay to two hot atoms, which are lost from the trap. The PA beam, obtained from the same laser as the 689 nm cooling laser, was overlapped with the lattice laser, with slightly larger waist. We used the PA transition $\sim$ 222 MHz red detuned from the $^1S_0 - ^3P_1$ transition [62]: the PA wave is applied for 600 ms before the clock interrogation, with an intensity of about 1 W/cm^2. A typical PA line, obtained by stepping the PA beam frequency using a double-pass AOM, is shown in Figure 5.9. The contrast could be improved, by applying larger PA beam intensity or longer pulse duration:

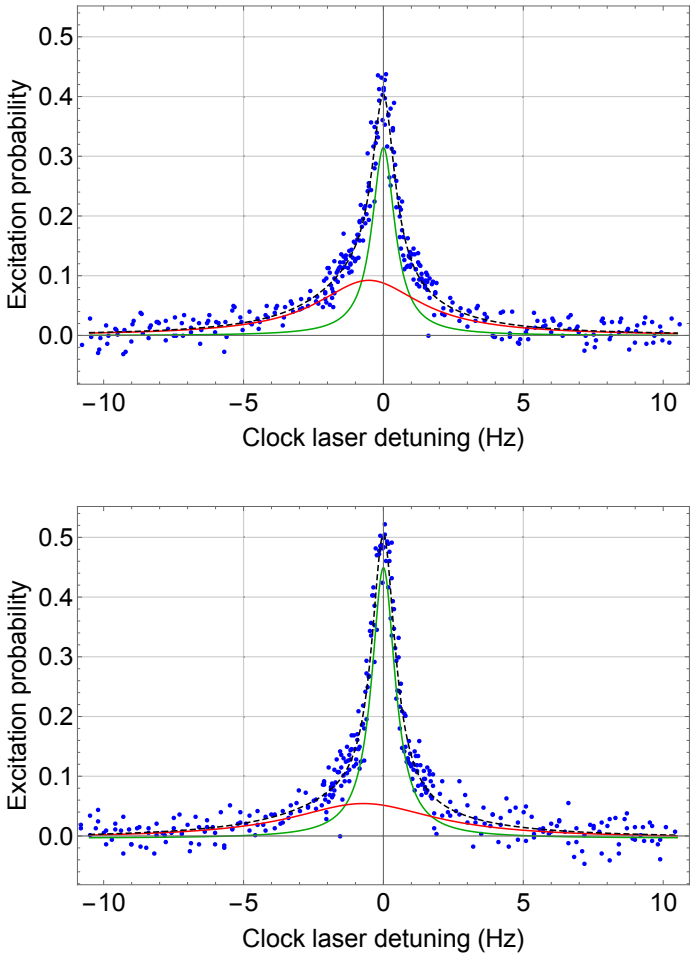

Figure 5.8: Clock transition scans acquired with 1.0 s interrogation time. Top: with detuned photoassociation laser applied before each atom interrogation; bottom: with resonant PA laser. The blue dashed curve is the fit function including a main line (green) and a second line (red). Details are given in the text.

however, we found that this causes more atoms to be lost for processes different than PA (e.g. heating and power broadening).

Than, two clock transition lines were acquired: one with the PA beam ~ 4 MHz red detuned from the transition (Figure 5.8, top), and one with the beam on resonance (Figure 5.8, bottom). In this way, atom loss mechanisms different than PA are common to both scans. Since the locking to the Si cavity was not available at that time, the PTB clock laser, to which the SOC clock laser is stabilized, was locked only to the 48 cm cavity [77]: thus, we used $T_\pi = 1.0$ s as interrogation time. It is clear that, when PA is applied, the contribution of the red profile is reduced by about a factor of two, this confirming the validity of the model.

Thus, we can assume the green profile to represents the unperturbed transition (i.e. atoms

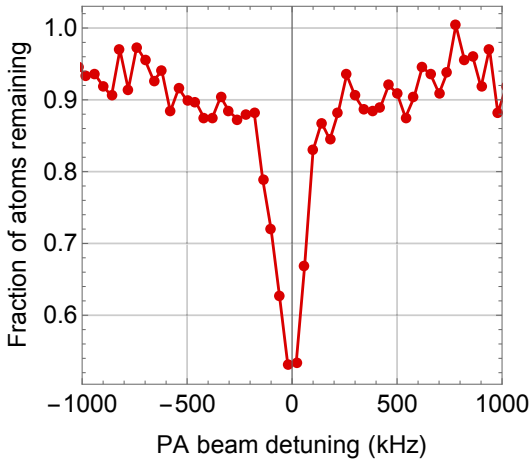

Figure 5.9: Typical PA transition. In order to evaluate the fraction of atoms remaining into the trap, the number of atoms is measured twice, once with the PA beam ~ 4 MHz red detuned from the transition (fixed frequency) and once with the beam at a frequency stepped across the PA transition. This ensures that all effects causing atom disturbances due to the PA beam (e.g. heating, power broadening, etc.), except for the PA process itself, are common in both cycles.

not affected by collisions), such that the collisional shift can be evaluated as line pulling due to the red profile. In particular, in the plots in Figure 5.10 is reported the difference between the center of the profile from singly occupied atoms (green profile) and the point halfway between the two sides of the lineshape (blue profile), at different excitation probabilities. The line pulling starts to increase significantly for excitation probabilities below 25-30%. Therefore, it is convenient to chose a locking point well above that level: this is done by interrogating the clock transition at two frequencies closer to the center of the main profile than at half height (as it is done usually).

The collisional shift was evaluated in this way for the second measurement of the ^{88}Sr $-^{87}$Sr isotope shift (September 2017, see Section 5.9): the use of longer interrogation times ($T_\pi =$ 4.0 s), thanks to the availability of the locking to the silicon cavity, allows to further reduce the effect of the line pulling (Figure 5.10, right). It is important to mention that the isotope shift measurement was done before the implementation of PA: however, we were operating with rather high red MOT temperature and this was enough to obtain sufficiently low density. The shift resulted $\Delta\nu_{\mathrm{LP}} = 2.5(15)$ mHz $(5.7(34) \times 10^{-18}$ in fractional units), which is consistent with the value resulting from the classical measurement (Section 5.4.1).

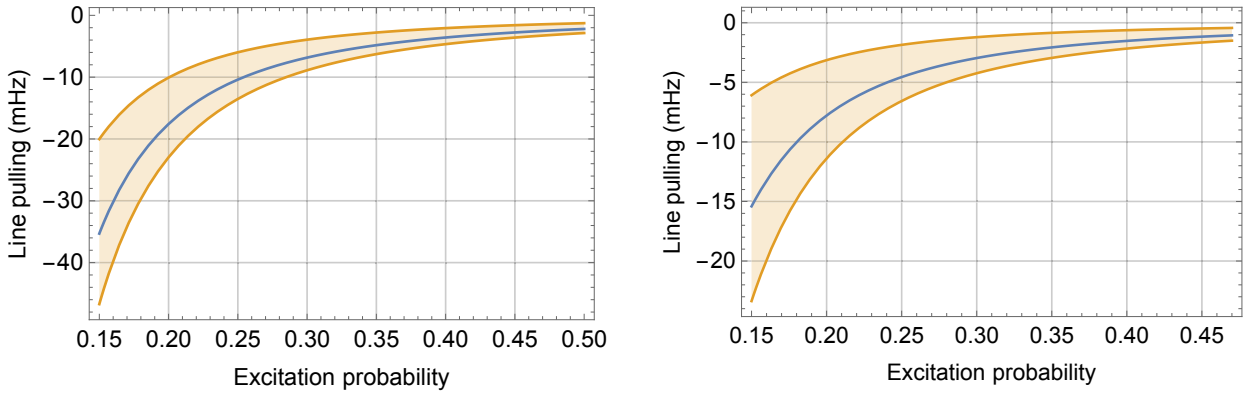

Figure 5.10: Line pulling of the clock transition lineshape due to the profile resulting from atoms in multiply occupied sites (red profile in Figure 5.8). Right: with interrogation time $T_\pi = 1.0$ s (evaluated from the transition in Figure 5.8, bottom); Left: with $T_\pi = 4.0$ s.

5.5 Lattice light shift

The trapping light field interacts with the atoms producing a differential shift of the ground and excited state of the clock transition, which results in a frequency shift (AC Stark shift). In the early years the AC lattice light shift has prevented the progress of optical lattice clocks, until when the idea of the so-called "magic" wavelength, which allows the cancellation of the AC Stark shift at the first order, has paved the way for their development [20]. In a first approximation this shift can be described as electric dipole interaction (E1):

$$h\Delta\nu_{\mathrm{s}}^{\mathrm{E1}} \approx \frac{\partial\Delta\alpha^{\mathrm{E1}}}{\partial\nu}\Delta\nu_{\mathrm{L,m}}\frac{U_0}{E_{\mathrm{r}}}, \tag{5.4}$$

where $\Delta\alpha^{\mathrm{E1}} = \alpha_{\mathrm{e}}^{\mathrm{E1}} - \alpha_{\mathrm{g}}^{\mathrm{E1}}$ is the differential dipole polarizability, ν is the lattice frequency, U_0 is the trap depth and $E_{\mathrm{r}} = \hbar k_{\mathrm{L}}^2/(2\pi)$ the recoil energy. $\Delta\nu_{\mathrm{L,m}}$ is the detuning of the lattice frequency from the magic value, corresponding to the wavelength for which the ground and excited states of the clock transition experience the same shift (of the order of 10^{-10} as fractional shift [92]). Close to this value also the sensitivity to the changes in the lattice wavelength is small, such that a control of the lattice frequency within few hundreds kHz of the magic value allows a cancellation of the AC Stark shift at the level of low 10^{-18}.

Aiming to accuracy in the low 10^{-17} level, additional smaller contributions to the lattice light shift have to be taken into account. These are:

- Vector and tensor shift, related to the hyperfine structure (in fermions) which generates a vector and tensor polarizability [92]. Due to the null angular momentum of both

the clock states, the vector and tensor shifts are null for bosons, which therefore are insensitive to lattice polarization effects.

- Differential hyperpolarizability between the two clock states, due mainly to two-photon resonance from the $^3P_0$ excited state [20].
- Shift due to higher multiple coupling generated by dipole magnetic (M2) and quadrupole electric (E2) interactions [93]. These two shifts present a linear dependence on the lattice light intensity (same as for the E1 shift) but are sensitive to the intensity variation in the axial direction, leading to different oscillation frequency. This leads to a dependence of the shift on the average motional state occupation n, i.e. on the atoms temperature. For Sr this contribution has been demonstrated to be at low 10^{-18} level [92, 94].

The complete expression for the lattice light shift, including all the contributions, is [95]:

$$\begin{aligned} h\Delta\nu_{\mathrm{ls}} \approx & \left(\frac{\partial\Delta\alpha^{\mathrm{E1}}}{\partial\nu}\Delta\nu_{\mathrm{L,m}} - \Delta\alpha^{\mathrm{qm}}\right)\left(n+\frac{1}{2}\right)\left(\frac{U_0}{E_{\mathrm{r}}}\right)^{1/2} + \\ & - \left(\frac{\partial\Delta\alpha^{\mathrm{E1}}}{\partial\nu}\Delta\nu_{\mathrm{L,m}} + \frac{3}{4}\Delta k_{\mathrm{H}}(2n^2+2n+1)\right)\frac{U_0}{E_{\mathrm{r}}} + \\ & + \Delta k_{\mathrm{H}}(2n+1)\left(\frac{U_0}{E_{\mathrm{r}}}\right)^{3/2} - \Delta k_{\mathrm{H}}\left(\frac{U_0}{E_{\mathrm{r}}}\right)^2, \end{aligned} \tag{5.5}$$

where $\Delta\alpha^{\mathrm{qm}}$ is the multipolar polarizability and Δk_{H} is the hyperpolarizability coefficient.

Experimentally, in order to identify the magic wavelength position, we used interleaved measurements (Figure 5.13, blue points), using two different lattice depths (evaluated from sideband spectroscopy), 87 E_{R} (shallow lattice) and 162 E_{R} (deep lattice). The fit provides the position corresponding to zero shift. We are able to know the absolute value of the magic wavelength, since we can beat the lattice laser with PTB stationary system lattice laser, which is stabilized to the frequency comb referenced to a hydrogen maser. The resulting lattice frequency is ν_{magic} =368554745(2) MHz. Our value is 4σ away from the one recently reported for ^{88}Sr in [62]: $\nu_{\mathrm{magic,Tak}}$ =368554778(8) MHz. The difference may be attributed to different spectra of the lattice laser (see next Section). The lattice light shift is then evaluated by using Equation 5.5: in operating conditions, usually, a small lattice depth is used (i.e. <100 E_{R}).

5.5.1 The problem of the TA ASE spectrum

For the first evaluation of the shift we used, as lattice laser, the SOC transportable tapered amplifier (TA) laser. However TA systems present a known problem for this application, which

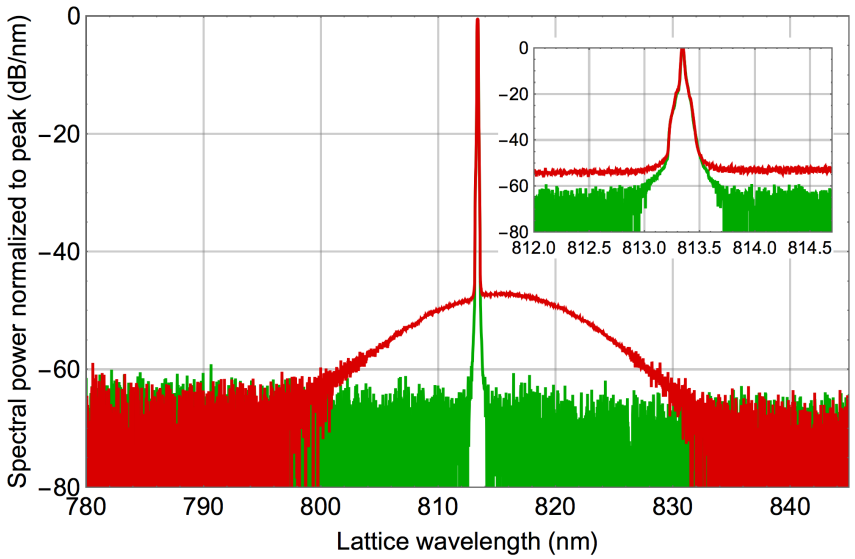

Figure 5.11: Spectrum of the TA laser measured with the spectrum analyzer (model AQ6370, from Yokogawa). Red: without filter. Green: with filter.

is the presence of TA amplified spontaneous emission (ASE, Figure 5.11). Even though the spectral power of the ASE is rather small (in our case the integrated power is about 1% of the carrier power), it covers a wide spectral range: since the shift is proportional to the detuning (from the fit in Figure 5.13 results about 5 (Hz/nm)/E_R), the contribution to the lattice shift can be significant. This means also that any small change in the ASE spectrum may produce a large drift of the clock frequency, making it unusable aiming to uncertainty and instability below 1×10^{-16} level. This effect was observed in previous works: for example in [10] it was reported a fluctuating discrepancy between two clocks, using a TA for the lattice, in the order of 10^{-15} level, attributed to the ASE spectrum; while in [35] it was observed a frequency difference at the level of 3×10^{-16} between two similar clocks using one a TA and one a TiSa laser (having greater spectral purity), even though the ASE spectrum was filtered using a Bragg grating.

In this work we have been tested a new filter, also based on a grating, provided by Toptica Photonics: the bandwidth of the filter is 12 GHz. The filter is fiber coupled and placed in between the lattice laser breadboard and the atomic package. The spectrum of the laser after the filter is reported in Figure 5.11 (in green). As comparison, the magic wavelength was measured once without the filter (Figure 5.12): the resulting value was much higher ($\sim$ 260 MHz) compared with the one measured with the filter (measurement in Figure 5.13). Furthermore the presence of many outlier points, suggests that, as expected, the shift varies in time: since every point corresponds to about one hour of measurement, and the points were acquired sequentially (from higher to lower lattice frequency), we can infer a change in the shift of the

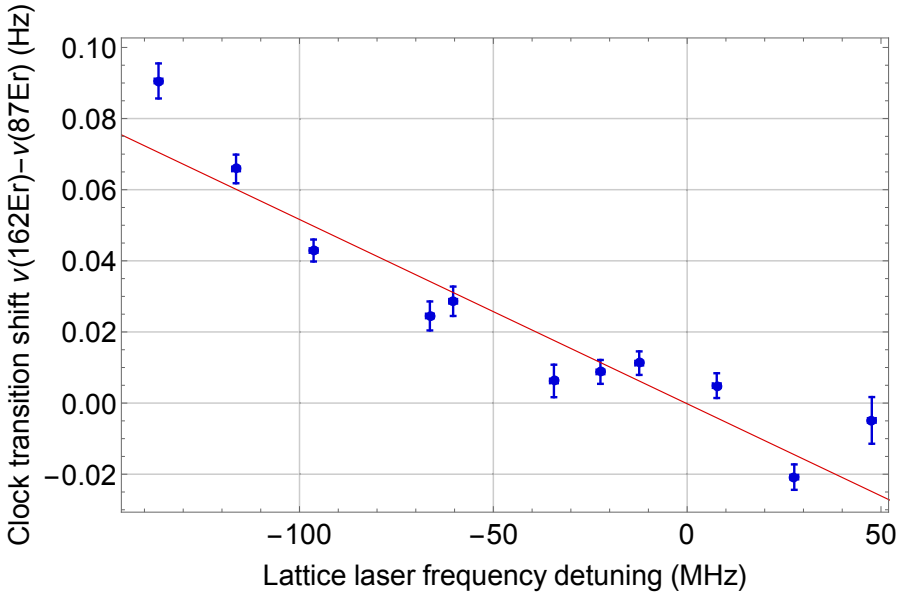

Figure 5.12: Measurement of the lattice laser AC-Stark shift, using the TA without the filter. The lattice frequency axis is centered to the value of the magic wavelength. The difference compared to the magic wavelength measured with TA+filter (Figure 5.13) is $\sim$ 260 MHz.

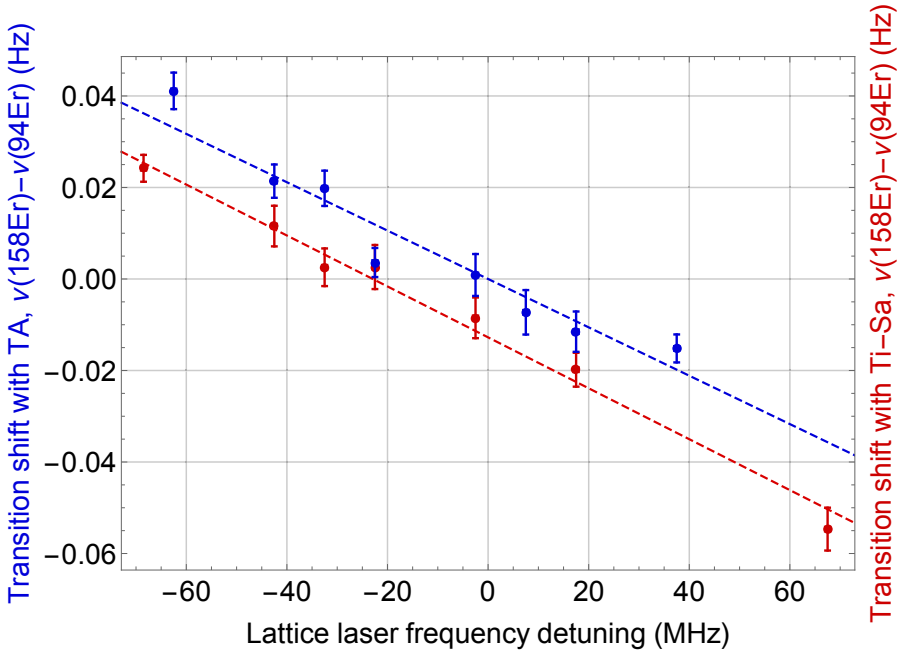

Figure 5.13: Measurement of the lattice laser AC-Stark shift. Blue: with TA+filter; Red: with TiSa. The lattice frequency axis is centered to the value of the magic wavelength as measured with the TA.

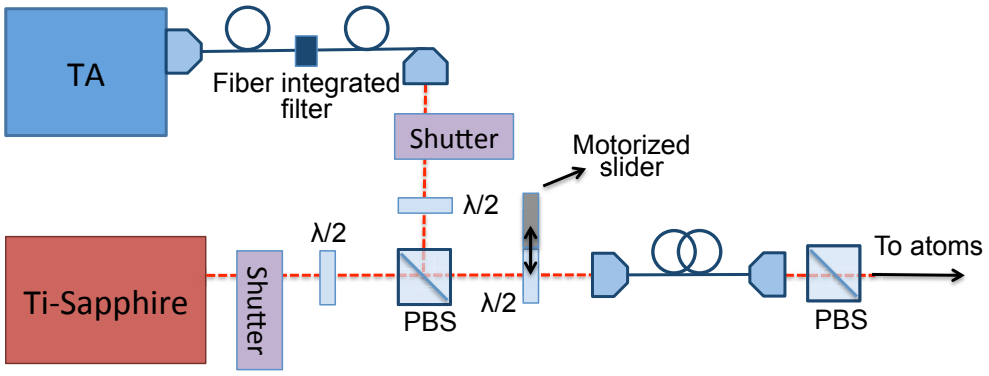

Figure 5.14: Scheme for the interleaved measurement using the TA and TiSa lasers.

order of many mHz (few 10^{-17}) on hourly basis.

5.5.2 Comparison with Ti-Sapphire laser

In order to characterize the performance of the filter, we switched to a TiSa laser (from Tekhnoscan), provided by PTB. The TiSa is known to have a greater spectral purity compared with the TA, thus it can be used as reference. The laser is stabilized to a 10 cm long Fabry-Pérot cavity: since the drift of the cavity is too large, we further stabilize it to the FSS. This also allows to have a direct comparison between the TA and TiSa frequency (since it was verified the drift of the FSS to be smaller than few hundreds kHz every few days). At first, we repeated the measurement of the AC-Stark shift (red points in Figure 5.11): the resulting magic wavelength is 23 MHz away compared with the one obtained with the TA, this being a rather small value considering that a difference of few tens of MHz is observed also when using different TiSa lasers [19].

The final test is the comparison between the clock frequency as measured running the clock with the TA (with filter) and with the TiSa. As reported in Section 5.9 the measurement of the ^{88}Sr–^{87}Sr isotope shift was repeated twice: once using the TA and once using the TiSa. The offset between the two measurements was rather small (less than 2σ, or 5×10^{-17}): even though it is difficult to determine whether the offset is due to the different lattice laser or to other causes, this suggest that the shift due to the ASE is controlled better than 5×10^{-17} level.

A more accurate way for measuring the frequency offset is with an interleaved measurement, by using in one cycle the TA and in the other cycle the TiSa. The scheme of the setup that we used for this measurement is shown in Figure 5.14: the light from the TA breadboard is delivered to the TiSa breadboard passing through the filter, and overlapped to the beam from the TiSa using a PBS cube. Two shutters are used to close either one of the two beams. The light from the two lasers is delivered via optical fiber to the atomic package. To make

sure that the two beams enter into the fiber with the same polarization, a half waveplate is placed after the cube and mounted on a motorized slider stage, such that it can slide in and out every cycle. For the measurement both the lasers were stabilized at the respective magic wavelength: in particular the TA was locked to the FSS, while the TiSa was stabilized to the Fabry-Pérot cavity and then manually tuned to the proper wavelength by looking at the beatnote with the TA. The measurement resulted in an offset of 2.1(52) mHz ($0.5(12) \times 10^{-17}$), where the uncertainty is a combination of the statistical uncertainty (9×10^{-18}) and of the systematic uncertainties on the AC-Stark shift for the TA and TiSa (4×10^{-18} and 7×10^{-18} respectively). Therefore we have verified that the filter allows a control of the TA ASE effect at the 1×10^{-17} level, which is the goal uncertainty for our work. This represents an encouraging result, mainly for applications as transportable or space clocks, where the use of diode laser based systems is preferable to TiSa lasers, which are usually much more complex and require more power compared with a TA.

5.6 DC-Stark shift

The presence of residual electric fields in the interrogation region may produce a shift of the clock transition. This effect was reported for the first time in a work by Syrte group [96], while a similar effect was observed at PTB [11].

For measuring the shift, we run a measurement similar to the one of the 2^{nd}-order Zeeman shift, i.e. by applying an additional external electric field and measuring the resulting frequency shift. Three pairs of electrodes were placed in the three spatial directions, around the chamber windows (see Section 3.8). The most critical direction is the horizontal one, since the two large windows are only 7 mm away from the center of the chamber: thus we started from this axis. In a first measurement (measurement I), we used the PTB stationary clock as reference, by applying at first a positive field, ± 10 V and ± 25 V, and than a negative field, ∓ 10 V and ∓ 25 V (Figure 5.15). Since we expect a quadratic dependence on the applied field, the shift can be expressed as $\delta\Delta\nu_E = \alpha((V_{\text{ref},z} - V_{0,z})^2 - (V_{E,z} - V_{0,z})^2)$, where $V_{\text{ref},z} = 0$ V is the reference voltage, $V_{0,z}$ is the position of the vertex of the parabola and $V_{E,z}$ is the applied voltage. It is clear that the fit function does not fit properly the experimental data. The problem was attributed to a redistribution of electrical charges on the surface of the vacuum chamber induced by the applied field, such that the background offset field was changing while acquiring the measurement. This seems to be confirmed by the fact that it was noticed a drift of the clock frequency in the first few thousand seconds after changing the field (see Figure 5.17).

In order to avoid the problem, for measurement II (Figure 5.16) we implemented a switch system which allows to run interleaved measurement by applying alternatively a positive and

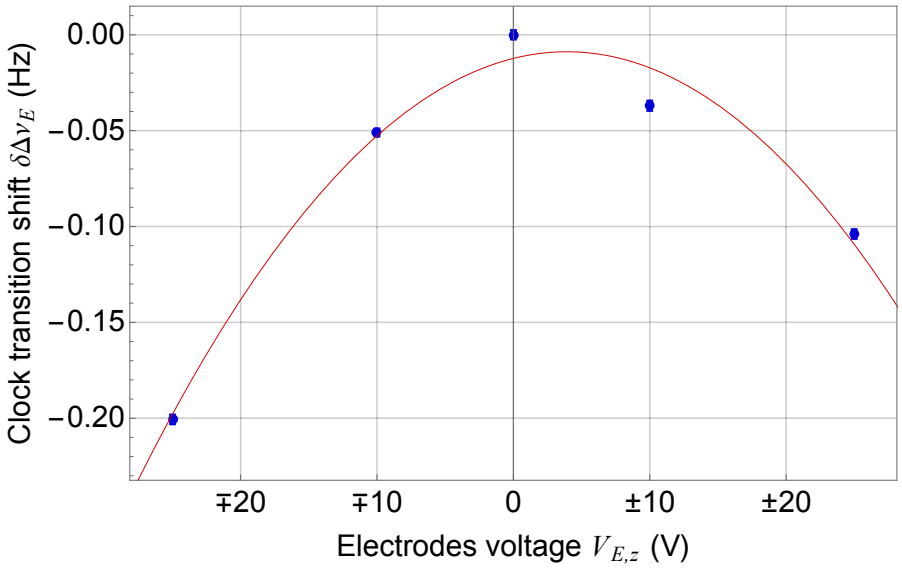

Figure 5.15: DC-Stark shift measurement I (z-direction).

negative field in the two interleaved cycles. At first we acquired two clock transitions by applying ± 40 V and 0 V: these were used to set the position of the point at ± 40 V (as difference between the center of the two lines) and the uncertainty on the point at 0 V (whose frequency was arbitrarily set to zero). Then, we run an interleaved measurement by applying ± 40 V in the first cycle and ∓ 40 V in the second cycle: in this way we determined the position of the point at ∓ 40 V. By fitting the data with the above-mentioned function, we obtain $V_{0,z} = 0.002(2)$ V and $\alpha = 0.59(2)$ Hz/V^2. The resulting shift when no field is applied is $\Delta\nu_{E,\mathrm{ref}} = \alpha(V_{0,z} - V_{\mathrm{ref},z})^2 = 0.77(6)$ mHz $(1.8(2) \times 10^{-18})$. The same measurement was acquired in the perpendicular directions, and the shift resulted well below the 10^{-18} level: this is not surprising, since the windows in the x and y axis are much farther away from the atoms (~ 24 mm).

5.7 Other shifts

5.7.1 Gravitational red-shift

For the measurement of the isotope shift (Section 5.9) it was necessary to correct the measured frequency offset compared with the PTB ^{87}Sr clock for the gravitational red-shift, since the height of the two systems (i.e. the position of the atoms being interrogated) is different. The two clocks are standing in two adjacent laboratories, such that the height difference could be measured with standard leveling, using a spirit level and measuring the height of the center of the two atomic chambers (atoms positions) from the floor with a ruler. The difference results

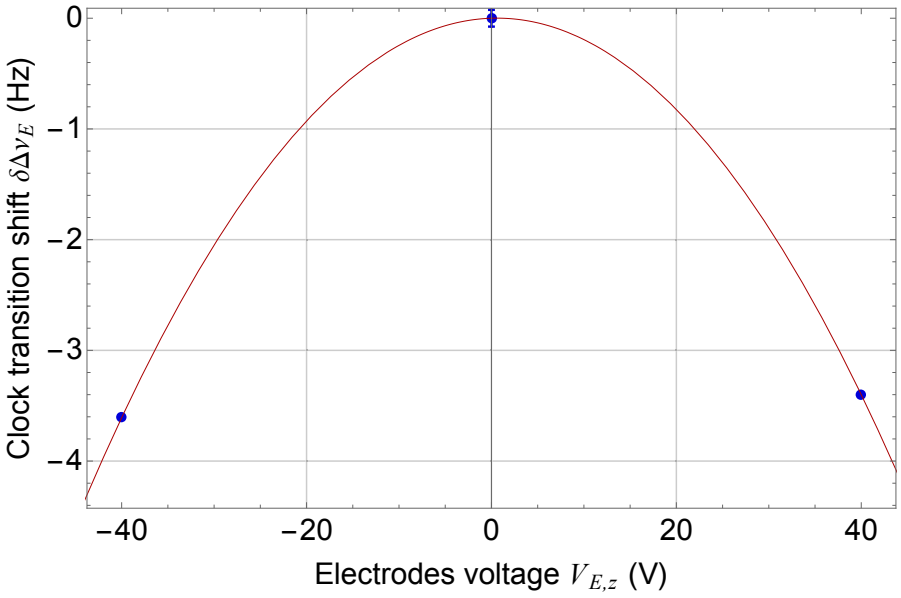

Figure 5.16: DC-Stark shift measurement II (z-direction).

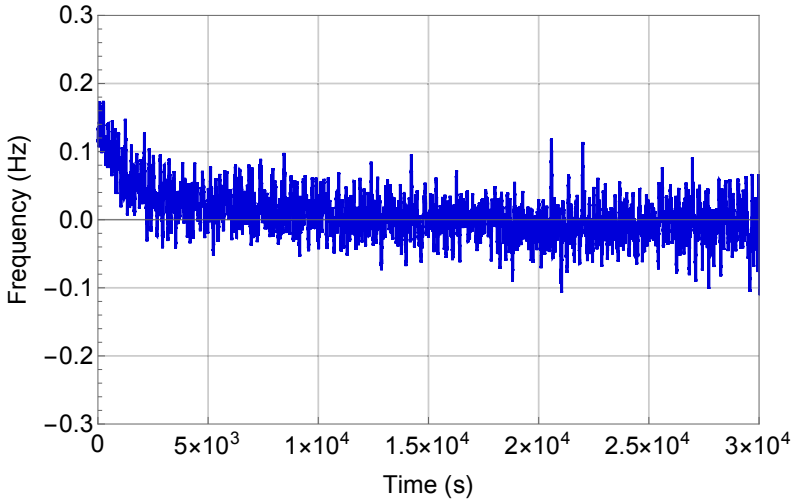

Figure 5.17: Raw data for the interleaved measurement used for the point with abscissa "$\mp 10V$" in the plot in Figure 5.15. The field was switched from "$\pm 10V$" to "$\mp 10V$" at $t = 0$ s. The initial drift is attributed to a redistribution of the charges on the surfaces of the chamber.

$\Delta h = +465(6)$ mm. Thus, the difference in the gravitational red-shift is $\Delta\nu_g = g\Delta h\nu_0/c = 21.8(3)$ mHz ($5.1(1)\times10^{-17}$), where ν_0 is the clock transition frequency.

5.7.2 Background gas collisions

Apart for collisions between Sr atoms trapped in the lattice, also collisions with other gases in the vacuum system produce a frequency shift. For the evaluation of the frequency shift we follow the procedure described in [11]: the density of a number of background gases (H, He, H_2, Sr and Xe) is evaluated based on the lattice lifetime ($\tau_L = 5.6$ s). Than the long-range coefficients C_6 for both the clock states, as given in [97], are used in order to determine the frequency shift due to the collisions with the different gases (this is done by using a code provided by PTB). We use the larger shift as upper limit to the frequency shift: in our case results $\Delta\nu_{BG} = 0.58(58)$ mHz (or $1.3(1.3)\times10^{-18}$).

5.7.3 Servo error

As described above, the clock laser stabilization cycle consists in two interrogations of the clock transition, on the two sides of the transition line: afterwards, the frequency error is evaluated and the clock frequency is corrected accordingly. If the clock laser frequency is drifting, due to the drift of the reference cavity, the delay between the atoms interrogation and the implementation of the correction causes a frequency shift, since there will be always a constant (or variable, in case the drift is not perfectly linear) offset between the clock transition and the clock laser frequencies [98]. However, during the isotope shift measurement (Section 5.9) our clock laser was locked to the PTB system clock laser, stabilized to the ^{87}Sr clock transition, therefore the drift is null.

5.8 Uncertainty budget

Two completely independent evaluations of the ^{88}Sr clock uncertainty were carried. A first one, in June 2017, using the TA laser for the lattice, the second one, in September 2017, using the TiSa laser.

Apart for the different lattice laser, the main change in the setup was the implementation of three additional switches for the MOT coils (leading to a total of seven switches, see Section 5.2): in this way, if for the first measurement it was possible to produce a bias field only in one fixed direction (Figure 5.2), after this change the bias field direction could be reversed from one interleaved cycle to the next. This allows a more accurate determination of the shift, with shorter averaging time (Figure 5.1).

Effect	correction (10^{-17})	uncertainty (10^{-17})
BBR shift	495.8	0.6
BBR oven	0	0
Lattice shifts	-0.3	0.5
Probe light shift	124.7	1.3
Cold collisions	0.1	0.5
2^{nd}-order Zeeman shift	168.3	2.6
Background gas collisions	0.1	0.1
DC Stark shift	0	0.7
Servo error	0	0
Total	784.2	3.1

Table 5.1: Uncertainty budget for the ^{88}Sr clock, with TA laser used for the lattice (June 2017).

Effect	correction (10^{-17})	uncertainty (10^{-17})
BBR shift	523.4	0.8
BBR oven	0	0
Lattice shifts	2.2	1.1
Probe light shift	96.1	1.3
Cold collisions	0.6	0.3
2^{nd}-order Zeeman shift	209.7	0.5
Background gas collisions	0.1	0.1
DC Stark shift	0.2	0.2
Servo error	0	0
Total	827.3	2.0

Table 5.2: Uncertainty budget for the ^{88}Sr clock, with TiSa laser used for the lattice (September 2017).

An additional change was the replacement of the filter in the clock laser optical setup, the one placed just before the lattice laser back-reflection (Section 3.9): in order to be less sensitive to electronic noises on the PD signal for the intensity stabilization, it was decided to reduce by a factor of two the transmissivity of the filter, such that, with the same amount of light going to the atoms, we could get twice the PD signal amplitude.

For the collisional shift, in the first case we evaluated the shift with the classical method (Figure 5.7), while for the second measurement we used the approach based on the lineshape analysis (i.e. line pulling, Section 5.4.2) .

In Table 5.1 is reported the first uncertainty budget. As expected the clock uncertainty is dominated by the uncertainty on the 2^{nd}-order Zeeman shift measurement. In the second evaluation (Table 5.2) this is almost four times smaller, while the main contribution to the clock uncertainty comes from the lattice light shift and the probe light shift measurements: in

Effect	correction (10^{-17})	uncertainty (10^{-17})
BBR shift	492.2	1.5
BBR oven	0.9	0.9
Lattice shifts	0.9	0.4
Probe light shift	0	0
Cold collisions	0	0.2
2nd-order Zeeman shift	3.4	0.1
Background gas collisions	0.8	0.8
DC Stark shift	0.2	0.1
Total	498.4	2.0

Table 5.3: Uncertainty budget for the PTB ^{87}Sr clock (September 2017). Courtesy of PTB group.

both cases one of the limiting factor was the measurement time since, due to technical reasons, we had to perform all the measurements necessary for evaluating the clock uncertainty in a limited time (less than 48 hours); in addition, for the probe light shift measurement, the lever arm was limited by the maximum available clock laser power.

The resulting uncertainty for the second measurement ($\sigma_{\nu_0} = 2.0 \times 10^{-17}$), represents a factor of 30 improvement compared with the best value reported so far for bosonic optical lattice clocks [62].

5.9 ^{88}Sr –^{87}Sr isotope shift

We evaluated the ^{88}Sr–^{87}Sr isotope shift for both the measurements (June and September 2017). A typical uncertainty budget of the PTB ^{87}Sr clock is given in Table 5.3: this is the one corresponding to the measurement acquired in September 2017. The uncertainty is the same as for the bosonic clock, but the main contribution is coming from the BBR shift, since the vacuum chamber is much larger and this leads to larger temperature gradients. Furthermore, no atomic shutter is used for shielding the atoms from the BBR emitted by the oven. For the first measurement (June 2017) the resulting uncertainty was $\sigma_{\nu_{0,87\mathrm{Sr}}} = 1.6 \times 10^{-17}$.

For the isotope shift evaluation in September 2017, four measurements were acquired within 48 h (Figure 5.18): the resulting value for the shift is obtained as weighted average. In the same time interval, we measured the lattice light shift, probe light shift, 2nd-order Zeeman shift, collisional shift and DC-Stark shift (as reported in Table 5.2). It is important that the probe light shift and 2nd-order Zeeman shift measurements were acquired at the same time as the isotope shift measurement, since a small misalignment between the lattice laser and clock laser beam or a small change in the background offset magnetic field, may in-

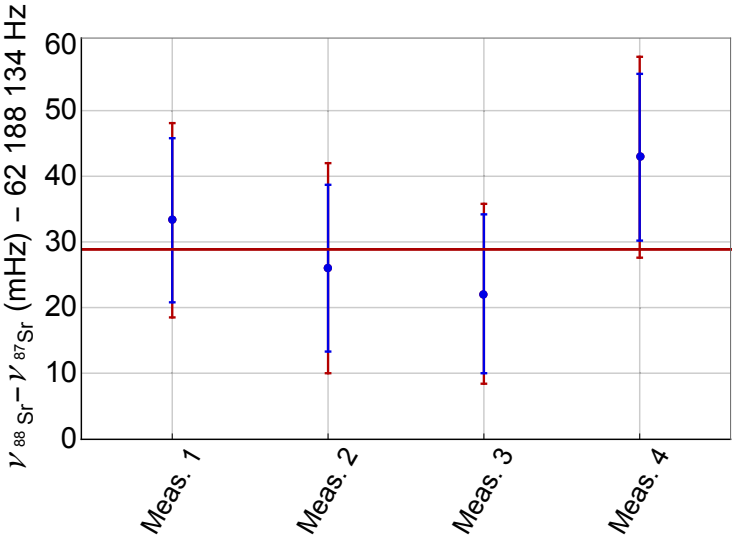

Figure 5.18: Measurements used for the evaluation of the isotope shift (September 2017). The red and blue error bars represent the statistical and systematic uncertainty.

troduce a rather large change in the value of the shifts (see Sections 4.3 and 4.4). For the isotope shift evaluation in June 2017 we used the average of two measurements. The isotope shift resulted $\nu_{88Sr} - \nu_{87Sr} = 62188134.006(15)$ Hz for the first measurement (June 2017) and $\nu_{88Sr} - \nu_{87Sr} = 62188134.029(12)$ Hz for the second one (September 2017).

In Figure 5.19 our results are compared with previously reported values. The red points are derived from absolute measurements of the ^{88}Sr frequency: in order to derive the isotope shift we used the value given by the *Bureau International des Poids et Mesures* (BIPM) for the ^{87}Sr frequency [101]. The green point was measured as interleaved measurement: ^{88}Sr and ^{87}Sr are interrogated alternatively in the same chamber and by sharing perturbations (i.e. with same probe beam power, bias magnetic field intensity, etc.): in this way, even though the uncertainty associated with the single isotope is of the order of 6×10^{-16}, the uncertainty on the isotope shift is much smaller (2×10^{-17}). Finally, the blue points corresponds to direct comparison between two independent systems operated one with ^{88}Sr and one with ^{87}Sr (as in our experiment). The offset of the value "Uni. Tokyo 2008", compared with others, was attributed a posteriori to the light shift due to the ASE of the TA laser used for the lattice [62]. Our first isotope shift measurement, using the TA for the lattice, is really close to the value given in [62], while the second measurement, with the TiSa laser for the lattice, results 1.6σ off (where σ is the combined uncertainty of the two measurements).

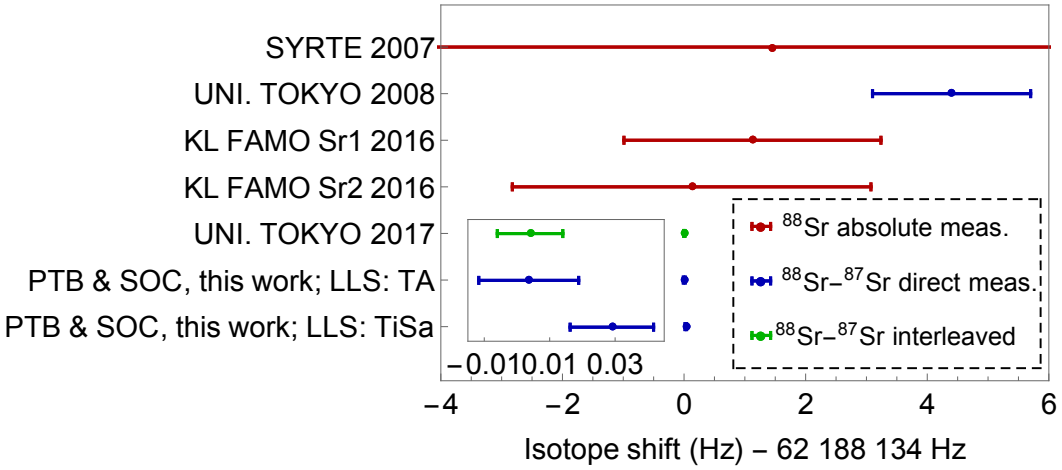

Figure 5.19: Isotope shift measurements compared with published values. "SYRTE 2007": [99]; "UNI. TOKYO 2008": [100]; "KL FAMO Sr1 2016" and "KL FAMO Sr2 2016": [63]; "UNI. TOKYO 2017": [62]. LLS: lattice laser system

Chapter 6

Conclusions and outlook

I have reported about my work on a transportable optical lattice clock, based on strontium atoms, developed in the framework of the I-SOC project. This work has been possible thanks to the collaboration between the Heinrich-Heine-Universität Düsseldorf, the University of Birmingham, where the atomic package was developed, and PTB (Braunschweig), where we performed an extensive characterization of the clock performances.

During this work I've investigated the clock operation using the strontium bosonic isotope: in particular, I've worked on the control of the shifts which characterize bosonic clocks. An intensity stabilization system for the clock laser beam was introduced, as well as a current stabilization system for the coils used to generate the bias magnetic field: this allowed to control the probe light shift and 2^{nd}-order Zeeman shift, respectively. We demonstrated a control of collisional effects in 1D lattice below the 1×10^{-17} relative level, and introduce a new approach for the evaluation of the shift, based on the lineshape analysis. Finally, we exploited the outstanding coherence time provided by a cryogenic silicon resonator, which allowed to operate at really low Rabi frequencies and, consequently, to reduce the coupling magnetic field strength and the probe light intensity. As result, Fourier limited clock transition linewidths of ~ 0.22 Hz were observed, these being one of the narrower optical transition ever reported.

The clock instability was measured against the PTB ^{87}Sr clock: the combined instability was $4.1 \times 10^{-16}/\sqrt{\tau}$, averaging down to the 3×10^{-18} level in less than 2×10^4 seconds. The clock accuracy was measured twice: once using the TA laser as lattice laser, with the inclusion of a grating based filter, and once using the TiSa laser. In the second case the uncertainty resulted 2.0×10^{-17} in fractional units. Both, the instability and the inaccuracy, represent a factor of approximately 30 improvement compared with previous works on bosonic optical lattice clocks. The ^{88}Sr $-^{87}$ Sr isotope shift was evaluated from the comparison with the PTB clock: in a first measurement (with the TA+filter for the lattice) the shift was found to be

in good agreement with the value recently reported by a group in Japan, within the 15 mHz uncertainty; while a second evaluation (with the TiSa, total uncertainty 12 mHz) resulted in an offset of less than 2σ.

Finally, we have characterized the performance of a newly developed grating based filter for the suppression of the TA ASE spectrum, by using the TiSa laser as reference: the comparison resulted in an agreement at 1×10^{-17} level, this opening new perspectives for applications of diode based lattice laser systems in high performance transportable clocks.

6.1 Outlook

One of the key ingredients for the enhancement of optical clocks performances, is the availability of better clock laser reference cavities, which not only allows for improved clock instability, but makes easier the investigation of systematic shifts. By further reducing the operating temperature of these cavities (e.g. from 124 K to 4 K [102, 103]) and using new mirror technologies (e.g. crystalline mirrors [104, 105]), their instability can be improved by one order of magnitude [78] within the next few years. Bosonic clocks will benefit most from this new development in cavity technologies: in fact, as demonstrated in this work, longer coherence times allow to operate with reduced coupling fields, simplifying the control of the induced shifts. This, together with a proper control of collisional effects, will allow in the future to achieve performances close to today best performing fermionic lattice clocks. A different approach consists in using Hyper-Ramsey spectroscopy [106]: this is a generalization of the Ramsey method [5] which allows, with a proper manipulation of the pulses duration, frequency and phase, to reduce by two to four orders of magnitude the shift induced by the interrogation laser. In this way, by properly balancing the clock wave and bias field intensities, both the shifts can be reduced to sub-10^{-17} level and would become controllable well below the 10^{-18} level.

This improvement in bosonic clocks, may also pave the way for new fundamental physics studies: for example, it was proposed that the measurement of isotope shifts can contribute to studies on the atomic Higgs force [107]. In particular in strontium, one could measure isotope shifts using all the bosonic isotopes (^{84}Sr, ^{86}Sr, ^{88}Sr and ^{90}Sr).

This work is also of great importance for the future of the I-SOC project. In fact we have demonstrated the compact size of the system, which is one of the most compact optical clock worldwide, not to be a limitation to the clock performance. Furthermore, we verified the robustness of the apparatus for transportation. Therefore, this system can be used as reference, in the framework of the I-SOC project, for the design of the flight instrument.

In the near future, we plan to move the clock out of the laboratory for measurement on the

field, such as relativistic geodesy or distant clock comparisons. Once it will be operated with ^{87}Sr, we expect to be able to achieve an accuracy below the 10^{-17} level: thus, for example, measurements of the local terrestrial gravitational potential at the equivalent uncertainty level better than 10 cm will be possible.

References

[1] BIPM. *The international System of Units (SI)*, 8th edition edition, 2006.

[2] L. Essen and J. V. L. Parry. The caesium frequency standard. *NPL News*, 1955.

[3] F. Levi, C. Calosso, D. Calonico, L. Lorini, E. Bertacco, A. Godone, G. Costanzo, B. Mongino, S. Jefferts, T. Heavner, and E. Donley. Cryogenic fountain development at NIST and INRIM: preliminary characterization," IEEE trans. ultrason., ferroelect., freq. cont., 57, pp. 600–605 (2010). *IEEE Trans. Ultrason., Ferroelect., Freq. Cont.*, 57:600, 2010.

[4] A. Clairon, C. Salomon, S. Guellati, and W. D. Phillips. Ramsey resonance in a Zacharias fountain. *EPL (Europhysics Letters)*, 16(2):165, 1991.

[5] N. F. Ramsey. A molecular beam resonance method with separated oscillating fields. *Phys. Rev.*, 78:695–699, 1950.

[6] B. C. Young, F. C. Cruz, W. M. Itano, and J. C. Bergquist. Visible lasers with subhertz linewidths. *Phys. Rev. Lett.*, 82:3799–3802, May 1999.

[7] R. W. P. Drever, J. L. Hall, F. V. Kowalski, J. Hough, G. M. Ford, A. J. Munley, and H. Ward. Laser phase and frequency stabilization using an optical resonator. *Appl. Phys. B*, 31:97, 1983.

[8] Th. Udem, J. Reichert, R. Holzwarth, and T. W. Hänsch. Accurate measurement of large optical frequency differences with a mode-locked laser. *Opt. Lett.*, 24(13):881–883, 1999.

[9] A. P. Kulosa, D. Fim, K. H. Zipfel, S. Rühmann, S. Sauer, N. Jha, K. Gibble, W. Ertmer, E. M. Rasel, M. S. Safronova, U. I. Safronova, and S. G. Porsev. Towards a Mg lattice clock: Observation of the ${}^1S_0 - {}^3P_0$ transition and determination of the magic wavelength. *Phys. Rev. Lett.*, 115:240801, Dec 2015.

[10] R. Le Targat, L. Lorini, Y. Le Coq, M. Zawada, J. Guna, M. Abgrall, M. Gurov, P. Rosenbusch, D. G. Rovera, B. Nagrny, R. Gartman, P.G. Westergaard, M.E. Tobar, M. Lours, G. Santarelli, A. Clairon, S. Bize, P. Laurent, P. Lemonde, and J. Lodewyck. Experimental realization of an optical second with strontium lattice clocks. *Nature Comm.*, 4:2109, 2013.

[11] S. Falke, N. Lemke, C. Grebing, B. Lipphardt, S. Weyers, V. Gerginov, N. Huntemann, C. Hagemann, A. Al-Masoudi, S. Häfner, St. Vogt, U. Sterr, and Ch. Lisdat. A strontium lattice clock with 3×10^{-17} inaccuracy and its frequency. *New J. Phys*, 16(073023), 2014.

[12] T.L. Nicholson, S.L. Campbell, R.B. Hutson, G.E. Marti, B.J. Bloom, R.L. McNally, W. Zhang, M.D. Barrett, M.S. Safronova, W.L. Strouse, G.F. Tew, and J. Ye. Systematic evaluation of an atomic clock at 2×10^{-18} total uncertainty. *Nat. Comm.*, 6:6896, 2015.

[13] I. Ushijima, M. Takamoto, M. Das, T. Ohkubo, and H. Katori. Cryogenic optical lattice clocks. *Nat. Photonics*, 9:185–189, 2015.

[14] I. R. Hill, R. Hobson, W. Bowden, E. M. Bridge, S. Donnellan, Curtis E. A., and P. Gill. A low maintenance Sr optical lattice clock. *Journal of Physics: Conference Series*, 723(012019), 2016.

[15] J. J. McFerran, L. Yi, S. Mejri, S. Di Manno, W. Zhang, J. Guéna, Y. Le Coq, and S. Bize. Neutral atom frequency reference in the deep ultraviolet with fractional uncertainty $= 5.7 \times 10^{-15}$. *Phys. Rev. Lett.*, 108:183004, May 2012.

[16] N. Poli, Z. W. Barber, N. D. Lemke, C. W. Oates, L. S. Ma, J. E. Stalnaker, T. M. Fortier, S. A. Diddams, L. Hollberg, J. C. Bergquist, A. Brusch, S. Jefferts, T. Heavner, and T. Parker. Frequency evaluation of the doubly forbidden $^1S_0$–$^3P_0$ transition in bosonic ^{174}Yb. , 77(5):050501, 2008.

[17] M. Yasuda, H. Inaba, T. Kohno, T. Tanabe, Y. Nakajima, K. Hosaka, D. Akamatsu, A. Onae, T. Suzuyama, M. Amemiya, and F. L. Hong. Improved absolute frequency measurement of the ^{171}Yb optical lattice clock towards a candidate for the redefinition of the second. *Applied Physics Express*, 5(10):102401, 2012.

[18] C. Y. Park, D. H. Yu, W. K. Lee, S. E. Park, E. B. Kim, S. K. Lee, J. W. Cho, T. H. Yoon, J. Mun, S. J. Park, T. Y. Kwon, and S. B. Lee. Absolute frequency measurement of $^1S_0$ (F = 1/2)– $^3P_0$ (F = 1/2) transition of ^{171}Yb atoms in a one-dimensional optical lattice at KRISS. *Metrologia*, 50(2):119, 2013.

[19] M. Pizzocaro, P. Thoumany, B. Rauf, F. Bregolin, G. Milani, C. Clivati, G. A. Costanzo, F. Levi, and D. Calonico. Absolute frequency measurement of the $^1S_0$–$^3P_0$ transition of ^{171}Yb. *Metrologia*, 54(1):102, 2017.

[20] H. Katori, M. Takamoto, V. G. Pal'chikov, and V. D. Ovsiannikov. Ultrastable optical clock with neutral atoms in an engineered light shift trap. *Phys. Rev. Lett.*, 91:173005, 2003.

[21] T. L. Nicholson, M. J. Martin, J. R. Williams, B. J. Bloom, M. Bishof, M. D. Swallows, S. L. Campbell, and J. Ye. Comparison of two independent Sr optical clocks with 1×10^{-17} stability at 10^3 s. *Phys. Rev. Lett.*, 109:230801, 2012.

[22] N. Hinkley, J. A. Sherman, N. B. Phillips, M. Schioppo, N. D. Lemke, K. Beloy, M. Pizzocaro, C. W. Oates, and A. D. Ludlow. An atomic clock with 10^{-18} instability. *Science*, 341(6151):1215–1218, 2013.

[23] A. Al-Masoudi, S. Dörscher, S. Häfner, U. Sterr, and Ch. Lisdat. Noise and instability of an optical lattice clock. *Phys. Rev. A*, 92:063814, 2015.

[24] M. Schioppo, R. C. Brown, W. F. McGrew, N. Hinkley, R. J. Fasano, K. Beloy, T. H. Yoon, G. Milani, D. Nicolodi, J. A. Sherman, N. B. Phillips, C. W. Oates, and A. D. Ludlow. Ultrastable optical clock with two cold-atom ensembles. *Nat. Photonics*, 11:48–52, 2017.

[25] W. F. McGrew, X. Zhang, R. J. Fasano, S. A. Schäffer, K. Beloy, D. Nicolodi, R. C. Brown, N. Hinkley, G. Milani, M. Schioppo, T. H. Yoon, and A. D. Ludlow. Atomic clock performance beyond the geodetic limit. *arXiv:1807.11282*, 2018.

[26] N. Huntemann, C. Sanner, B. Lipphardt, Chr. Tamm, and E. Peik. Single-Ion Atomic Clock with 3×10^{-18} Systematic Uncertainty. *Phys. Rev. Lett.*, 116(6):063001, February 2016.

[27] "Report of the 104^{th} Meeting of the Comité International des Poids et Mesures (CIPM)", Bureau International des Poids et Mesures (BIPM), Sevres, Paris, Cedex 2015.

[28] Ch. Lisdat, G. Grosche, N. Quintin, C. Shi, S.M.F. Raupach, C. Grebing, D. Nicolodi, F. Stefani, A. Al-Masoudi, S. Dörscher, S. Häfner, J.-L. Robyr, N. Chiodo, S. Bilicki, E. Bookjans, A. Koczwara, S. Koke, A. Kuhl, F. Wiotte, F. Meynadier, E. Camisard, M. Abgrall, M. Lours, T. Legero, H. Schnatz, U. Sterr, H. Denker, C. Chardonnet,

Y. Le Coq, G. Santarelli, A. Amy-Klein, R. Le Targat, J. Lodewyck, O. Lopez, and P.-E. Pottie. A clock network for geodesy and fundamental science. *Nat. Comm.*, 7:12443, 2016.

[29] H. Schnatz, L. J. Terra, K. Predehl, T. Feldmann, T. Legero, B. Lipphardt, U. Sterr, G. Grosche, R. Holzwarth, T. W. Hansch, T. Udem, Z. H. Lu, L. J. Wang, W. Ertmer, J. Friebe, A. Pape, E. M. Rasel, M. Riedmann, and T. Wubbena. Phase-coherent frequency comparison of optical clocks using a telecommunication fiber link. *IEEE Transactions on Ultrasonics, Ferroelectrics, and Frequency Control*, 57:175–181, 2010.

[30] F. Levi, D. Calonico, A. Mura, M. Frittelli, C. E. Calosso, M. Zucco, C. Clivati, G. A. Costanzo, R. Ambrosini, G. Galzerano, P. De Natale, D. Mazzotti, N. Poli, D. V. Sutyrin, and G. M. Tino. Lift-the italian link for time and frequency. *2013 Joint European Frequency and Time Forum International Frequency Control Symposium (EFTF/IFC)*, (477-480), 2013.

[31] A. Bercy, O. Lopez, P. E. Pottie, and A. Amy-Klein. Ultrastable optical frequency dissemination on a multi-access fibre network. *Applied Physics B*, 122(7):189, Jun 2016.

[32] A. D. Ludlow, M. M. Boyd, J. Ye, E. Peik, and P. O. Schmidt. Optical atomic clocks. *Rev. Mod. Phys.*, 87:637–701, 2015.

[33] M. Vermeer. *Chronometric levelling*, volume 83. Helsinki: Geodeettinen Laitos, Geodetiska Institutet, 1983.

[34] C. Voigt, H. Denker, and L. Timmen. Time-variable gravity potential components for optical clock comparisons and the definition of international time scales. *Metrologia*, 53(6):1365, 2016.

[35] S. B. Koller, J. Grotti, St. Vogt, A. Al-Masoudi, S. Dörscher, S. Häfner, U. Sterr, and Ch. Lisdat. Transportable optical lattice clock with 7×10^{-17} uncertainty. *Phys. Rev. Lett.*, 118:073601, 2017.

[36] J. Grotti, S. Koller, S. Vogt, S. Häfner, U. Sterr, Ch. Lisdat, H. Denker, C. Voigt, L. Timmen, A. Rolland, F. N. Baynes, H. S. Margolis, M. Zampaolo, P. Thoumany, M. Pizzocaro, B. Rauf, F. Bregolin, A. Tampellini, P. Barbieri, M. Zucco, G. A. Costanzo, C. Clivati, F. Levi, and D. Calonico. Geodesy and metrology with a transportable optical clock. *Nature Physics*, 14:437–441, 2018.

[37] Private communication.

[38] T. Takano, M. Takamoto, I. Ushijima, N. Ohmae, T. Akatsuka, A. Yamaguchi, Y. Kuroishi, H. Munekane, B. Miyahara, and H. Katori. Geopotential measurements with synchronously linked optical lattice clocks. *Nat. Photonics*, 10:662–666, 2016.

[39] P. Laurent, D. Massonnet, L. Cacciapuoti, and C. Salomon. The ACES/PHARAO space mission. *Comptes Rendus Physique*, 16:540 – 552, 2015.

[40] B. Hoffmann. Noon-Midnight Red Shift. *Physical Review*, 121(1):337–342, 1961.

[41] T. P. Krisher. Gravitational redshift in a local freely falling frame: A proposed new null test of the equivalence principle. *Physical Review D*, 53(4):R1735–R1739, 1996.

[42] K. Bongs, Y. Singh, L. Smith, W. He, O. Kock, D. Świerad, J. Hughes, S. Schiller, S. Alighanbari, S. Origlia, S. Vogt, U. Sterr, Ch. Lisdat, R. Le Targat, J. Lodewyck, D. Holleville, B. Venon, S. Bize, G. P. Barwood, P. Gill, I. R. Hill, Y. B. Ovchinnikov, N. Poli, G. M. Tino, J. Stuhler, and W. Kaenders. Development of a strontium optical lattice clock for the SOC mission on the ISS. *C. R. Phys.*, 16(5):553 – 564, 2015.

[43] A. Derevianko and M. Pospelov. Hunting for topological dark matter with atomic clocks. *Nature Physics*, 10:933, 2014.

[44] J. D. Prestage, R. L. Tjoelker, and L. Maleki. Atomic clocks and variations of the fine structure constant. *Phys. Rev. Lett.*, 74:3511, 1995.

[45] S. Schiller, A. Görlitz, A. Nevsky, S. Alighanbari, S. Vasilyev, C. Abou-Jaoudeh, G. Mura, T. Franzen, U. Sterr, S. Falke, Ch. Lisdat, E. Rasel, A. Kulosa, S. Bize, J. Lodewyck, G. M. Tino, N. Poli, M. Schioppo, K. Bongs, Y. Singh, P. Gill, G. Barwood, Y. Ovchinnikov, J. Stuhler, W. Kaenders, C. Braxmaier, R. Holzwarth, A. Donati, S. Lecomte, D. Calonico, F. Levi, and members of the SOC2 teams. Towards neutral-atom space optical clocks (SOC2): Development of high-performance transportable and breadboard optical clocks and advanced subsystems. *Let's embrace space II*, Ch. 45, 452–463, 2012.

[46] N. Poli, M. Schioppo, S. Vogt, St. Falke, U. Sterr, Ch. Lisdat, and G. M. Tino. A transportable strontium optical lattice clock. *Appl. Phys. B*, 117:1107 – 1116, 2014.

[47] M. Schioppo. *Development of a transportable strontium optical clock*. PhD thesis, Università degli Studi di Firenze, 2010.

[48] G. Mura, T. Franzen, C. A. Jaoudeh, A. Görlitz, H. Luckmann, I. Ernsting, A. Nevsky, and S. Schiller. A transportable optical lattice clock using ^{171}Yb. In *2013 Joint*

European Frequency and Time Forum International Frequency Control Symposium (EFTF/IFC), pages 376–378, 2013.

[49] NIST. Basic atomic spectroscopy data for strontium, 2016.

[50] M. M. Boyd, T. Zelevinsky, A. D. Ludlow, S. Blatt, T. Zanon-Willette, S. M. Foreman, and J. Ye. Nuclear spin effects in optical lattice clocks. *Phys. Rev. A*, 76:022510, 2007.

[51] A. V. Taichenachev, V. I. Yudin, C. W. Oates, C. W. Hoyt, Z. W. Barber, and L. Hollberg. Magnetic field-induced spectroscopy of forbidden optical transitions with application to lattice-based optical atomic clocks. *Phys. Rev. Lett.*, 96:083001, 2006.

[52] H. J. Metcalf and P. Van der Straten. *Laser Cooling And Trapping*. Springer, New York, 1999.

[53] L. Smith. *A transportable strontium optical lattice clock towards space*. PhD thesis, University of Birmingham, December 2016.

[54] S. Origlia, S. Schiller, M.S. Pramod, L. Smith, Y. Singh, W. He, S. Viswam, D. Świerad, J. Hughes, K. Bongs, U. Sterr, Ch. Lisdat, S. Vogt, S. Bize, J. Lodewyck, R. Le Targat, D. Holleville, B. Venon, P. Gill, G. Barwood, I. R. Hill, Y. Ovchinnikov, A. Kulosa, W. Ertmer, E. M. Rasel, J. Stuhler, and W. Kaenders. Development of a strontium optical lattice clock for the SOC mission on the ISS. *Proc. SPIE 9900, Quantum Optics, 990003*, 2016.

[55] R. H. Dicke. The effect of collisions upon the Doppler width of spectral lines. *Phys. Rev.*, 89(2):472–473, 1953.

[56] S. Blatt, J. W. Thomsen, G. K. Campbell, A. D. Ludlow, M. D. Swallows, M. J. Martin, M. M. Boyd, and J. Ye. Rabi spectroscopy and excitation inhomogeneity in a one-dimensional optical lattice clock. *Phys. Rev. A*, 80:052703, Nov 2009.

[57] A. D. Ludlow. *The Strontium Optical Lattice Clock: Optical Spectroscopy with Sub-Hertz Accuracy*. PhD thesis, B.S. Physics, Brigham Young University, 2002.

[58] R. Santra, E. Arimondo, T. Ido, C. H. Greene, and J. Ye. High-accuracy optical clock via three-level coherence in neutral bosonic ^{88}Sr. *Phys. Rev. Lett.*, 94:173002, May 2005.

[59] Tao Hong, Claire Cramer, Warren Nagourney, and E. N. Fortson. Optical clocks based on ultranarrow three-photon resonances in alkaline earth atoms. *Phys. Rev. Lett.*, 94:050801, Feb 2005.

[60] R. Tyumenev, M. Favier, S. Bilicki, E. Bookjans, R. Le Targat, J. Lodewyck, D. Nicolodi, Y. Le Coq, M. Abgrall, J. Guéna, L. De Sarlo, and S. Bize. Comparing a mercury optical lattice clock with microwave and optical frequency standards. *New J. Phys.*, 18(11):113002, 2016.

[61] J. Lodewyck, S. Bilicki, E. Bookjans, J. L. Robyr, C. Shi, G. Vallet, R. Le Targat, D. Nicolodi, Y. Le Coq, and J. Guéna. Optical to microwave clock frequency ratios with a nearly continuous strontium optical lattice clock. *Metrologia*, 53:1123, 2016.

[62] T. Takano, R. Mizushima, and H. Katori. Precise determination of the isotope shift of ^{88}Sr–^{87}Sr optical lattice clock by sharing perturbations. *Appl. Phys. Express*, 10:072801, 2017.

[63] C. Radzewicz, M. Bober, P. Morzyński, A. Cygan, D. Lisak, D. Bartoszek-Bober, P. Masłowski, P. Ablewski, J. Zachorowski, W. Ciuryło R. Gawlik, and M. Zawada. Accuracy budget of the ^{88}Sr optical atomic clocks at KL FAMO. *Physica Scripta*, 91:084003, 2016.

[64] M. Inguscio and L. Fallani. *Atomic Physics: Precise Measurements and Ultracold Matter*. Oxford University Press, 2013.

[65] D. M. Harber, H. J. Lewandowski, J. M. McGuirk, and E. A. Cornell. Effect of cold collisions on spin coherence and resonance shifts in a magnetically trapped ultracold gas. *Phys. Rev. A*, 66:053616, Nov 2002.

[66] G. K. Campbell, M. M. Boyd, J. W. Thomsen, M. J. Martin, S. Blatt, M. D. Swallows, T. L. Nicholson, T. Fortier, C. W. Oates, S. A. Diddams, N. D. Lemke, P. Naidon, P. Julienne, Jun Ye, and A. D. Ludlow. Probing interactions between ultracold fermions. *Science*, 324(5925):360–363, 2009.

[67] Ch. Lisdat, J. S. R. Vellore Winfred, T. Middelmann, F. Riehle, and U. Sterr. Collisional losses, decoherence, and frequency shifts in optical lattice clocks with bosons. *Phys. Rev. Lett.*, 103:090801, 2009.

[68] J. S. R. Vellore Winfred. *Investigation of collisional losses and decoherence in a 1-D optical lattice clock with ^{88}Sr*. PhD thesis, Leibniz Universität Hannover, 2010.

[69] T. Akatsuka, M. Takamoto, and Katori H. Three-dimensional optical lattice clock with bosonic ^{88}Sr atoms. *Physical Review A*, 81:023402, 2010.

[70] T. Zelevinsky, M. M. Boyd, A. D. Ludlow, T. Ido, J. Ye, R. Ciuryło, P. Naidon, and Julienne P. S. Narrow line photoassociation in an optical lattice. *Phys. Rev. Lett.*, 96:203201, 2006.

[71] A. Yu. Nevsky, S. Alighanbari, Q. Chen, I. Ernsting, S. Vasilyev, S. Schiller, G. Barwood, P. Gill, N. Poli, and G. M. Tino. Robust frequency stabilization of multiple spectroscopy lasers with large and tunable offset frequencies. *Opt. Lett.*, 38:4903–6, 2013.

[72] S. Falke, M. Misera, U. Sterr, and Ch. Lisdat. Delivering pulsed and phase stable light to atoms of an optical clock. *Appl. Phys. B*, 107:301–311, 2012.

[73] J. I. Thorpe, K. Numata, and J. Livas. Laser frequency stabilization and control through offset sideband locking to optical cavities. *Opt. Express*, 16(20):15980–15990, Sep 2008.

[74] Eric D. Black. An introduction to Pound–Drever–Hall laser frequency stabilization. *American Journal of Physics*, 69(1):79–87, 2001.

[75] D. Świerad, S. Häfner, S. Vogt, B. Venon, D. Holleville, S. Bize, A. Kulosa, S. Bode, Y. Singh, K. Bongs, E. M. Rasel, J. Lodewyck, R. Le Targat, Ch. Lisdat, and U. Sterr. Ultra-stable clock laser system development towards space applications. *Sci. Rep.*, 6:33973, 09 2016.

[76] S. Vogt, C. Lisdat, T. Legero, U. Sterr, I. Ernsting, A. Nevsky, and S. Schiller. Demonstration of a transportable 1 Hz-linewidth laser. *Appl. Phys. B*, 104:741, 2011.

[77] S. Häfner, S. Falke, C. Grebing, S. Vogt, T. Legero, M. Merimaa, Ch. Lisdat, and U. Sterr. 8×10^{17} fractional laser frequency instability with a long room-temperature cavity. *Opt. Lett.*, 40(9):2112–2115, 2015.

[78] D. G. Matei, T. Legero, S. Häfner, C. Grebing, R. Weyrich, W. Zhang, L. Sonderhouse, J. M. Robinson, J. Ye, F. Riehle, and U. Sterr. 1.5 μm lasers with sub-10 mHz linewidth. *Phys. Rev. Lett.*, 118:263202, 2017.

[79] J. Stenger, H. Schnatz, C. Tamm, and H.R. Telle. Ultraprecise measurement of optical frequency ratios. *Phys. Rev. Lett.*, 88:073601, 2002.

[80] M. Schioppo, N. Poli, M. Prevedelli, St. Falke, Ch. Lisdat, U. Sterr, and G. M. Tino. A compact and efficient strontium oven for laser-cooling experiments. *Rev. Sci. Instrum.*, 83(10):103101, 2012.

[81] I. R. Hill, Yuri B. Ovchinnikov, E. M. Bridge, E. A. Curtis, and P. Gill. Zeeman slowers for strontium based on permanent magnets. *J. Phys. B*, 47:75006, 2014.

[82] G. J. Dick. Local oscillator induced instabilities in trapped ion frequency standards. In *Proceedings of* 19^{th} *Annu. Precise Time and Time Interval Meeting, Redendo Beach, 1987*, pages 133–147, Washington, DC, 1988. U.S. Naval Observatory.

[83] D. B. Hume and D. R. Leibrandt. Probing beyond the laser coherence time in optical clock comparisons. *Phys. Rev. A*, 93:032138, Mar 2016.

[84] L. Hollberg, C. W. Oates, E. A. Curtis, E. N. Ivanov, S. A. Diddams, T. Udem, H. G. Robinson, J. C. Bergquist, R. J. Rafac, W. M. Itano, R. E. Drullinger, and D. J. Wineland. Optical frequency standards and measurements. *IEEE Journal of Quantum Electronics*, 37(12):1502–1513, Dec 2001.

[85] P. Lemonde and P. Wolf. Optical lattice clock with atoms confined in a shallow trap. *Phys. Rev. A*, 72:033409, 2005.

[86] D. W. Allan. Should the classical variance be used as a basic measure in standard metrology? *IEEE Trans. Instr. Meas.,*, IM-36:646, 1987.

[87] Thomas Middelmann, Stephan Falke, Christian Lisdat, and Uwe Sterr. High accuracy correction of blackbody radiation shift in an optical lattice clock. *Phys. Rev. Lett.*, 109:263004, 2012.

[88] T. Middelmann, S. Falke, Ch. Lisdat, and U. Sterr. Long-range transport of ultracold atoms in a far-detuned one-dimensional optical lattice. *New Journal of Physics*, 14(7):073020, 2012.

[89] GUM, Guide to the Expression of Uncertainty in Measurement, ISO/TAG 4. (ISO, 1993) (corrected and reprinted, 1995) in the name of the BIPM, IEC, IFCC, ISO, UPAC, IUPAP, and OILM (Sèrres, France, 1995), ISBN 92-67-10188-9,1995.

[90] M. Naftaly and R. E. Miles. Terahertz time-domain spectroscopy for material characterization. *Proceedings of the IEEE*, 95(8):1658–1665, 2007.

[91] Michael N. Bishof. *Understanding atomic interactions in an optical lattice clock and using them to study many-body physics*. PhD thesis, University of Colorado, 2014.

[92] P. G. Westergaard, J. Lodewyck, L. Lorini, A. Lecallier, E. A. Burt, M. Zawada, J. Millo, and P. Lemonde. Lattice-induced frequency shifts in Sr optical lattice clocks at the 10^{-17} level. *Phys. Rev. Lett.*, 106:210801, May 2011.

[93] A. V. Taichenachev, V. I. Yudin, V. D. Ovsiannikov, V. G. Pal'chikov, and C. W. Oates. Frequency shifts in an optical lattice clock due to magnetic-dipole and electric-quadrupole transitions. *Phys. Rev. Lett.*, 101:193601, Nov 2008.

[94] B. J. Bloom, T. L. Nicholson, J. R. Williams, S. L. Campbell, M. Bishof, X. Zhang, W. Zhang, S. L. Bromley, and J. Ye. An optical lattice clock with accuracy and stability at the 10^{-18} level. *Nature*, 506(7486):71–75, 2014.

[95] H. Katori, V. D. Ovsiannikov, S. I. Marmo, and V. G. Palchikov. Strategies for reducing the light shift in atomic clocks. *Phys. Rev. A*, 91:052503, 2015.

[96] J. Lodewyck, M. Zawada, L. Lorini, M. Gurov, and P. Lemonde. Observation and cancellation of a perturbing dc stark shift in strontium optical lattice clocks. *IEEE Trans. Ultrasonics Ferroelectr. Freq. Control*, 59:411–415, 2012.

[97] K. Gibble. Scattering of cold atom coherences by hot atoms: Background gas collision shifts of primary fountain clocks. In *2013 Joint European Frequency and Time Forum International Frequency Control Symposium (EFTF/IFC)*, pages 46–47, July 2013.

[98] S. Falke, H. Schnatz, J. S. R. Vellore Winfred, T. Middelmann, S. Vogt, S. Weyers, B. Lipphardt, G. Grosche, F. Riehle, U. Sterr, and Ch. Lisdat. The ^{87}Sr optical frequency standard at PTB. *Metrologia*, 48(5):399, 2011.

[99] X. Baillard, M. Fouché, R. Le Targat, P. G. Westergaard, A. Lecallier, Y. Le Coq, G. D. Rovera, S. Bize, and P. Lemonde. Accuracy evaluation of an optical lattice clock with bosonic atoms. *Opt. Lett.*, 32(13):1812–1814, 2007.

[100] T. Akatsuka, M. Takamoto, and H. Katori. Optical lattice clocks with non-interacting bosons and fermions. *Nature Physics*, 4:954, 2008.

[101] Recommendation 2 (ci-2015) 2015 *Session II of the 104th Meeting of the CIPM* (www.bipm.org/utils/en/pdf/CIPM/CIPM2015-II-EN.pdf), 2015.

[102] E. Wiens, A. Yu. Nevsky, and S. Schiller. Resonator with ultrahigh length stability as a probe for equivalence-principle-violating physics. *Phys. Rev. Lett.*, 117:271102, 2016.

[103] W. Zhang, J. M. Robinson, L. Sonderhouse, E. Oelker, C. Benko, J. L. Hall, T. Legero, D. G. Matei, F. Riehle, U. Sterr, and J. Ye. Ultrastable Silicon Cavity in a Continuously Operating Closed-Cycle Cryostat at 4 K. *Physical Review Letters*, 119(24):243601, 2017.

[104] G. D. Cole, W. Zhang, M. J. Martin, J. Ye, and M. Aspelmeyer. Tenfold reduction of brownian noise in high-reflectivity optical coatings. *Nature Photonics*, 7(644), 2013.

[105] G. D. Cole, W. Zhang, B. J. Bjork, D. Follman, P. Heu, C. Deutsch, L. Sonderhouse, J. Robinson, C. Franz, A. Alexandrovski, M. Notcutt, O. H. Heckl, J. Ye, and M. Aspelmeyer. High-performance near- and mid-infrared crystalline coatings. *Optica*, 3(6):647–656, 2016.

[106] V. I. Yudin, A. V. Taichenachev, C. W. Oates, Z. W. Barber, N. D. Lemke, A. D. Ludlow, U. Sterr, Ch. Lisdat, and F. Riehle. Hyper-ramsey spectroscopy of optical clock transitions. *Phys. Rev. A*, 82:011804(R), 2010.

[107] C. Delaunay, R. Ozeri, G. Perez, and Y. Soreq. Probing atomic Higgs-like forces at the precision frontier. *Phys. Rev. D*, 96:093001, 2017.

[108] T. L. Nicholson. *A new record in atomic clock performance*. PhD thesis, University of Colorado, 2015.

Appendix A

Compact blue distribution breadboard

The new distribution breadboard for the blue laser (whose photo is shown in Figure 3.2a), was developed to be as compact as possible, using commercially available components. The scheme of the design is shown in Figure A.1. All the optics are 1/2" size. The use of the double pass AOM for the MOT beams allows to use the same beams for detection: this is useful if, as in our case, the optical access to the main vacuum chamber is limited and it would be difficult to introduce a dedicated detection beam. Furthermore, this allows to save electrical power, since no additional AOM is needed for the detection beam. The compact size of the breadboard is helpful also for the mechanical stability of the optical system (e.g. fiber coupling). In the future, we plan to implement a cooling breadboard, underneath the optical breadboard, for operation outside the lab: this is the reason why all the optics, including the fiber collimators, are placed inside the box (while in the other breadboards fiber coupled fixed to the front panel of the breadboard's enclosure are used). The total efficiency of the breadboard (i.e. from input to the output of the slower and MOT beams fiber) is about 30%.

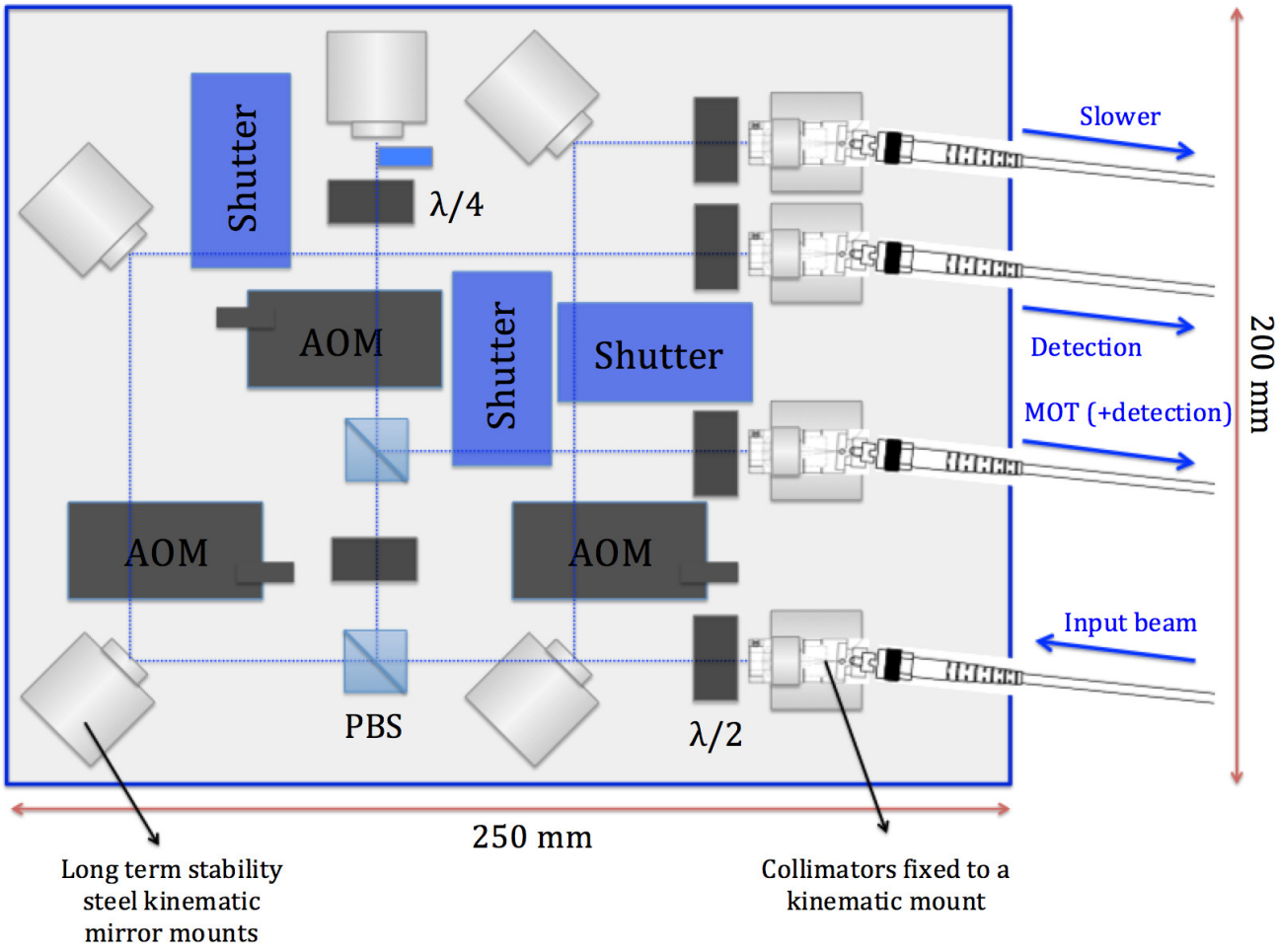

Figure A.1: Schematic of the design of the new distribution breadboard for the blue laser.

Appendix B

Calibration of temperature sensors

The temperature sensors used for the main vacuum chamber are thin film RTDs (PT100) from Omega. These were chosen due to the small size, and to the fact that thin film RTDs are known to be robust and stable over time [108]: this is important since, once the sensors are placed on the chamber, it will be impossible to recalibrate them again. However they come as class A sensors, meaning that the original accuracy is 0.19 °C (at 20 °C): thus a calibration is needed. We used a calibration setup at PTB, including a reference sensor with 1 mK absolute accuracy connected to a thermometer from Fluke (model 1594A). Four sensors can be calibrated at the same time.

The relation between the resistance R of the PT100s, which is what is measured by the acquisition device, and the temperature T (in degree Celsius) can be expressed as:

$$T = R_0(1 + \alpha R + \beta R^2), \tag{B.1}$$

where R_0 (resistance at 0 °C), α and β are the coefficients to be evaluated with the calibration. The introduction of a second order term provides a more accurate fit of the experimental data. For the calibration five points are used, between 17 and 30 °C (see Figure B.1).

In order to test the robustness and reliability of the sensors the following procedure was applied. The sensors were calibrated once, then they were subjected to a thermal stress test, down to -70 °C (the minimum specified temperature), using liquid nitrogen, and to some mechanical stress test; after that the calibration was repeated and compared with the first calibration. The difference between the two calibrations is evaluated at the five temperatures used as reference: the same procedure was repeated for 20 sensors. The result is reported in the histogram in Figure B.2: the resulting standard deviation is $\sigma \sim 8$ mK. It's practical to use the same uncertainty for all the sensors: we decided to use twice the standard deviation, meaning 16 mK, as "safe" value.

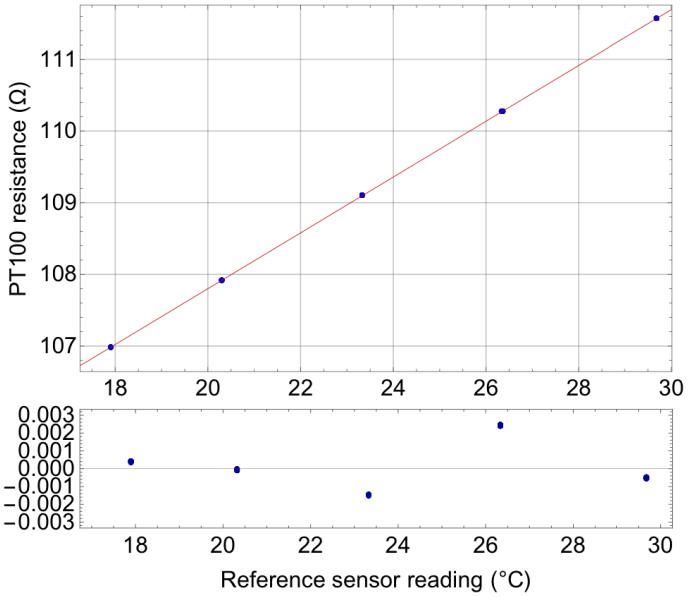

Figure B.1: Example of measurement for the calibration of the temperature sensors (with residuals).

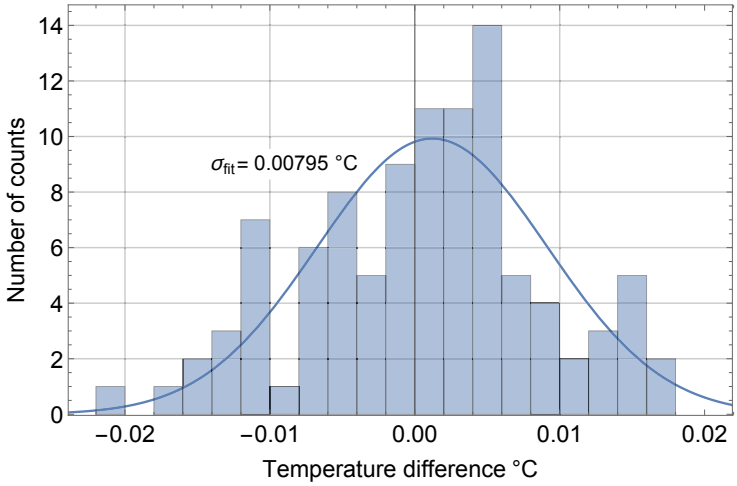

Figure B.2: Temperature difference between two calibrations (before and after stress tests) for 20 temperature sensors, evaluated at 5 different temperatures between 17 and 30 °C.

Appendix C

Temperature control system

In order to control the temperature gradients across the main vacuum chamber, a temperature control system was designed (Figure C.1). The only source of heat close to the chamber are the MOT coils: these are mounted on a system made by two copper plates, divided by a thermal insulator sheet. The internal cooling plates are less than 1 mm away from the vacuum chamber. On the external side the coils are in contact with the telescopes holders (made of aluminum). In order to reduce as much as possible the temperature gradients across the vacuum chamber, the temperature of the internal cooling plates (including the section of the plates inside the coils) shall be kept as close as possible to room temperature. This is done using eight TEC (or Peltier) elements: four of them are placed in between the internal and the external cooling plates, and four are placed on the telescope holders. To each TEC element is associated a 10k thermistor, placed on the inner side of the internal cooling plate (see Figure C.1). The heat is dissipated using eight heat pipes, connected to a heat sink on the top of the atomic package rack. The heat pipes are connected to the external copper plates and to the telescopes holders with custom made adaptors. Also the control electronics was designed to be compact and power efficient. The eight controllers (from Analog Technologies, model TEC-A1-5V-5V-D), one per each TEC element, are implemented in a single PCB board (Figure C.2). Via I^2C interface, an Arduino Nano board drives a DAC, used for controlling the set point of the controllers, and a ADC, for the acquisition of the thermistors reading.

The system was tested before fixing the coils to the chamber, and the temperature homogeneity of the internal cooling plate was found to be better than 300 mK, with a power consumption of about 5 W (by running the coils as in standard clock operation, i.e. power dissipated 7 W). However, after the implementation of the temperature sensors on the vacuum chamber, it was found that the temperature homogeneity of the chamber was good enough considering the actual clock accuracy (i.e. $\sim$ 350 mK), and the temperature control system was not used during measurement.

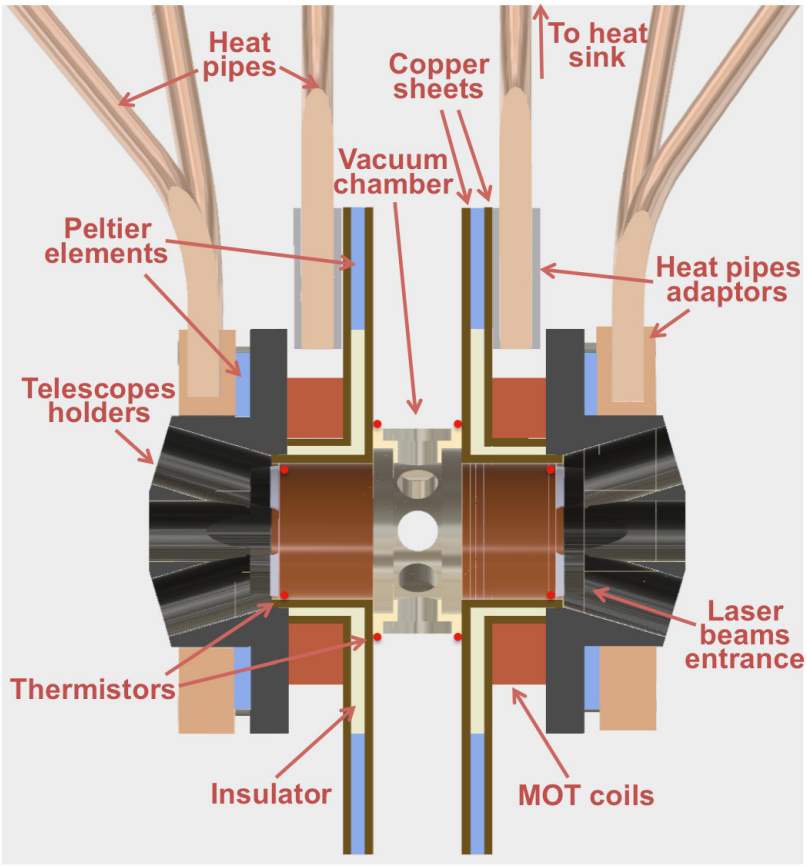

Figure C.1: Scheme of the temperature control system for the main vacuum chamber. See text for a detailed description.

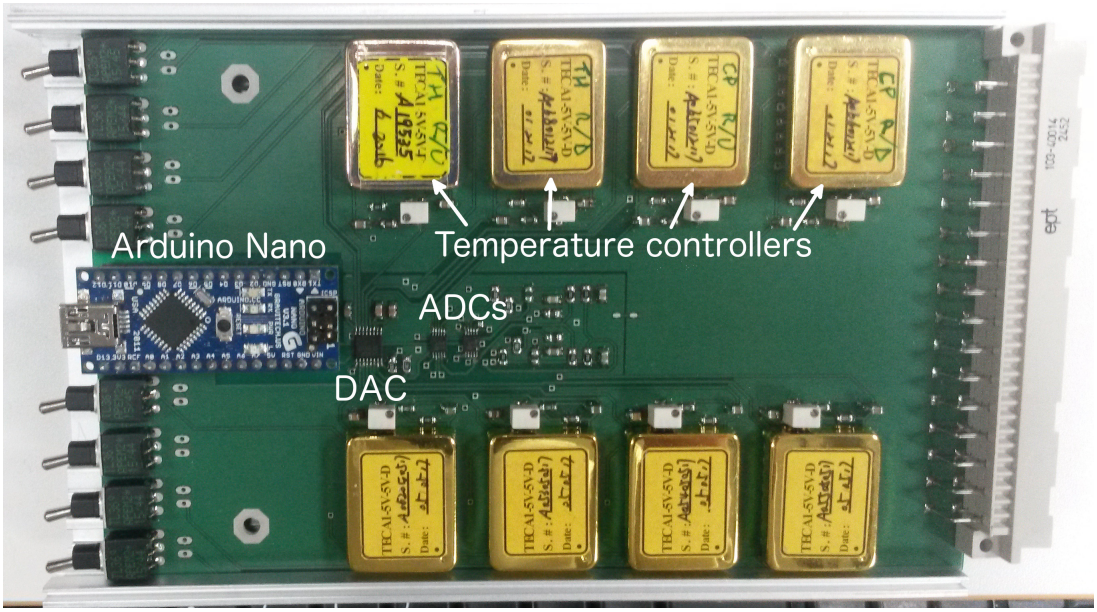

Figure C.2: Temperature control system electronics.

Acknowledgements

I'd like to thank all the members of the Quantum optics and relativity group at the Heinrich-Heine-Universität Düsseldorf (Institute für Experimentalphysik), in particular:

- Prof. Stephan Schiller for giving me the chanche to join such an exciting project and for always motivating me during my work;
- Pramod for working together for more than two years on the clock development;
- Dmitri Iwaschko and Ulrich Rosowski for their support;
- Prof. Axel Görlitz, Dr. Alexander Nevsky, Dr. Michael Hansen, Dr. Marco Schioppo, Dr. Christian Wellers, Soroosh Alighanbari, Jian Chang Kwong and Eugen Wiens for suggestions and helpful discussion;
- Beate Rödding, for her constant help with administrative issues.

Thanks to Prof. Michael Schmitt, who agreed to be my mentor and reviewer of my dissertation.

For the great time spent in Birmingham, I thank:

- Prof. Kai Bongs, Dr. Ole Kock and Dr. Joshua Hughes, for discussions and advices.
- Dr. Yeshpal Sigh, for always supporting us, also after the clock was transported to PTB.
- Dr. Dariusz Swierad, Sruthi Viswam, Dr. Wei He and Qasim Ubaid for the time spent together in the lab;
- A special thanks to Dr. Lyndsie Smith: it was a pleasure to work with her the first year of my PhD.

During the long time I spent at PTB, I've found a supportive and motivating environment. In particular I'd like to acknowledge:

- Dr. Christian Lisdat for being always available for discussions and for his constructive comments;
- Dr. Uwe Sterr for his valuable advices;
- Dr. Sören Dörscher, Dr. Ali Al-Masoudi, Dr. Silvio Koller, Dr. Stefan Vogt, Jacopo Grotti, Roman Schwarz and Sofia Herbers for their help and for all the nice measurements that we performed together.
- Dr. Sebastian Häfner for the help with the clock laser and with the upgrade of the vacuum system;
- Dr. Thomas Legero, Dan Matei and Dr. Erik Benkler, who enabled us to operate with one of the best clock laser in the world;
- Dr. Evgenij Pachomow and Veit Dahlke, for hosting our experiment in their laboratory;
- Andre Uhde, Mandy Rindermann, Klemens Budin, Andreas Koczwara, Mattias Misera and Marion Wengel for providing mechanical and electronic components.

Finally, I would like to thank Roman Schwarz, Dr. Christian Wellers and Dr. Michael Hansen, for helping with the translation of the abstract to German.

I declare under oath that I have compiled my dissertation independently and without any undue assistance by third parties under consideration of the 'Principles for the Safeguarding of Good Scientific Practice at Heinrich Heine University Düsseldorf'

Stefano Origlia

Düsseldorf, 26/02/18